NATIONAL TECHNICAL UNIVERSITY OF ATHENS
SCHOOL OF ELECTRICAL AND COMPUTER ENGINEERING
DIVISION OF INFORMATION TRANSMISSION AND MATERIAL TECHNOLOGY

MIMO Optical Satellite Systems: Power Allocation with Classical Optimization Methods and with Deep Learning Techniques

PhD Thesis

Theodore T. Kapsis
Electrical and Computer Engineer, NTUA

Three-member Advisory Committee:
A. D. Panagopoulos, Professor NTUA (Supervisor)
P. Cottis, Professor NTUA
G. Fikioris, Professor NTUA

Athens, March 2024

ΕΘΝΙΚΟ ΜΕΤΣΟΒΙΟ ΠΟΛΥΤΕΧΝΕΙΟ
ΣΧΟΛΗ ΗΛΕΚΤΡΟΛΟΓΩΝ ΜΗΧΑΝΙΚΩΝ
ΚΑΙ ΜΗΧΑΝΙΚΩΝ ΥΠΟΛΟΓΙΣΤΩΝ
ΤΟΜΕΑΣ ΣΥΣΤΗΜΑΤΩΝ ΜΕΤΑΔΟΣΗΣ ΠΛΗΡΟΦΟΡΙΑΣ
ΚΑΙ ΤΕΧΝΟΛΟΓΙΑΣ ΥΛΙΚΩΝ

Οπτικά Δορυφορικά Συστήματα MIMO: Ανάθεση Ισχύος με Κλασικές Μεθόδους Βελτιστοποίησης και με Τεχνικές Βαθιάς Μάθησης

ΔΙΔΑΚΤΟΡΙΚΗ ΔΙΑΤΡΙΒΗ

Θεόδωρος Θ. Καψής
Διπλ. Ηλεκτρολόγος Μηχ/κος & Μηχ/κος Υπολογιστών, Ε.Μ.Π.

Τριμελής Αθ. Δ. Παναγόπουλος, Καθηγητής Ε.Μ.Π. (Επιβλέπων)
Συμβουλευτική Π. Κωττής, Καθηγητής Ε.Μ.Π.
Επιτροπή: Γ. Φικιώρης, Καθηγητής Ε.Μ.Π.

Αθήνα, Μάρτιος 2024

ΕΘΝΙΚΟ ΜΕΤΣΟΒΙΟ ΠΟΛΥΤΕΧΝΕΙΟ
ΣΧΟΛΗ ΗΛΕΚΤΡΟΛΟΓΩΝ ΜΗΧΑΝΙΚΩΝ
ΚΑΙ ΜΗΧΑΝΙΚΩΝ ΥΠΟΛΟΓΙΣΤΩΝ
ΤΟΜΕΑΣ ΣΥΣΤΗΜΑΤΩΝ ΜΕΤΑΔΟΣΗΣ ΠΛΗΡΟΦΟΡΙΑΣ
ΚΑΙ ΤΕΧΝΟΛΟΓΙΑΣ ΥΛΙΚΩΝ

Οπτικά Δορυφορικά Συστήματα MIMO: Ανάθεση Ισχύος με Κλασικές Μεθόδους Βελτιστοποίησης και με Τεχνικές Βαθιάς Μάθησης

ΔΙΔΑΚΤΟΡΙΚΗ ΔΙΑΤΡΙΒΗ

Θεόδωρος Θ. Καψής
Διπλ. Ηλεκτρολόγος Μηχ/κος & Μηχ/κος Υπολογιστών, Ε.Μ.Π.

Συμβουλευτική Επιτροπή : Αθανάσιος Δ. Παναγόπουλος (Επιβλέπων)
Παναγιώτης Κωττής
Γεώργιος Φικιώρης

Εγκρίθηκε από την επταμελή εξεταστική επιτροπή την 20η Μαρτίου 2024.

.....	.....	.....
Αθανάσιος Παναγόπουλος Καθηγητής Ε.Μ.Π.	Παναγιώτης Κωττής Καθηγητής Ε.Μ.Π.	Γεώργιος Φικιώρης Καθηγητής Ε.Μ.Π.
.....	.....	.....
Γεώργιος Ματσόπουλος Καθηγητής Ε.Μ.Π.	Ιωάννα Ρουσσάκη Αν. Καθηγητής Ε.Μ.Π.	Βασίλειος Γκίκας Καθηγητής Ε.Μ.Π.

.....
Έκτορας Νισταζάκης
Καθηγητής ΕΚΠΑ

Αθήνα, Μάρτιος 2024

.....
Θεόδωρος Θ. Καψής

Διδάκτωρ Ηλεκτρολόγος Μηχανικός και Μηχανικός Υπολογιστών Ε.Μ.Π.

“Do not dwell in the past, do not dream of the future,
concentrate the mind on the present moment.”

—Siddhartha Gautama Buddha

Περίληψη

Τα ασύρματα δίκτυα πέμπτης γενιάς (fifth-generation, 5G) έχουν σχεδιαστεί για να ανταποκρίνονται στις ολοένα και πιο απαιτητικές ανάγκες των διαφορετικών αναδυόμενων υπηρεσιών με ξεχωριστές απαιτήσεις: Ευρυζωνικές υπηρεσίες υψηλής ταχύτητας, ετερογενείς, εξαιρετικά αξιόπιστες, ασφαλείς και χαμηλής καθυστέρησης. Στα ασύρματα δίκτυα πέρα από το 5G (beyond 5G, B5G), οι δορυφορικές επικοινωνίες και γενικά τα μη-επίγεια δίκτυα θεωρούνται τεχνολογίες ενεργοποίησης λόγω της δυνατότητας παροχής παγκόσμιας κάλυψης, της συνδεσιμότητας απομακρυσμένων περιοχών, της επεκτασιμότητας και της ανθεκτικότητάς τους. Οι δορυφορικές τεχνολογίες είναι ήδη αρκετά ώριμες για ζεύξεις υποστήριξης (backhauling) και για εφαρμογές Διαδικτύου των Πραγμάτων (Internet of Things, IoT) κάνοντας χρήση δορυφόρων υψηλής ρυθμαπόδοσης (high-throughput satellites, HTS) στη ζώνη Ka (20/30 GHz). Επίσης, αρκετές εθνικές και πολυεθνικές διαστημικές υπηρεσίες συμμετέχουν στην εξερεύνηση του βαθέως διαστήματος (deep-space), κοντά στη Γη (near-earth), της Σελήνης και του Άρη και σχεδιάζουν και άλλες αποστολές. Η βελτιστοποίηση των δορυφορικών επικοινωνιών είναι ένας ακόμη σημαντικός τομέας στη βιομηχανία του νέου διαστήματος (new space). Λόγω του περιορισμένου διαθέσιμου φάσματος, οι παραδοσιακές ζεύξεις ραδιοεπικοινωνιών (radio frequency, RF) αδυνατούν να παρέχουν τόσο υψηλή ρυθμαπόδοση. Η οπτική επικοινωνία ελευθέρου χώρου (free space optical, FSO) είναι μια εναλλακτική με ποικίλα πλεονεκτήματα έναντι της RF που έχει κερδίσει αυξημένη προσοχή στη δορυφορική κοινότητα. Ωστόσο, η FSO είναι ευάλωτη στις σοβαρές επιπτώσεις των ατμοσφαιρικών στροβιλισμών, των σφαλμάτων στόχευσης και των σπινθηρισμών.

Η παρούσα Διατριβή επικεντρώνεται στην μελέτη των οπτικών δορυφορικών συστημάτων επικοινωνιών και ειδικότερα στην μοντελοποίηση του οπτικού διαύλου κάτω ζεύξης (downlink, DL) και στη βελτιστοποίηση της κατανομής ισχύος σε οπτικά δορυφορικά δίκτυα πολλαπλών εισόδων - εξόδων (multi-input multi-output, MIMO). Δίνεται έμφαση στα δυσμενή φαινόμενα που αντιμετωπίζει η δέσμη φωτός κατά τη διάδοση στη γήινη ατμόσφαιρα και στις τεχνικές άμβλυνσης των φαινομένων αυτών. Αρχικά, για την ακριβή πρόβλεψη του σπινθηρισμού έντασης ακτινοβολίας του DL οπτικού καναλιού αναπτύχθηκε μεθοδολογία που παράγει χρονοσειρές με χρήση στοχαστικών διαφορικών εξισώσεων η οποία επικυρώθηκε και επιβεβαιώθηκε ως προς τα στατιστικά πρώτης και δεύτερης τάξης (συνάρτηση πυκνότητας πιθανότητας, αθροιστική συνάρτηση κατανομής, φασματική πυκνότητα ισχύος) με πειραματικά δεδομένα. Στη συνέχεια, εξετάζονται σενάρια αμιγώς

οπτικών δορυφορικών συστημάτων MIMO και προτείνονται αλγόριθμοι βέλτιστης και αποδοτικής εκχώρησης ισχύος. Το κύριο πρόβλημα διατυπώνεται ως κυρτό πρόβλημα βελτιστοποίησης με περιορισμούς μέγιστης επιτρεπτής εκπομπής ισχύος με σκοπό την μεγιστοποίηση της χωρητικότητας και κατόπιν αποσυντίθεται σε ανεξάρτητα κυρτά υποπροβλήματα. Η όλη προτεινόμενη μεθοδολογία είναι βασισμένη στον αλγόριθμο υδροπλήρωσης (water-filling) και ικανοποιεί τις συνθήκες Karush-Kuhn-Tucker (KKT). Επίσης, διερευνάται ο βέλτιστος έλεγχος ισχύος σε υβριδικά δορυφορικά δίκτυα (χρήση επιγείου relay). Θεωρείται η οπτική DL ζεύξη αποκωδικοποίησης-και-προώθησης διπλής αναπήδησης (dual-hop decode-and-forward) για μια γεωστατική δορυφορική πηγή. Λαμβάνονται υπόψη η χωρική συσχέτιση, οι μήτρες και συντελεστές συσχέτισης. Ακόμη, το πρόβλημα βελτιστοποίησης ισχύος διατυπώνεται και επιλύεται μη-γραμμικά για σχήματα υβριδικής αυτόματης αίτησης επανεκπομπής (hybrid automatic repeat request, HARQ) σε χαμηλής τροχιάς δορυφόρους (low-earth orbit, LEO). Ακολούθως, το πρόβλημα βελτιστοποίησης ισχύος ενσωματώνει τα σφάλματα στόχευσης και προτείνεται εύρωστη μεθοδολογία για την αντιμετώπιση της αβεβαιότητας της οπτικής διακύμανσης (jitter). Τέλος, η Διατριβή ολοκληρώνεται με την μελέτη αλγορίθμων νευρωνικών δικτύων, μηχανικής, βαθιάς και ενισχυτικής μάθησης. Προτείνεται αλγόριθμος χωρίς μοντέλο (model-free) που με ακρίβεια προβλέπει τη βέλτιστη κατανομή ισχύος σε κάθε οπτικό κανάλι.

Λέξεις Κλειδιά—αλγόριθμος υδροπλήρωσης, ασύρματα δίκτυα 5G, ασύρματες οπτικές επικοινωνίες, ατμοσφαιρικοί στροβιλισμοί, βαθιά ενισχυτική μάθηση, βέλτιστη εκχώρηση ισχύος, δορυφορικές επικοινωνίες, δορυφορικές ζεύξεις καθόδου, έλεγχος ισχύος, εργοδική χωρητικότητα, εύρωστη βελτιστοποίηση, λογαριθμοκανονικές διαλείψεις, κατανομή πόρων, κυρτή βελτιστοποίηση, μοντελοποίηση, νευρωνικά δίκτυα, οπτικά δορυφορικά δίκτυα, οπτικό υβριδικό δίκτυο, σπινθηρισμοί, στατιστικά μοντέλα, στοχαστικά μοντέλα, συσχέτιση καναλιού, GEO, LEO, HARQ, MIMO, ARTEMIS.

Abstract

Fifth-generation (5G) cellular networks are engineered to satisfy the unique requirements of a variety of emerging services, each with escalating demands: Broadband services characterized by low latency, security, high-speed, diversity, and high reliability. Because of their universal coverage, connectivity, scalability, and robustness, satellite communications and non-terrestrial networks are regarded as enabling technologies towards beyond 5G (B5G). High-throughput satellites (HTS) in the Ka-band (26–40 GHz) can be employed for Internet of Things (IoT) applications and backhauling because satellite technologies are now sufficiently mature for these usages. In addition, a number of countries and international space agencies take part in the exploration of Mars, the Moon, deep-space, and near-Earth. In the new space sector, optimizing satellite communications is another crucial field. Conventional radio frequency (RF) lines are unable to offer such high regulation because of the restricted spectrum available. In the satellite community, there has been a growing interest in free space optical (FSO) communication as an alternative to RF communication. Nonetheless, FSO is susceptible to the detrimental effects of scintillation, pointing errors, and clear air turbulence.

This Thesis focuses on the study of optical satellite communication systems and in particular on the modeling of the optical downlink (DL) channel and the optimization of power allocation in multiple-input multiple-output (MIMO) optical satellite networks. Emphasis is placed on the adverse effects faced by the laser beam from propagating in the Earth's atmosphere and on their mitigation techniques. First, for the accurate prediction of DL optical channel irradiance scintillations, a methodology was developed that generates time series using stochastic differential equations and validates them in terms of first and second-order statistics (probability density function, cumulative distribution function, power spectral density). Then, all-optical MIMO satellite system scenarios are considered, and optimal and efficient power allocation algorithms are proposed. The primary problem is formulated as a convex optimization problem with maximum allowed transmit power constraints to maximize capacity and then decomposed into independent convex sub-problems. The entire proposed methodology is based on the water-filling algorithm and satisfies the Karush-Kuhn-Tucker (KKT) conditions. Moreover, optimal power control in hybrid satellite relays is investigated. A dual-hop decode-and-forward optical DL link for a geostationary satellite source is considered. Spatial correlation, correlation matrices and, coefficients are included. Additionally, the power optimization problem is formulated and solved non-linearly for hybrid automatic repeat request (HARQ) schemes in low-earth orbit (LEO) satellites. Then,

the power optimization problem incorporates the pointing errors, and a robust maximin methodology is proposed to deal with optical jitter uncertainty. Finally, the Dissertation concludes with the study of neural networks, deep learning, and deep reinforcement learning algorithms. A model-free learning algorithm is proposed that accurately predicts the optimal power distribution in each optical channel.

Keywords—atmospheric turbulence, channel correlation, convex optimization, deep reinforcement learning, ergodic capacity, log-normal fading, modeling, neural networks, optical hybrid network, optical satellite networks, optimal power allocation, power control, resource allocation, robust optimization, satellite communications, satellite downlinks, scintillations, statistical models, stochastic models, water-filling algorithm, wireless 5G networks, wireless optical communications, ARTEMIS, GEO, HARQ, LEO, MIMO.

Acknowledgments/Ευχαριστίες

Αυτή η ενότητα της Διατριβής μου είναι αφιερωμένη στο να εκφράσω την ευγνωμοσύνη μου σε όλους τους ανθρώπους που συνέβαλαν στις προσπάθειές μου και στην ολοκλήρωση των διδακτορικών μου σπουδών. Είναι πολύ δύσκολο να συλλάβει κανείς τις σκέψεις και τα συναισθήματα κατά τον συλλογισμό των τελευταίων ετών. Ελπίζω μόνο ότι οι επόμενες λέξεις, παρά την απλότητά τους και την έλλειψη πρωτοτυπίας τους, μεταφέρουν την ειλικρίνεια και το βάθος της ευγνωμοσύνης μου.

Πρώτα και κύρια, θα ήθελα να ευχαριστήσω θερμά τον επιβλέποντα μου καθηγητή Αθανάσιο Δ. Παναγόπουλο που με εμπιστεύτηκε και μου πρόσφερε την ευκαιρία να συνεχίσω το διδακτορικό μου πτυχίο στο τόσο εμπνευσμένο και παραγωγικό περιβάλλον της Ομάδας Ασυρμάτων και Δορυφορικών Επικοινωνιών αλλά και να έχω την απαραίτητη οικονομική υποστήριξη για την ολοκλήρωση της. Η συνεχής τεχνική και ηθική του υποστήριξη και το γνήσιο ενδιαφέρον του με ενθάρρυνε και με καθοδήγησε σε όλα τα στάδια των σπουδών μου. Τα μαθήματα που πήρα κατά τη διάρκεια αυτής της καθοδήγησης θα μείνουν κοντά μου και θα συνεχίσουν να με βοηθούν να αντιμετωπίσω τις νέες προκλήσεις στη ζωή μου. Στη συνέχεια θα ήθελα να ευχαριστήσω ιδιαιτέρως τη συμβολή του Νικόλαου Λύρα, με τον οποίο συνεργάστηκα στενά κατά την εκπόνηση της παρούσας Διατριβής. Οι οξυδερκείς παρατηρήσεις του σχετικά με την έρευνά μου και τις ενδιαφέρουσες συζητήσεις μας ήταν εμπνευσμένες και καθοριστικές για την ολοκλήρωση της. Ελπίζω η αγάπη του για την έρευνα και η εργασιακή ηθική να αντικατοπτρίζονται στη δουλειά μου από εδώ και στο εξής.

Οι διδακτορικές μου σπουδές δεν θα ήταν ίδιες χωρίς τους Ph.D. υποψηφίους, ερευνητές και διοικητικό προσωπικό που αποτελείται της Ομάδας. Θα ήθελα να τους ευχαριστήσω όλους που ήταν μέρος ενός από τα πιο δύσκολα επιτεύγματα της ζωής μου και μερικές από τις πιο όμορφες αναμνήσεις μου. Τους θεωρώ φίλους μου τόσο σε επαγγελματικό όσο και σε προσωπικό επίπεδο. Με αυτά τα λόγια, θα ήθελα να ευχαριστήσω ιδιαιτέρως τους: Δρ. Ν. Λύρα, Δρ. Χ. Κουρόγιωργα, Δρ. Χρ. Εφραίμ, Δρ. Αν. Ρουμελιώτη, Δρ. Ν. Μωραΐτη, την Δρ. I. Popescu, Ν. Μπούζη με τους οποίους είχα μια εξαιρετική συνεργασία. Καθώς και όλους τους στενούς μου φίλους για ενδιαφέρουσες συζητήσεις, τη βοήθεια και την υποστήριξή τους και τις πολύτιμες στιγμές που μοιράστηκαν μαζί μου σε αυτό το ταξίδι.

Θα ήθελα επίσης να ευχαριστήσω το Ίδρυμα Α. Γ. Λεβέντη και τον Ειδικό Λογαριασμό Χρηματοδότησης Έρευνας (ΕΛΚΕ) του ΕΜΠ για την οικονομική υποστήριξή τους κατά τη διάρκεια της έρευνάς μου (2019–2021 και 2019–2023, αντίστοιχα).

Ακόμη, θα ήθελα να ευχαριστήσω όλους τους καθηγητές και συνεργάτες με τους οποίους συνεργάστηκα και ειδικότερα τους καθηγητές κ. Π. Κωττή, κ. Γ. Φικιώρη και κ. Χ. Καψάλη, η διδασκαλία των οποίων συνέβαλε καθοριστικά στην απόφασή μου να ασχοληθώ με το εν λόγω αντικείμενο και τομέα ευρύτερα. Ευχαριστώ πολύ και τα μέλη της επταμελούς επιτροπής εξέτασης για το χρόνο που αφιέρωσαν στην παρούσα εργασία.

Τέλος, θα ήθελα να ευχαριστήσω την μητέρα μου Ευσταθία για την αμέριστη αγάπη και υποστήριξή της. Είναι εκείνη που ήταν πιο κοντά μου σε αυτό το εγχείρημα, προσφέροντάς μου την υποστήριξή της και ποτέ δεν έχασε την πίστη της σε μένα. Κλείνοντας, θέλω να αφιερώσω την παρούσα Διδακτορική Διατριβή στη μνήμη του πατέρα μου Θεόδωρου.

Θεόδωρος Θ. Καψής

Αθήνα, Μάρτιος 2024

Στον ανώτερο εαυτό μας.

Table of Contents

List of Figures

List of Tables

List of Equations

Glossary of Technical Terms – Γλωσσάρι Τεχνικών Όρων

Αγγλικά	Ελληνικά
Aperture averaging factor	Συντελεστής άμβλυνσης στροβιλισμών
Artificial intelligence	Τεχνητή νοημοσύνη
Atmospheric attenuation	Ατμοσφαιρική εξασθένηση
Automatic repeat request	Αυτόματη αίτηση επανεκπομπής
Backhaul	Ζεύξη υποστήριξης
Beam spreading	Εξάπλωση δέσμης
Beam wander	Περιπλάνηση δέσμης
Bidirectional link	Αμφίδρομη ζεύξη
Bit error rate	Ρυθμός σφάλματος ψηφίων
Brute-force search	Αναζήτηση ωμής βίας
Channel state information	Περίθλαση
Cloud-free	Χωρίς σύννεφα
Coherence length	Μήκος συνοχής
Convex optimization	Κυρτή βελτιστοποίηση
Covariance matrix	Μήτρα συνδιακύμανσης
Cumulative distribution function	Αθροιστική συνάρτηση κατανομής
Data rate	Ρυθμός δεδομένων
Deep learning	Βαθιά μάθηση
Deep neural network	Ισχύς
Deep-space	Βαθύ διάστημα
Diffraction	Περίθλαση
Downlink	Κατερχόμενη ζεύξη
Elevation angle	Γωνία ανύψωσης
Feeder link	Ζεύξη τροφοδοσίας
Gateway	Πύλη δικτύου
GEO satellite	Γεωστατικός δορυφόρος
Gradient descent	Κατάβαση κλίσης
High-altitude platform	Πλατφόρμα μεγάλου ύψους
Intensity modulation – Direct Detection	Διαμόρφωση έντασης με άμεση ανίχνευση
Inter-satellite link	Δια-δορυφορική ζεύξη
Irradiance	Ένταση ακτινοβολίας
LEO satellite	Δορυφόρος χαμηλής τροχιάς
Line-of-sight	Οπτική επαφή
Link budget	Προϋπολογισμος ισχύος
Lognormal distribution	Λογαριθμοκανονική κατανομή
Machine learning	Μηχανική μάθηση
Mitigation techniques	Τεχνικές άμβλυνσης διαλείψεων
Modulation	Διαμόρφωση
Normal distribution	Κανονική κατανομή
Objective function	Αντικειμενική συνάρτηση
Optical ground station	Οπτικός σταθμός βάσης
Optimization	Βελτιστοποίηση

Outage capacity	Χωρητικότητα αποκοπής
Outage probability	Πιθανότητα αποκοπής
Pointing error	Σφάλμα στόχευσης
Pointing jitter	Διακύμανση στόχευσης
Power allocation	Ανάθεση ισχύος
Power constraints	Περιορισμοί ισχύος
Power spectral density	Φασματική πυκνότητα ισχύος
Probability density function	Συνάρτηση πυκνότητας πιθανότητας
Propagation	Διάδοση
Quantum key distribution	Κβαντικός διαμοιρασμός κλειδιού
Refractive index	Δείκτης διάθλασης
Reinforcement learning	Ενισχυτική μάθηση
Scintillation	Σπινθηρισμός
Scintillation index	Δείκτης σπινθηρισμού
Slant path	Κεκλιμένη διαδρομή
Spatial correlation	Χωρική συσχέτιση
Spatial diversity	Διαφορισμός θέσης
Spectral efficiency	Φασματική απόδοση
Stochastic differential equations	Στοχαστικές διαφορικές εξισώσεις
Time series	Χρονοσειρές
Tracking error	Σφάλμα παρακολούθησης
Transmitter diversity	Διαφορισμός πομπού
Turbulence	Στροβιλισμός
Uplink	Ανερχόμενη ζεύξη
Water-filling algorithm	Αλγόριθμος υδροπλήρωσης

Abbreviations

3GPP	3rd Generation Partnership Project
5G	5th Generation
ACK	Acknowledgment
AF	Amplify-and-Forward
ASE	Amplified Spontaneous Emission
AWGN	Additive White Gaussian Noise
B5G	Beyond 5th Generation
BER	Bit Error Rate
CC	Chase Combining
CCDF	Complementary Cumulative Distribution Function
CDF	Cumulative Distribution Function
CFLOS	Cloud Free Line of Sight
CINVA	Channel Inversion Algorithm
CSI	Channel State Information
CSIT	Channel State Information at Transmitter
DF	Decode-and-Forward
DL	Downlink / Deep Learning
DNN	Deep Neural Network
DQN	Deep Q-Learning Network
DRL	Deep Reinforcement Learning
EE	Energy Efficiency
EPA	Equal Power Allocation
ESA	European Space Agency
FSO	Free-Space Optical
FSPL	Free-Space Path Loss
GA	Gradient Ascent / Greedy Algorithm
GD	Gradient Descent
GEO	Geostationary Orbit
GND	Ground
GW	Gateway
HAP	High-Altitude Platform
HARQ	Hybrid Automatic Repeat Request
HTS	High Throughput Satellite
H-V	Hufnagel–Valley
i.i.d.	independent and identically distributed
IM/DD	Intensity Modulation/Direct Detection
IoT	Internet of Things
IP	Interior-Point
IR	Incremental Redundancy
JAXA	Japanese Aerospace Exploration Agency

KKT	Karush-Kuhn-Tucker
LEO	Low-Earth Orbit
LN	Lognormal
LTE	Long-Term Evolution
MEO	Medium Earth Orbit
MIMO	Multiple-Input Multiple-Output
ML	Machine Learning
MRC	Maximum-Ratio Combining
MSE	Mean Square Error
OGRS	Optical Ground Relay Station
OGS	Optical Ground Station
OGUS	Optical Ground User Station
OOK	On-Off-Keying
OPA	Optimal Power Allocation
OWC	Optical Wireless Communications
PA	Power Allocation
PDF	Probability Density Function
PL	Path Losses
PSD	Power Spectral Density
QKD	Quantum Key Distribution
QoS	Quality of Service
RF	Radio Frequency
RL	Reinforcement Learning
RoFSO	Radio over Free-Space Optical
SDE	Stochastic Differential Equation
SI	Scintillation Index
SQP	Sequential Quadratic Programming
s.t.	subject to
SVD	Singular Value Decomposition
TN	Truncated Normal
UE	User Equipment
UP	Uniform Power
WDM	Wavelength Division Multiplexing
WF	Water-Filling

Chapter 1
Extended Greek Summary – Εκτεταμένη Περίληψη

1.1 Εισαγωγή

Στο Κεφάλαιο 2 της παρούσας Διατριβής παρουσιάζεται μια εισαγωγή στα επίγεια δίκτυα πέμπτης γενιάς (fifth-generation, 5G), πέρα από το 5G (beyond 5G, B5G) και έκτης γενιάς (sixth-generation, 6G), δίνεται μια ανασκόπηση στις οπτικές δορυφορικές επικοινωνίες και στην τρέχουσα τεχνολογική κατάσταση καθώς και μια περιγραφή της διάρθρωσης της Διατριβής. Από το 2019, τα δίκτυα κινητής τηλεφωνίας 5G έχουν αναπτυχθεί σε όλο τον κόσμο και έχουν ήδη φτάσει σε πολύ μεγάλη κλίμακα σε ορισμένες χώρες. Για παράδειγμα, ο αριθμός των εγκατεστημένων σταθμών βάσης 5G στην Κίνα υπερέβη τις 500.000 στο τέλος του 2020, εξυπηρετώντας περισσότερους από 100 εκατομμύρια συνδρομητές 5G. Για τον ορισμό του 5G, τρία σενάρια χρήσης προτάθηκαν αρχικά από την ITU-R M.2083 το 2015: Βελτιωμένη κινητή ευρυζωνικότητα (enhanced mobile broadband, eMBB), εξαιρετικά αξιόπιστες επικοινωνίες χαμηλής καθυστέρησης (ultra-reliable low latency communications, URLLC), μαζικές επικοινωνίες τύπου μηχανής (massive machine-type communications, mMTC). Ωστόσο, αυτά τα σενάρια χρήσης 5G δεν μπορούν να ικανοποιήσουν τις τεχνικές απαιτήσεις των B5G και 6G. Για παράδειγμα, τα αυτόνομα οχήματα ή τα ιπτάμενα drones χρειάζονται πανταχού συνδεσιμότητα με υψηλή ρυθμαπόδοση, υψηλή αξιοπιστία και χαμηλή καθυστέρηση. Η ταχύτητα στο 6G αναμένεται να φτάσει έως και 1 Tbps, ενώ το 5G έχει μέγιστο ρυθμό 20 Gbps για την κατερχόμενη ζεύξη και 10 Gbps για την ανερχόμενη. Στο 5G, η ελάχιστη απαίτηση για καθυστέρηση επιπέδου χρήστη είναι 4 ms για eMBB και 1 ms για URLLC. Αυτή η τιμή προβλέπεται να μειωθεί περαιτέρω στα 100 μs ή και στα 10 μs. Στο 5G, οι μέγιστες φασματικές αποδόσεις είναι 30 bps/Hz στην κατερχόμενη ζεύξη και 15 bps/Hz στην ανερχόμενη. Εκτιμάται ότι οι προηγμένες ραδιοτεχνολογίες 6G μπορούν να επιτύχουν τρεις φορές υψηλότερη φασματική απόδοση σε σχέση με το 5G. Στα δίκτυα 5G, η ελάχιστη απαίτηση αξιοπιστίας μετριέται με πιθανότητα επιτυχίας $1-10^{-5}$. Αναμένεται να βελτιώσει τουλάχιστον δύο τάξεις μεγέθους, δηλαδή $1 - 10^{-7}$ ή 99.99999 %. Τέλος, η απαίτηση εύρους ζώνης στο 5G είναι τουλάχιστον 100 MHz ενώ το 6G θα υποστηρίζει έως και 1 GHz.

Τα παραδοσιακά επίγεια συστήματα επικοινωνίας έχουν ανθίσει με πολλούς τρόπους, ωστόσο, εξακολουθούν να υπάρχουν ορισμένα εγγενή μειονεκτήματα. Τα δίκτυα κινητής τηλεφωνίας έχουν κακή κάλυψη σε απομακρυσμένες περιοχές. Υποφέρουν από καθυστερήσεις μετάδοσης μεγάλων αποστάσεων. Επιπλέον, η ευπάθεια σε φυσικές καταστροφές τα καθιστά μη διαθέσιμα σε ακραίες περιπτώσεις. Επίσης, βάσει του Οδηγού Λύσεων Σύνδεσης στο Διαδίκτυο Τελευταίου Μιλίου που κυκλοφόρησε από τον Τομέα Ανάπτυξης της ITU, το 49% του παγκόσμιου πληθυσμού (ή 3.7 δισεκατομμύρια άνθρωποι) εξακολουθούσε να ζει χωρίς σύνδεση στο Διαδίκτυο στα τέλη του 2019.

Ο όρος μη επίγεια δίκτυα περιλαμβάνει μια τεράστια ποικιλία διαστημικών και εναέριων δικτύων επικοινωνίας, όπως δορυφόρους γεωστατικής τροχιάς (geostationary Earth orbit, GEO) (36000 χλμ), μεσαίας γήινης τροχιάς (medium Earth orbit, MEO) (5000 με 25000 χλμ), χαμηλής γήινης τροχιάς (low Earth orbit, LEO) (500 με 900 χλμ), δορυφορικούς αστερισμούς, πλατφόρμες μεγάλου ύψους (high-altitude platforms, HAPs), πλατφόρμες χαμηλού ύψους, μη επανδρωμένα εναέρια οχήματα (unmanned aerial vehicles, UAVs) και drones. Σε σύγκριση με τα παραδοσιακά επίγεια δίκτυα, τα δορυφορικά δίκτυα έχουν πολλά πλεονεκτήματα. Από οικονομική άποψη, το δορυφορικό δίκτυο είναι μια οικονομικά αποδοτική επιλογή όταν παρέχει κάλυψη επικοινωνιών για απομακρυσμένες περιοχές. Είναι επίσης ικανά να παρέχουν απρόσκοπτη και χαμηλής καθυστέρησης κινητή συνδεσιμότητα για οχήματα, τρένα, αεροπλάνα, UAVs κλπ. Επιπλέον, η δορυφορική επικοινωνία δεν είναι περιορισμένη από το έδαφος και δεν θα υποστεί ζημιά από φυσικές καταστροφές, καθιστώντας την κατάλληλη για επικοινωνίες έκτακτης ανάγκης καταστροφών. Με την ευρεία κάλυψή του, ο δορυφόρος μπορεί επίσης να παρέχει περιεχόμενο πολυμέσων. Τέλος, η σύνδεση δορυφόρου προς γη παρέχει μια εναλλακτική επιλογή ζεύξης κορμού (backhaul) για τα επίγεια δίκτυα, όταν η χωρητικότητα του επίγειου δικτύου είναι κορεσμένη. Πολλές εταιρείες, όπως η SpaceX, η Amazon, η OneWeb, η TeleSAT έχουν ήδη ανακοινώσει μεγάλα σχέδια LEO, συμπεριλαμβανομένων χιλιάδων δορυφόρων και ορισμένες έχουν ήδη εκτοξεύσει. Η SpaceX έχει στόχο να φτάσει σχεδόν τους 12.000 δορυφόρους μέχρι τα μέσα της δεκαετίας 2020s. Άλλα αξιοσημείωτα προγράμματα είναι το European data relay system (EDRS), το SeCure and Laser communication Technology (ScyLight), το High thRoughput Optical Network (HydRON), το Moonlight, το LunaNet και Mars Cube Ones (MarCOs). Τέλος, το Νέο Διάστημα (New Space) δεν αναφέρεται σε μια συγκεκριμένη τεχνολογία, αλλά υποδηλώνει μια νέα νοοτροπία απέναντι στο διάστημα. Προήλθε από τρεις κύριες πτυχές: 1) Ιδιωτικοποίηση του διαστήματος, 2) σμίκρυνση δορυφόρων, 3) καινοτόμες υπηρεσίες βασισμένες σε διαστημικά δεδομένα.

Οι ζώνες συχνοτήτων που χρησιμοποιούνται για δορυφορικές επικοινωνίες είναι η S (2–4 GHz), η X (8–12 GHz), η Ku (12/14 GHz) και η Ka (20/30 GHz). Η ζήτηση για υψηλότερους ρυθμούς δεδομένων και περιορισμένο διαθέσιμο εύρος ζώνης ωθεί τους χειριστές δορυφόρων να χρησιμοποιούν ήδη τις ζώνες Q/V (40/50 GHz) και να εξετάζουν την W (75–110 GHz). Αυτή η μετεγκατάσταση όχι μόνο απελευθερώνει την Ka για τη ζεύξη χρήστη, αλλά παρέχει υψηλότερο εύρος ζώνης για ζεύξεις τροφοδοσίας που μπορούν να φιλοξενήσουν έναν δορυφόρο υψηλής ρυθμαπόδοσης (high-throughput satellite, HTS).

Οι οπτικές επικοινωνίες ελεύθερου χώρου (free-space optical, FSO) αναμένεται να διαδραματίσουν σημαντικό ρόλο στα μελλοντικά δίκτυα 5G/B5G, τα οποία βασίζονται σε δορυφορικούς αστερισμούς LEO και μη επίγεια δίκτυα drone/HAPs. Αυτό προτρέπει την ανάπτυξη τερματικών laser που μπορούν να τοποθετηθούν σε μικρές κινούμενες πλατφόρμες. Πρόσφατα, τα συστήματα FSO αναδείχθηκαν ως βιώσιμη επιλογή για την κάλυψη των βασικών απαιτήσεων των δικτύων 6G. Πράγματι, οι ζώνες επικοινωνίας FSO είναι χωρίς παρεμβολές και αδειοδότηση, όπου οι μεταδόσεις στα 850, 1310 και 1550 nm ταιριάζουν καλά με την τυπική επικοινωνία οπτικών ινών. Αυτή η συμβατότητα με την υπάρχουσα υποδομή οπτικών ινών επιτρέπει στα συστήματα FSO να προσφέρουν χωρητικότητα συγκρίσιμη με την οπτική ίνα αλλά σε ένα κλάσμα του κόστους της ανάπτυξής τους. Η FSO αποτελεί μια ευέλικτη και ευεργετική λύση για δορυφορικά συστήματα καθώς παρουσιάζει σχετικά εύκολη και γρήγορη ανάπτυξη, τεράστια ποσά εύρους ζώνης που μπορεί να φτάσει εκατοντάδες terabit/s, δεν απαιτούνται άδειες χρήσης φάσματος, τεχνολογία από σημείο σε σημείο λόγω στην πολύ στενή μεταδιδόμενη δέσμη λέιζερ, καθιστώντας έτσι κατάλληλη για ζεύξεις κορμού (backhauling) και πύλης δικτύου.

Παρά τα πιθανά πλεονεκτήματά τους σε σχέση με τις ραδιοσυχνότητες (radio frequency, RF) οι συνδέσεις FSO έχουν πολλές εγγενείς προκλήσεις που θα πρέπει να αντιμετωπιστούν προσεκτικά για την επίτευξη σταθερών και αξιόπιστων συστημάτων επικοινωνίας. Αυτές οι προκλήσεις περιλαμβάνουν απώλειες απορρόφησης και σκέδασης λόγω βροχής, χιονιού και ομίχλης, καθώς και τυχαίες διακυμάνσεις στη γωνία άφιξης δέσμης που προκαλούνται από ατμοσφαιρικούς στροβιλισμούς, όπως σπινθηρισμοί και περιπλάνηση δέσμης. Υπάρχουν πρόσθετες προκλήσεις που σχετίζονται με το σχεδιασμό μιας ζεύξης FSO: Απώλειες κακής ευθυγράμμισης, ατμοσφαιρικές απώλειες, καιρικές συνθήκες (ομίχλη, σύννεφα, ομίχλη, αιθαλομίχλη, χιόνι, άνεμοι, βροχή, πολικά σύννεφα, ηφαιστειακή δραστηριότητα), θόρυβος, σκέδαση, απώλεια διαδρομής, ολίσθηση Doppler. Ως εκ τούτου, χρησιμοποιούνται τεχνικές μετριασμού, όπως υβριδικά συστήματα FSO/RF, διαφορισμός θέσης μέσω οπτικών επίγειων σταθμών και διαφορισμός μήκους κύματος. Μέθοδοι φυσικού επιπέδου όπως οπτικοί δέκτες

μεγάλης διαμέτρου για την άμβλυνση των ατμοσφαιρικών στροβιλισμών (aperture averaging), και τα προσαρμοστικά οπτικά (adaptive optics, AO) είναι από τις πιο εφαρμοσμένες τεχνικές για τον μετριασμό των σπινθηρισμών.

1.2 Μοντελοποίηση ατμοσφαιρικών στροβιλισμών - Σύνθεση χρονοσειρών ισχύος σε κατερχόμενες οπτικές δορυφορικές ζεύξεις και επικύρωση με πειραματικά αποτελέσματα

Στο Κεφάλαιο 3 της παρούσας Διατριβής αναφέρεται μια μεθοδολογία για τη δημιουργία χρονοσειρών λαμβανόμενης ακτινοβολίας/ισχύος για μια κατερχόμενη ζεύξη GEO που αφορά μικρά οπτικά τερματικά (τηλεσκόπια). Η γεννήτρια χρονοσειρών λαμβάνει υπόψη τα ατμοσφαιρικά φαινόμενα που υποβαθμίζουν τη διάδοση του οπτικού σήματος και ιδιαίτερα τα φαινόμενα στροβιλισμού. Για τη μοντελοποίηση των φαινομένων σπινθηρισμού θεωρούνται οι εξής βασικές παραδοχές: α) Μετάδοση κατερχόμενης ζεύξης, β) ζεύξεις με γωνία ανύψωσης μεγαλύτερη από 20 μοίρες, γ) λαμβάνονται υπόψη ασθενείς στροβιλισμοί, δ) εκπέμπεται μόνο μία δέσμη Gauss, ε) θεωρείται το φάσμα Kolmogorov και η προσέγγιση Rytov περί ασθενών στροβιλισμών. Για την ενσωμάτωση των φαινομένων στροβιλισμού, απαιτείται η σταθερά δομής του δείκτη διάθλασης για ολόκληρη την κεκλιμένη διαδρομή και η τροποποιημένη έκδοση του μοντέλου Hufnagel-Valley (H-V). Για ασθενείς στροβιλισμούς, το κανονικοποιημένο λογαριθμικό πλάτος μπορεί να θεωρηθεί ως χαμηλοπερατή Γκαουσιανή διαδικασία μηδενικής μέσης τιμής, μοναδιαίας διασποράς με κλίση -80/3 dB/δεκάδα. Τέτοιες διαδικασίες μπορούν να μοντελοποιηθούν χρησιμοποιώντας στοχαστικές διαφορικές εξισώσεις (stochastic differential equations, SDEs) που οδηγούνται από κλασματική κίνηση Brown. Η προτεινόμενη γεννήτρια χρονοσειρών επικυρώνεται ως προς τα στατιστικά πρώτης και δεύτερης τάξης με πειραματικά δεδομένα από την οπτική διαστημική αποστολή ARTEMIS με πολύ καλή συμφωνία. Πιο συγκεκριμένα, η αθροιστική συνάρτηση κατανομής (cumulative distribution function, CDF) που υπολογίζεται απευθείας από τα δεδομένα ARTEMIS συγκρίνεται με την CDF από τον προτεινόμενη γεννήτρια χρονοσειρών. Επιπλέον, οι συναρτήσεις πυκνότητας πιθανότητας (probability distribution function, PDF) που προέρχονται από τα πειραματικά δεδομένα συγκρίνονται με αυτές που προέρχονται από τα συντιθέμενα δεδομένα και παρουσιάζεται ο αντίστοιχος δείκτης σπινθηρισμού. Ομοίως, η φασματική πυκνότητα ισχύος (power spectral density, PSD) των μετρήσεων ARTEMIS συγκρίνεται με την PSD των παραχθέντων χρονοσειρών.

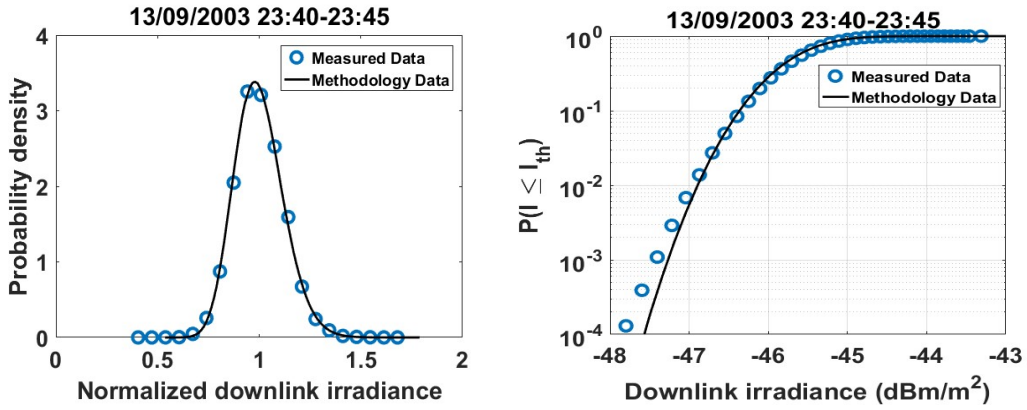

(α) (β)

Σχήμα 1: Επικύρωση στατιστικών πρώτης τάξης (α) Συνάρτηση κανονικοποιημένης πυκνότητας πιθανότητας (PDF) δεδομένων μέτρησης έναντι κανονικοποιημένης PDF των παραγόμενων δεδομένων. (β) αθροιστική συνάρτηση κατανομής (CDF) δεδομένων μέτρησης έναντι CDF παραγόμενων δεδομένων.

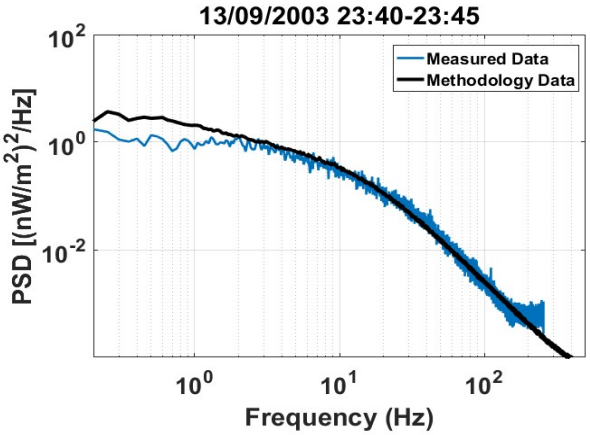

Σχήμα 2: Επικύρωση στατιστικών δεύτερης τάξης. PSD δεδομένων μέτρησης έναντι PSD παραγόμενων δεδομένων.

Στο Σχήμα 1, παρουσιάζονται τα στατιστικά πρώτης τάξης, η κανονικοποιημένη PDF και η CDF για αυτήν τη συνεδρία και συγκρίνονται με τα πειραματικά αποτελέσματα. Στο Σχήμα 2 φαίνονται τα στατιστικά δεύτερης τάξης (PSD) και ελέγχονται έναντι των πειραματικών αποτελεσμάτων. Τέλος, επισημαίνεται η χρήση του για προσομοίωση και μοντελοποίηση σε επίπεδο συστήματος. Παρουσιάζονται προσομοιωμένα στατιστικά λαμβανόμενης ισχύος για διάφορες καιρικές συνθήκες χρησιμοποιώντας την προτεινόμενη επικυρωμένη μεθοδολογία.

1.3 Βέλτιστη κατανομή ισχύος σε κατερχόμενες οπτικές δορυφορικές ζεύξεις και σε υβριδικά οπτικά δορυφορικά δίκτυα

Στο Κεφάλαιο 4 της παρούσας Διατριβής εξετάζεται μια οπτική κατερχόμενη ζεύξη GEO δορυφόρου σε μια διαμόρφωση πολλαπλών πομπών και πολλαπλών δεκτών (multiple-input multiple-output, MIMO) και προτείνεται ένας βέλτιστος αλγόριθμος κατανομής ισχύος που λαμβάνει υπόψη τα φαινόμενα των τυρβωδών ατμοσφαιρικών καναλιών. Η αντικειμενική συνάρτηση που βελτιστοποιείται είναι η εργοδική χωρητικότητα του δικτύου υπό τον ολικό αναμενόμενο περιορισμό ισχύος και την μέγιστη επιτρεπόμενη ισχύ εκπομπής. Τα κανάλια επικοινωνίας χρησιμοποιούν ίδιο μήκος κύματος και ένα σχήμα διαμόρφωσης έντασης και άμεσης ανίχνευσης (intensity modulation and direct detection, IM/DD). Επιπλέον, θεωρούνται τέλειες συνθήκες στόχευσης και παρακολούθησης και η ατμόσφαιρα ελεύθερη από σύννεφα και ομίχλη. Τα οπτικά στοιχεία πρέπει να είναι επαρκώς τοποθετημένα σε αποστάσεις μεγαλύτερες από την παράμετρο Fried, ώστε τα οπτικά κανάλια να είναι ασυσχέτιστα και ανεξάρτητα. Η παράμετρος Fried ορίζεται ως το μήκος συνοχής της ατμόσφαιρας. Έχουν χρησιμοποιηθεί πραγματικά πειραματικά δεδομένα για την εφαρμογή των προτεινόμενων στρατηγικών κατανομής. Ο αλγόριθμος παρουσιάζεται τόσο σε συνθήκες ασθενούς όσο και σε ισχυρούς στροβιλισμούς. Παρουσιάζονται προσομοιώσεις δικτύου με αριθμητικά δεδομένα που διερευνούν την ευαισθησία του αλγορίθμου στον σπινθηρισμό και στην ατμοσφαιρική εξασθένηση. Τα βήματα της μεθοδολογίας βασίζονται στον αλγόριθμο υδροπλήρωσης και στον σχηματισμό της συνάρτησης Lagrangian και στη μετατροπή του αρχικού περιορισμένου προβλήματος σε ένα μη περιορισμένο. Το πρόβλημα βελτιστοποίησης αναλύεται σε απλούστερα, ανεξάρτητα κυρτά υποπροβλήματα που επιλύονται χρησιμοποιώντας κατάλληλη μεθοδολογία που καθοδηγείται από τον γνωστό αλγόριθμο υδροπλήρωσης. Στη συνέχεια εφαρμόζονται οι γνωστές συνθήκες Karush–Kuhn–Tucker (ΚΚΤ) αφού είναι απαραίτητες και επαρκείς. Τέλος, ο προτεινόμενος αλγόριθμος συγκρίνεται με άλλους κλασικούς αλγόριθμους ως προς τον ρυθμό δεδομένων, τη ταχύτητα σύγκλισης και την επεκτασιμότητα σε σενάρια με παραπλήσια αλλά και με πολύ ανόμοια επίπεδα εξασθένησης και σπινθηρισμού. με εξαιρετικά αποτελέσματα.

Επιπροσθέτως, προτείνεται μια μεθοδολογία κατανομής ισχύος για ένα πλήρως οπτικό υβριδικό δορυφορικό δίκτυο που αποτελείται από μια πολυκαναλική πηγή δορυφόρου, έναν οπτικό σταθμό αναμετάδοσης (πύλη) και έναν οπτικό εξοπλισμό χρήστη. Χρησιμοποιείται ένα σχήμα διπλής αναπήδησης, αποκωδικοποίησης-και-προώθησης για τα οπτικά κανάλια

κατερχόμενης ζεύξης που επηρεάζονται από την εξασθένηση, τον σπινθηρισμό και τη χωρική συσχέτιση. Η βελτιστοποίηση κατανομής ισχύος εκτελείται σε σχέση με τους περιορισμούς ισχύος τόσο της πηγής όσο και του αναμεταδότη. Το πρόβλημα κατανομής ισχύος αρχικά δομείται ως ένα κυρτό πρόβλημα βελτιστοποίησης και στη συνέχεια επιλύεται με την αντίστοιχη θεωρία κυρτότητας και τη μέθοδο Αποσύνθεσης Ιδιαζουσών Τιμών (singular value decomposition, SVD) λαμβάνοντας υπόψη τη χωρική συσχέτιση καναλιών, την ατμοσφαιρική εξασθένηση και τους σπινθηρισμούς. Τέλος, εκτελούνται αριθμητικές προσομοιώσεις για να εξεταστεί ο αντίκτυπος της συσχέτισης στη χωρητικότητα του συστήματος και να αξιολογηθεί η απόδοση του προτεινόμενου αλγορίθμου. Παρουσιάζονται τα προκύπτοντα αριθμητικά αποτελέσματα και γίνονται παρατηρήσεις για την επικύρωση της προτεινόμενης μεθοδολογίας σε διάφορες τοπολογίες και ρυθμίσεις δικτύου. Τα σφάλματα στόχευσης/παρακολούθησης θεωρούνται αυθαίρετα μικρά ενώ ένα κανάλι ανάδρασης παρέχει γνώση καναλιού (channel state information at transmitter, CSIT) τόσο στην πηγή όσο και στον αναμεταδότη. Τέλος, θεωρούνται συνθήκες χωρίς σύννεφα.

Στο Σχήμα 3 παρουσιάζεται η μέση κατανομή ισχύος στα οπτικά δορυφορικά κανάλια και η εργοδική χωρητικότητα συναρτήσει της ολικής αναμενόμενης ισχύος για διάφορους δείκτες σπινθηρισμού. Στο Σχήμα 4, η χωρητικότητα του συστήματος παρουσιάζεται ως συνάρτηση της ολικής ισχύος των GEO και OGRS για διαφορετικούς συντελεστές συσχέτισης καναλιών.

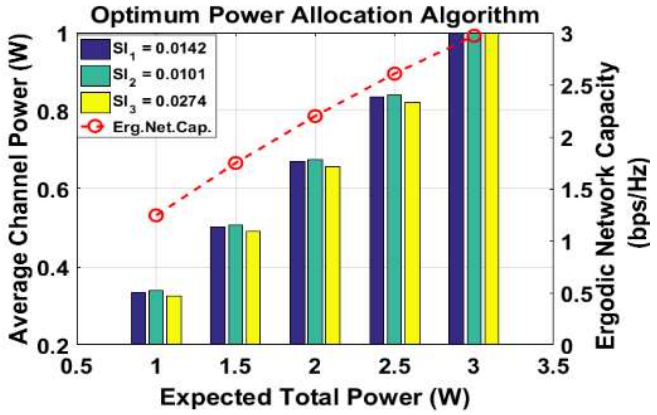

Σχήμα 3: Προτεινόμενος αλγόριθμος κατανομής ισχύος και εργοδική χωρητικότητα έναντι της αναμενόμενης ολικής ισχύος. Πραγματικά πειραματικά δεδομένα.

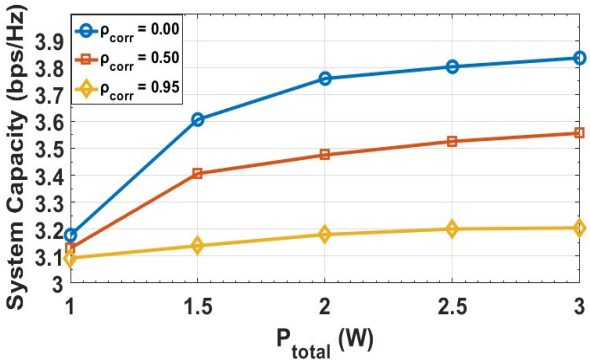

Σχήμα 4: Η χωρητικότητα του συστήματος έναντι της συνολικής ισχύος για διάφορους συντελεστές συσχέτισης. Όσο μεγαλύτερη η συσχέτιση τόσο χαμηλότερη η φασματική απόδοση.

1.4 Βέλτιστη κατανομή ισχύος σε κατερχόμενες οπτικές δορυφορικές ζεύξεις με HARQ

Στο Κεφάλαιο 5 της παρούσας Διατριβής προτείνεται μια μεθοδολογία κατανομής ισχύος για οπτικές κατερχόμενες ζεύξεις LEO-προς-Γη υπό συνθήκες ασθενούς σπινθηρισμού χρησιμοποιώντας σχήματα υβριδικής αυτόματης αίτησης επανεκπομπής (Hybrid Automatic Repeat Request, HARQ). Προτείνονται τρεις μεθοδολογίες κατανομής ισχύος που βασίζονται στα σχήματα Type I, Chase Combining (CC) και Incremental Redundancy (IR) και οι επιδόσεις τους συγκρίνονται και κατατάσσονται από την καλύτερη προς τη χειρότερη ως προς τη μέση κατανάλωση ενέργειας. Η ενεργειακή απόδοση και η αξιοπιστία των οπτικών ζεύξεων βελτιστοποιούνται διατυπώνοντας το πρόβλημα βελτιστοποίησης ως περιορισμένο πρόβλημα μη γραμμικού προγραμματισμού με αντικειμενική συνάρτηση την μέση κατανάλωση ενέργειας, τους περιορισμούς ισχύος και μια πιθανότητα αποκοπής αντίστοιχα. Απαιτούνται μόνο τα μακροπρόθεσμα στατιστικά του καναλιού για να επιτευχθεί η βέλτιστη στρατηγική κατανομής ισχύος και όχι οι στιγμιαίες καταστάσεις καναλιού. Οι προτεινόμενες λύσεις προέρχονται αριθμητικά μέσω επαναληπτικών αλγορίθμων εσωτερικού σημείου (interior point, IP) και διαδοχικού τετραγωνικού προγραμματισμού (sequential quadratic programming, SQP) και επικυρώνονται μέσω εξαντλητικής αναζήτησης. Οι προσομοιώσεις εκτελούνται για διάφορες συνθήκες καναλιού και ρυθμίσεις συστήματος προσομοιώνοντας ένα LEO που διέρχεται από διάφορες εντάσεις στροβιλισμών και επίγειες καιρικές συνθήκες για να διερευνηθεί η ευαισθησία των τριών σχημάτων HARQ σε ασθενή σπινθηρισμό, απώλεια διαδρομής και πιθανότητα αποκοπής. Για την μετάδοση, θεωρείται η διαμόρφωση OOK και χρησιμοποιείται DD για τη λήψη. Για να επιτευχθούν ανεξάρτητες καταστάσεις

εξασθένισης, ο ελάχιστος χρόνος αναμετάδοσης μεταξύ των γύρων πρέπει να είναι ίσος με τον χρόνο συνοχής του οπτικού καναλιού. Το HARQ Type I αποδίδει την υψηλότερη μέση συνολική ισχύ, το CC είναι μέτριο και το IR αποδίδει τη χαμηλότερη μέση συνολική ισχύ. Ο αλγόριθμος IP βρέθηκε να είναι πιο ακριβής στην εύρεση της καθολικής λύσης, αλλά ο SQP είναι ταχύτερος. Στο Σχήμα 5, η επίδραση του SI στη μέση συνολική ισχύ αξιολογείται για τα τρία πρωτόκολλα HARQ. Η προτεινόμενη μεθοδολογία προσομοιώνεται χρησιμοποιώντας τους αλγόριθμους IP και SQP και επικυρώνεται με αναζήτηση ωμής βίας.

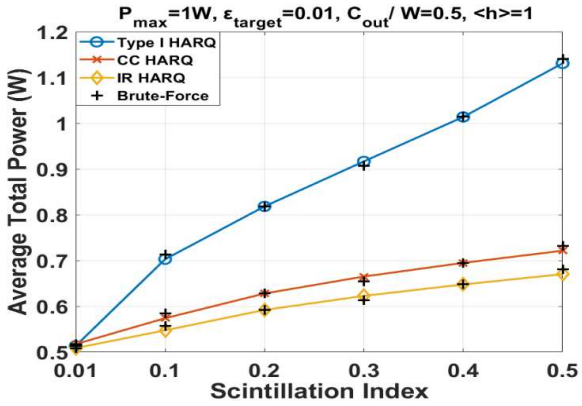

Σχήμα 5: Βελτιστοποίηση της μέσης συνολικής ισχύος έναντι του δείκτη σπινθηρισμού για τα σχήματα Type I, CC και IR HARQ.

1.5 Εύρωστη κατανομή ισχύος σε οπτικές δορυφορικές ζεύξεις MIMO με διακύμανση στόχευσης

Στο Κεφάλαιο 6 της παρούσας Διατριβής το πρόβλημα βελτιστοποίησης κατανομής ισχύος μελετάται για ένα οπτικό GEO-προς-Γη σύστημα που επικοινωνεί μέσω οπτικών καναλιών MIMO υπό την επίδραση της ατμοσφαιρικής εξασθένησης, στροβιλισμών και διακύμανσης στόχευσης (pointing jitter). Η γνώση τόσο των στατιστικών στοιχείων των οπτικών καναλιών όσο και των στιγμιαίων κερδών, δηλαδή των μακροπρόθεσμων και βραχυπρόθεσμων πληροφοριών CSIT, είναι απαραίτητη για τη μεγιστοποίηση της εργοδικής χωρητικότητας του δικτύου. Ωστόσο, η διακύμανση στόχευσης είναι μια στοχαστική διαδικασία που δεν μπορεί να προβλεφθεί με ακρίβεια, επομένως μια εύρωστη μεθοδολογία προτείνεται για την αντιμετώπιση της αβεβαιότητας: α) Η χειρότερη χωρητικότητα παράγει ένα πρόβλημα μέγιστης βελτιστοποίησης με περιορισμούς μεγίστης και συνολικής ισχύος. Η χειρότερη χωρητικότητα εμφανίζεται όταν η διακύμανση στόχευσης φτάσει στο χαμηλότερο

σημείο της. β) Το κάτω όριο της εργοδικής χωρητικότητας. Ένα εύρωστο κυρτό πρόβλημα βελτιστοποίησης διατυπώνεται και επιλύεται για παράλληλες κατερχόμενες οπτικές ζεύξεις υπό τις επιδράσεις των ατμοσφαιρικών στροβιλισμών και της διακύμανσης στόχευσης. Η ενσωμάτωση του ατμοσφαιρικού σπινθηρισμού και της διακύμανση στόχευσης σε όλη την ανάλυση αποδίδει ένα σημαντικά διαφορετικό πρόβλημα από το RF. Οι προσομοιώσεις πραγματοποιούνται χρησιμοποιώντας πραγματικά πειραματικά δεδομένα από το πρόγραμμα ARTEMIS. Τα προτεινόμενα σχήματα κατανομής ισχύος συγκλίνουν στη βέλτιστη λύση γρήγορα. Χρησιμοποιείται το σχήμα IM/DD, τα οπτικά κανάλια θεωρούνται ασυσχέτιστα και χωρίς σύννεφα αλλά υποφέρουν από απώλειες διαδρομής, σπινθηρισμό και διακύμανση στόχευσης. Οι λύσεις των τετραγωνικών εξισώσεων προκύπτουν από τις συνθήκες στασιμότητας KKT. Η χωρητικότητα του δικτύου υποβαθμίζεται σοβαρά όταν η διακύμανση στόχευσης υπερβαίνει την αναμενόμενη τιμή του και τα αποτελέσματα επιβεβαιώνουν την υπεροχή της φασματικής απόδοσης των προτεινόμενων σχημάτων.

Στο Σχήμα 6, η χειρότερη χωρητικότητα υπολογίζεται για διάφορες τιμές του Ω, η απόκλιση από τις μέσες απώλειες jitter. Παρατηρούμε ότι το jitter προκαλεί αξιοσημείωτες απώλειες που δεν μπορούν να αγνοηθούν καθώς το Ω αυξάνεται..

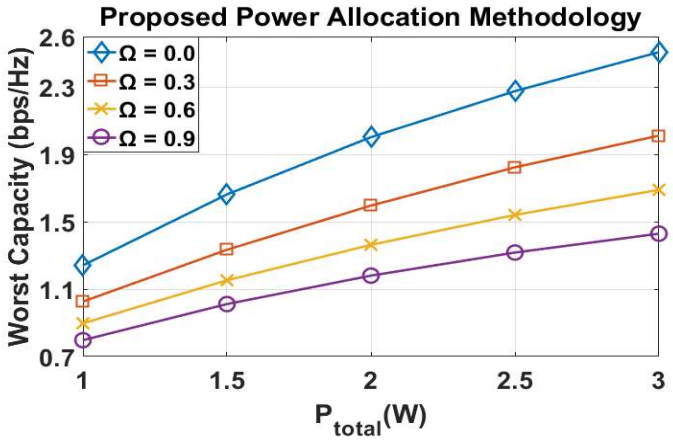

Σχήμα 6: Η χειρότερη χωρητικότητα σε σχέση με τη συνολική ισχύ εκπομπής. Όσο μεγαλύτερη είναι η απόκλιση από τις μέσες απώλειες jitter, τόσο χαμηλότερη είναι η φασματική απόδοση.

1.6 Βέλτιστη κατανομή ισχύος σε οπτικές δορυφορικές ζεύξεις με αλγορίθμους βαθιάς μάθησης

Στο Κεφάλαιο 7, διερευνώνται διάφορες μεθοδολογίες και ευρετικές μέθοδοι χωρίς μοντέλα καναλιών για τη βέλτιστη κατανομή ισχύος και, στη συνέχεια, συγκρίνονται με την ακριβή, βασισμένη σε μοντέλο λύση για μια πλήρως οπτική κατερχόμενη δορυφορική ζεύξη

πολλαπλών καναλιών, μεταξύ ενός γεωστατικού δορυφόρου και ενός οπτικού επίγειου σταθμού. Η βαθιά μάθηση αποτελεί ένα ισχυρό εργαλείο για το χειρισμό δεδομένων από πολύπλοκα και διαλείποντα κανάλια επικοινωνίας. Επομένως, το πρόβλημα βελτιστοποίησης διατυπώνεται ως ένα πρόβλημα μάθησης με περιορισμούς μεγίστης και συνολικής αναμενόμενης διαθέσιμης ισχύος. Συγκεκριμένα, προτείνεται μια μονάδα βαθιάς ενισχυτικής μάθησης (DRL) που βοηθά τους πράκτορες να παράγουν ενέργειες μέσω μιας τεχνικής στοχαστικής κλίσης πολιτικής, δεδομένων των παρατηρήσεων πληροφοριών κατάστασης καναλιού (CSI) από το περιβάλλον. Η πολιτική είναι δομημένη ως ένα βαθύ νευρωνικό δίκτυο και εκπαιδεύεται σύμφωνα με τον αλγόριθμο REINFORCE, αλλά τροποποιημένη ώστε να περιλαμβάνει τους περιορισμούς ισχύος και το οπτικό περιβάλλον πολλαπλών πρακτόρων. Οι πράκτορες έχουν πρόσβαση μόνο στις τοπικές τους παρατηρήσεις, αλλά προσπαθούν συλλογικά να μεγιστοποιήσουν την ολική ανταμοιβή. Η προτεινόμενη στρατηγική κρίνεται κατάλληλη για δύσκολες οπτικές συνθήκες, δεδομένου ότι μαθαίνει ρητά από την παρατήρηση. Ενώ το πρόβλημα βελτιστοποίησης έχει προσεγγιστεί στη βιβλιογραφία, δεν έχει παρουσιαστεί ποτέ σε σενάριο οπτικού δορυφόρου MIMO μαζί με διαθέσιμα πειραματικά δεδομένα.

Συνοψίζοντας τις κύριες συνεισφορές αυτού του Κεφαλαίου: 1) Προτείνεται ένας αλγόριθμος με τη βοήθεια DRL για τη βέλτιστη κατανομή ισχύος σε ένα οπτικό σύστημα πολλαπλών καναλιών GEO-to-ground. Η προτεινόμενη μέθοδος προσαρμόζει με ακρίβεια την αναμενόμενη ισχύ για κάθε οπτικό κανάλι, χωρίς καμία γνώση των απωλειών διαδρομής και των συνθηκών σπινθηρισμού. Χρησιμοποιούνται μόνο δείγματα CSI. Η συνολική αναμενόμενη ισχύς και η μέγιστη ισχύς είναι περιορισμένες. Αν και σε ένα σενάριο LEO/MEO η βαθιά μάθηση θα ήταν ακόμη πιο ωφέλιμη, το οπτικό GEO CSI εξακολουθεί να είναι ασταθές λόγω των διακυμάνσεων της σταθερά δομής του δείκτη διάθλασης κατά μήκος της κεκλιμένης διαδρομής, των λεπτών νεφών που μπορεί να εξασθενήσουν ή να μπλοκάρουν την δέσμη λέιζερ και των σφαλμάτων στόχευσης και παρακολούθησης. 2) Αντί για προσομοιωμένα δεδομένα, χρησιμοποιήθηκαν πειραματικές χρονοσειρές ακτινοβολίας από τις συνεδρίες του οπτικού δορυφόρου ARTEMIS του Ευρωπαϊκού Οργανισμού Διαστήματος (ESA) για την αξιολόγηση της απόδοσης της προτεινόμενης μεθοδολογίας. 3) Η επιτυγχανόμενη εργοδική χωρητικότητα συστήματος από την εφαρμογή του προτεινόμενου αλγορίθμου υπερβαίνει κατά πολύ την απόδοση των σχημάτων Equal Power, Random Power και Deep Q-Learning Network (DQN) χωρίς μοντέλα και προσεγγίζει τη βασισμένη σε μοντέλο, απαράμετρη λύση με πολύ καλή συμφωνία. 3) Διεξήχθη διερεύνηση του αντίκτυπου του αριθμού των κρυφών επιπέδων και νευρώνων, των κατανομών πολιτικής

και των επιδράσεων επιλογής υπερπαραμέτρων και υπερπροσαρμογής. 4) Η προτεινόμενη λύση διαφέρει από άλλες τυπικές φόρμουλες μάθησης επειδή εφαρμόζεται σε ένα πρόβλημα πολλαπλών πρακτόρων που βασίζεται στην προσέγγιση κοινής χρήσης παραμέτρων, επιτρέποντας την κεντρική μάθηση σε μια ενιαία πολιτική για ταχύτερη σύγκλιση. Το μοντέλο μάθησης είναι επεκτάσιμο καθώς έχει δοκιμαστεί σε σενάρια με μεγάλο αριθμό οπτικών δορυφορικών κατερχομένων ζεύξεων και μεγάλο όγκο δεδομένων και διατήρησε την απόδοσή του. Είναι ιδιαίτερα πιο επεκτάσιμος από τον αλγόριθμο DQN επειδή ο πίνακας Q δεν είναι επεκτάσιμος όταν υπάρχουν μεγάλα, υψηλών διαστάσεων και συνεχή ζευγάρια κατάστασης-ενέργειας.

Στο Σχήμα 7, απεικονίζονται η προβλεπόμενη μέση χωρητικότητα (α) και η συνάρτηση περιορισμού (β). Στο Σχήμα 8, οι μέσες ισχύες απεικονίζονται για τον προτεινόμενο, τον εποπτευόμενο, τον DQN, τον ίσης ισχύος, και τον τυχαίας ισχύος αλγορίθμους.

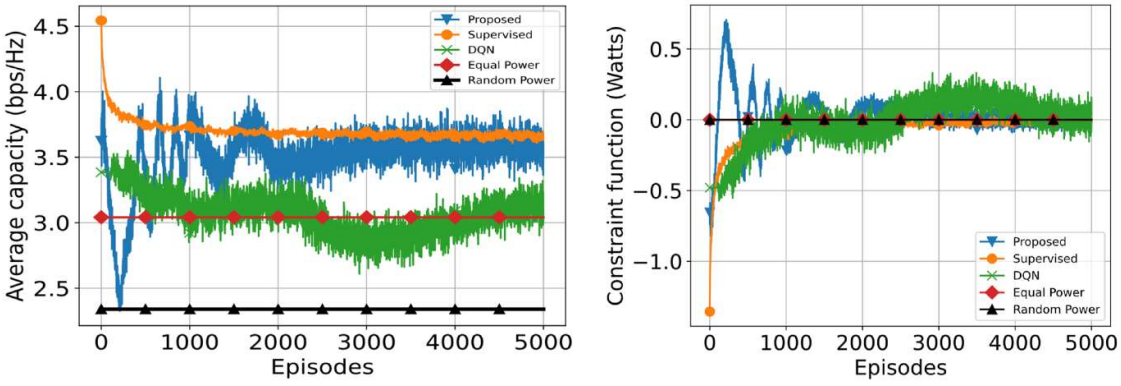

(α) (β)

Σχήμα 7: Επεισόδια μάθησης πέντε διαφορετικών αλγορίθμων κατανομής ισχύος: (α) η μέση χωρητικότητα του συστήματος και (β) η συνάρτηση περιορισμού.

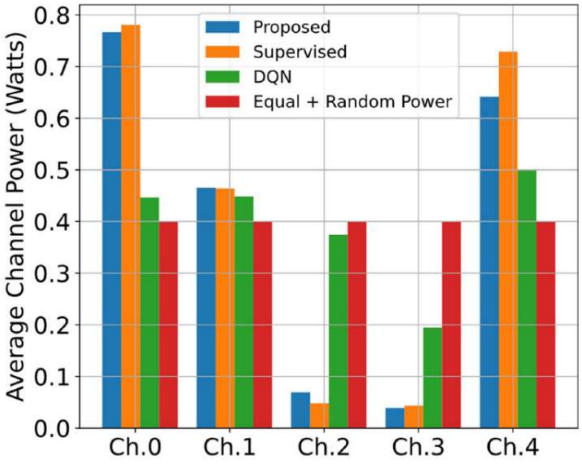

Σχήμα 8: Οι μέσες ισχύες καναλιού πέντε διαφορετικών αλγορίθμων κατανομής ισχύος κατά τη διάρκεια 5000 επεισοδίων.

1.7 Συμπεράσματα – Προεκτάσεις

Στο Κεφάλαιο 8 παρουσιάζεται μια σύνοψη των μεθοδολογιών που αναπτύχθηκαν στο πλαίσιο της παρούσας Διδακτορικής Διατριβής και δίνονται προτάσεις μελλοντική έρευνας.

Ανακεφαλαιώνοντας, στο Κεφάλαιο 2 γίνεται μια εισαγωγή στα επίγεια δίκτυα 5G και αναφέρονται τα σενάρια χρήσης, οι τεχνικές προδιαγραφές, οι προσφερόμενες υπηρεσίες, οι τελευταίες εξελίξεις καθώς και ο δρόμος προς το B5G και 6G. Ιδιαίτερη έμφαση δίνεται στις δορυφορικές επικοινωνίες και στις οπτικές επικοινωνίες ελευθέρου χώρου, οι οποίες απασχολούν εξ ’ολοκλήρου την παρούσα Διατριβή.

Στο Κεφάλαιο 3 δίνεται μεθοδολογία δημιουργίας χρονοσειρών λαμβανόμενης ισχύος για μια οπτική δορυφορική ζεύξη. Το μαθηματικό μοντέλο λαμβάνει υπόψη τα ατμοσφαιρικά φαινόμενα στροβιλισμού και σπινθηρισμού. Για τη μοντελοποίηση χρησιμοποιούνται στοχαστικές διαφορικές εξισώσεις. Η προτεινόμενη γεννήτρια χρονοσειρών συγκρίνεται με πειραματικά δεδομένα από το πρόγραμμα ARTEMIS με πολύ μεγάλη επιτυχία. Συγκεκριμένα, παρουσιάζεται εκτενής επικύρωση της γεννήτριας χρονοσειρών χρησιμοποιώντας στατιστικά αποτελέσματα τόσο πρώτης όσο και δεύτερης τάξης και επισημαίνεται η χρήση της για προσομοίωση και μοντελοποίηση σε επίπεδο συστήματος. Παρουσιάζονται προσομοιωμένα στατιστικά ισχύος λήψης για διάφορες καιρικές συνθήκες.

Στο Κεφάλαιο 4 προτείνεται μια μεθοδολογία κατανομής ισχύος για μια πολυκαναλική οπτική δορυφορική κατερχόμενη ζεύξη. Η μεθοδολογία βασίζεται σε κυρτές μεθόδους βελτιστοποίησης και στον αλγόριθμο υδροπλήρωσης. Παρουσιάζονται προσομοιωμένα αποτελέσματα κατανομής ισχύος χρησιμοποιώντας πραγματικά δεδομένα από το πείραμα ARTEMIS και διερευνάται η απόδοση του προτεινόμενου αλγορίθμου. Η προτεινόμενη μεθοδολογία αξιολογείται μέσω εκτεταμένων αποτελεσμάτων προσομοίωσης και συγκρίνεται ως προς την χωρητικότητα με δύο άλλους αλγόριθμους κατανομής ισχύος. Ακόμα, διερευνάται το πρόβλημα βελτιστοποίησης ισχύος για ένα οπτικό υβριδικό δίκτυο με μια δορυφορική πηγή, μια οπτική πύλη εδάφους και τον εξοπλισμό χρήστη. Το πρόβλημα κατανομής ισχύος είναι κυρτό υπό περιορισμούς ισχύος και προτείνεται μεθοδολογία συνυπολογίζοντας τη συσχέτιση του καναλιού και τα φαινόμενα στροβιλισμού. Η απόδοση της μεθόδου αξιολογείται μέσω αριθμητικών προσομοιώσεων.

Στο Κεφάλαιο 5 προτείνεται μεθοδολογία κατανομής ισχύος για οπτικές κατερχόμενες ζεύξεις LEO που χρησιμοποιούν HARQ. Το πρόβλημα βελτιστοποίησης είναι πρόβλημα περιορισμένου μη γραμμικού προγραμματισμού και επιλύεται για τα Type I, CC και IR. Οι

λύσεις δίνονται μέσω επαναληπτικών αλγορίθμων, δηλαδή IP και SQP, και επικυρώνονται μέσω εξαντλητικής αναζήτησης. Παρουσιάζονται αριθμητικά αποτελέσματα.

Στο Κεφάλαιο 6 διερευνάται μια εύρωστη στρατηγική κατανομής ισχύος για την κατερχόμενη ζεύξη οπτικού δορυφορικού συστήματος με διακύμανση στόχευσης και διατυπώνεται ένα πρόβλημα μεγιστοποίησης της χειρότερης χωρητικότητας δικτύου. Η βελτιστοποίηση πραγματοποιείται υπό περιορισμούς ισχύος με κυρτές τεχνικές και μετρήσεις από το πείραμα ARTEMIS. Εξάγεται το κατώτερο όριο εργοδικής χωρητικότητας δικτύου. Οι αλγόριθμοι συγκρίνονται με άλλες πολιτικές κατανομής ισχύος.

Τέλος στο Κεφάλαιο 7 παρουσιάζεται μεθοδολογία κατανομής ισχύος για οπτικά δορυφορικά συστήματα βασισμένη στη DRL και στα DNNs, η οποία εκπαιδεύεται χωρίς μοντέλο μέσω μιας στοχαστικής κλίσης πολιτικής. Για την επικύρωση και τη δοκιμή του προτεινόμενου σχήματος κατανομής, χρησιμοποιούνται πειραματικές μετρήσεις από την αποστολή ARTEMIS και ελέγχεται ως προς την ακρίβεια πρόβλεψης.

Διάφορες κατευθύνσεις για μελλοντική έρευνα μπορούν να προταθούν με βάση τις θεωρούμενες παραδοχές και απλοποιήσεις κατά την ανάπτυξη των μαθηματικών μοντέλων, των αλγορίθμων μοντελοποίησης και βελτιστοποίησης κατά τη διάρκεια αυτής της Διατριβής. Αυτές οι κατευθύνσεις παρατίθενται παρακάτω:

1. Μοντελοποίηση μέτριου/ισχυρού σπινθηρισμού σε δορυφόρους μη γεωστατικής τροχιάς

Για τη σύνθεση χρονοσειρών που μοντελοποιούν τα αποτελέσματα των ασθενών ατμοσφαιρικών αναταράξεων στην κατερχόμενη ζεύξη, θα μπορούσε να αναπτυχθεί μια αντίστοιχη μεθοδολογία παραγωγής βασισμένη σε στοχαστικές διαφορικές εξισώσεις για μέτριες και ισχυρές συνθήκες σπινθηρισμού. Ομοίως, οι μη γεωστατικοί δορυφόροι (δορυφόροι χαμηλής και μέσης γήινης τροχιάς) παρουσιάζουν μεγάλο ενδιαφέρον, αλλά το ίδιο έχουν και οι περιπτώσεις των ζεύξεων drone-to-ground, UAV-to-ground και CubeSat-to-ground. Οι κύριες προκλήσεις είναι η μικρότερη περίοδος περιστροφής και ο χρόνος οπτικής επαφής (< 24 ώρες, μερικές φορές και μερικά λεπτά), ο συχνός κύκλος ημέρας-νύχτας (στο σκοτάδι > 2% του χρόνου), η ταχέως μεταβαλλόμενη γωνία ανύψωσης, η ανάγκη για καλύτερη οπτική στόχευση και παρακολούθηση, η υψηλή ταχύτητα διαδρομής (> 10.000 mph) και τα χειρότερα φαινόμενα περιπλάνησης δέσμης και άμβλυνσης στροβιλισμών. Μπορούν να χρησιμοποιηθούν προσομοιωμένα ή ακόμα και πραγματικά οπτικά δορυφορικά δεδομένα.

2. Μη κυρτά και NP-δύσκολα προβλήματα κατανομής ισχύος

Η εύρεση ευρετικών και μεταευρετικών μεθόδων για προβλήματα βελτιστοποίησης μη κυρτών και NP-δύσκολων, καθώς και η μελέτη της βέλτιστης κατανομής ισχύος σε οπτικά δορυφορικά συστήματα μαζικών MIMO, μη ορθογώνιας πολλαπλής πρόσβασης (Non-Orthogonal Multiple Access, NOMA), αστερισμού δορυφόρων κ.λπ., είναι άλλες πιθανές εφαρμογές αυτής της έρευνας. Για παράδειγμα, η μεγιστοποίηση της ενεργειακής απόδοσης είναι ένα κρίσιμο ζήτημα στα συστήματα NOMA και διατυπώνεται ως NP-δύσκολο πρόβλημα βελτιστοποίησης υπό τη μέγιστη ισχύ μετάδοσης, την απαίτηση ελάχιστου ρυθμού μετάδοσης δεδομένων χρήστη και την απαίτηση διαδοχικής ακύρωσης παρεμβολών. Επίσης, το μη-κυρτό πρόβλημα κατανομής ισχύος σε ενοποιημένα 6G δορυφορικά και επίγεια (integrated 6G satellite-terrestrial) λόγω της εγγενούς μη-κυρτότητας της αντικειμενικής συνάρτησης. Η λύση πρέπει να επιδεικνύει υψηλή επεκτασιμότητα και αποτελεσματικότητα και χαμηλή πολυπλοκότητα. Η διατύπωση του ίδιου του προβλήματος κατανομής ισχύος και οι προτεινόμενες τεχνικές για την επίλυσή του θα είναι το κύριο επίκεντρο της μελλοντικής εργασίας. Η ορολογία που χρησιμοποιείται σε αυτή τη διδακτορική διατριβή είναι ευρεία και υποθέτει ότι προηγούμενες ενέργειες ή καταστάσεις δεν προβλέπουν μελλοντικές καταστάσεις. Ωστόσο, υπάρχουν ενδιαφέρουσες περιστάσεις στις οποίες αυτό δεν συμβαίνει, π.χ., ένα μοντέλο οπτικού καναλιού που ενσωματώνει ένα μοντέλο Markov όπου η κατάσταση καναλιού σε μια χρονική στιγμή εξαρτάται από τις προηγούμενες στιγμές. Ομοίως, τα προβλήματα αναλογικής δικαιοσύνης λαμβάνουν υπόψη μια επιπλέον κατάσταση που σχετίζεται με τις προηγούμενες κατανεμημένες ισχύες των τερματικών εκπομπών.

3. Ανάλυση απόδοσης σε άλλα θέματα οπτικής διάδοσης ανερχόμενων ζεύξεων με μικρούς δορυφόρους ή μη επανδρωμένα αεροχήματα.

Η περιπλάνηση δέσμης (beam wander) είναι μια σημαντική πρόκληση στην ανοδική ζεύξη, καθώς έχει ως αποτέλεσμα τη μετατόπιση της δέσμης κατά αρκετές εκατοντάδες μέτρα. Κατά την διασπορά δέσμης (beam spreading) η εισερχόμενη δέσμη θα περιθλαθεί και θα διασκορπιστεί ανεξάρτητα, οδηγώντας σε παραμόρφωση του λαμβανόμενου μετώπου κύματος. Για την ανοδική ζεύξη, η διασπορά δέσμης, η περιπλάνηση δέσμης και οι διακυμάνσεις στη γωνία άφιξης είναι οι κύριοι παράγοντες που συμβάλλουν στην υποβάθμιση του σήματος και έτσι δημιουργούν ένα πιο πολύπλοκο πρόβλημα βελτιστοποίησης ανάθεσης ισχύος. Ακόμη, οι νανοδορυφόροι LEO με μικροσκοπικά τηλεσκόπια των ~9 cm μπορούν να κάνουν κύκλους γύρω από τη Γη γρήγορα σε περίπου 90 λεπτά ενώ οι πλατφόρμες CubeSat έχουν διάρκεια ζωής από μερικές εβδομάδες έως 1-2

χρόνια. Τα drones υποφέρουν από δονήσεις πλατφόρμας λόγω των πτερυγίων του ρότορα του drone και επειδή αιωρούνται τυχαία λόγω των τοπικών ριπών ανέμων και της ακρίβειας GPS. Είναι ανάγκη συνεπώς να μελετηθούν βέλτιστα ή εύρωστα σχήματα κατανομής ισχύος και να πραγματοποιηθεί μια ανάλυση απόδοσης των συστημάτων αυτών με προσομοιωμένα ή και πειραματικά δεδομένα.

Τέλος, ιδιαίτερο ενδιαφέρον έχουν τα προσαρμοστικά οπτικά (Adaptive Optics, AO), τα οποία χρησιμοποιούνται για την άμβλυνση της επίδρασης των ατμοσφαιρικών αναταράξεων και στην παροχή μιας μη παραμορφωμένης δέσμης. Ομοίως, στα πλαίσια της μελλοντικής έρευνας είναι και η ανάλυση απόδοσης των AO σε διάφορες συνθήκες στροβιλισμών με πειραματικές μετρήσεις αν είναι εφικτό.

4. Μηχανική μάθηση και νευρωνικά δίκτυα

Οι συμβατικές και κλασικές μέθοδοι βελτιστοποίησης εξακολουθούν να επιδεικνύουν πλεονεκτήματα στη βελτιστοποίηση της κατανομής ισχύος των τύπων ασύρματων δικτύων. Ωστόσο, απαιτούν πολύπλοκες και εντατικές επαναλήψεις και μπορεί να είναι υποβέλτιστες. Από την άλλη πλευρά, η μηχανική μάθηση (ML) έχει πολλές υποσχέσεις για την επίλυση προβλημάτων που δύσκολα μοντελοποιούνται και τη μεταφορά επίπονων και υπολογιστικά δαπανηρών διαδικασιών βελτιστοποίησης σε εκπαίδευση εκτός σύνδεσης. Για το λόγο αυτό, και με την εκθετική αύξηση του αριθμού των διαθέσιμων συνόλων δεδομένων, η ML έχει γίνει μια θεμελιώδης τεχνολογία σε διάφορους τομείς των ασύρματων επικοινωνιών, και ειδικότερα στη βέλτιστη κατανομή ισχύος. Εκτός από τα βαθιά νευρωνικά δίκτυα (DNN), λύσεις με αρχιτεκτονικές επαναλαμβανόμενων νευρωνικών δικτύων (RNNs), νευρωνικών δικτύων γραφημάτων (GNNs), συνελικτικών νευρωνικών δικτύων (CNN) και τεχνικών βαθιάς ενισχυτικής μάθησης (DRL) θα μπορούσαν να διερευνηθούν σε κατανεμημένα περιβάλλοντα πολλαπλών πρακτόρων.

5. Λήψη δεδομένων εκπαίδευσης και εφαρμογή στο πραγματικό σύστημα

Δεδομένου ότι οι τεχνικές μηχανικής μάθησης απαιτούν τη συλλογή άφθονων ποσοτήτων δεδομένων υψηλής ποιότητας εκτός από τα προφίλ δικτύου, συναντούν πολλά εμπόδια σε όλη τη φάση της εκπαίδευσης. Για παράδειγμα, σωστά χαρακτηρισμένα δεδομένα απαιτούνται για συστήματα επιτηρούμενης μάθησης, αλλά αυτό μπορεί να είναι δύσκολο να επιτευχθεί σε ένα περιβάλλον που αλλάζει γρήγορα. Ορισμένες μέθοδοι βασίζονται σε προσομοιωμένα σύνολα δεδομένων που δημιουργούνται χρησιμοποιώντας ένα συγκεκριμένο είδος δικτύου. Ως αποτέλεσμα, θα μπορούσε να υπάρξει ασυμφωνία μεταξύ της βέλτιστης

προσέγγισης που λειτουργεί σε ένα πραγματικό σύστημα και της καθιερωμένης μεθόδου. Η ανάγκη και το κόστος των οπτικών δορυφορικών αλλά και επίγειων μετρήσεων θα γίνονται όλο και πιο δύσκολα καθώς τα ασύρματα οπτικά δίκτυα γίνονται πιο πυκνά και απαιτητικά στο μέλλον.

6. Ασφαλείς επικοινωνίες

Οι συσκευές είναι δικτυωμένες για ανίχνευση και αλληλεπίδραση σε πραγματικό χρόνο στην εποχή του Internet of Things. Θα πρέπει να αποτρέπεται η πρόσβαση σε ιδιωτικά δεδομένα, συμπεριλαμβανομένων των πληροφοριών τραπεζικών λογαριασμών και των αρχείων υγειονομικής περίθαλψης, από κινδύνους για την ασφάλεια του δικτύου, όπως η υποκλοπή και η παρεμβολή. Τα ασύρματα δίκτυα επόμενης γενιάς θα πρέπει να αντιμετωπίσουν ζητήματα όπως ο κυβερνοπόλεμος, η κλοπή δεδομένων cloud και το phishing, τα οποία θα έχουν σημαντική επίδραση στον τρόπο προστασίας της ανταλλαγής δεδομένων με τρόπο που να διατηρεί τόσο το απόρρητο όσο και τη δικαιοσύνη.

Η οπτική ζεύξη ελεύθερου χώρου έχει εγγενή χαρακτηριστικά ασφαλείας και μπορεί να υποστηρίξει κβαντική κρυπτογραφία όταν η υποδομή οπτικών ινών δεν είναι διαθέσιμη. Η διανομή κβαντικού κλειδιού (Quantum Key Distribution, QKD) είναι μια πολλά υποσχόμενη τεχνολογία που επιτυγχάνει άνευ όρων ασφάλεια, η οποία είναι απαραίτητη για ένα ευρύ φάσμα ευαίσθητων εφαρμογών. Σε αντίθεση με την οπτική ίνα, η επικοινωνία FSO χρησιμοποιείται αποτελεσματικά ως κβαντικό κανάλι χωρίς να επηρεάζεται η πόλωση των μεταδιδόμενων φωτονίων. Δυστυχώς, όλες οι παραδοσιακές προσεγγίσεις διανομής κλειδιών είναι εγγενώς απρόβλεπτες, καθώς βασίζονται εξ ολοκλήρου σε υπολογιστικούς μηχανισμούς που είναι ευάλωτοι σε μελλοντικές εξελίξεις στο υλικό και τους αλγόριθμους υπολογιστών. Με την εκθετική ανάπτυξη των κβαντικών υπολογιστών, αναμένεται ότι η υπάρχουσα υποδομή δημόσιου κλειδιού θα γίνει πιο ευάλωτη μέσα σε λίγα χρόνια λόγω της διαθεσιμότητας κβαντικών υπολογιστών μεγάλης κλίμακας. Ένας κβαντικός δορυφόρος GEO μπορεί να παρέχει έναν αργό αλλά συνεχή ρυθμό παραγωγής μυστικού κλειδιού, λόγω της σταθερής του θέσης στον ουρανό σε πολύ μεγάλο υψόμετρο. Αντίθετα, οι κβαντικοί δορυφόροι LEO είναι πολύ πιο κοντά στην επιφάνεια της Γης και, λόγω αυτού, μπορούν να παρέχουν μια ταχύτερη αλλά διακοπτόμενη υπηρεσία παραγωγής μυστικών κλειδιών.

Στην περίπτωση ενός κβαντικού δορυφόρου, το πρόβλημα κατανομής πόρων ανάγεται λοιπόν στη βελτιστοποίηση της συνάρτησης στόχου, όπως η μεγιστοποίηση των ροών κλειδιών και η ελαχιστοποίηση της κατανάλωσης μυστικού κλειδιού.

Chapter 2
Introduction

2.1 Overview of 5G Mobile Networks and Future Wireless Communications

Since its commercial launch in 2019, fifth-generation (5G) coverage has grown to reach 40% of the world's population by 2023 (Figure 2-1). However, distribution remains extremely uneven. While 5G networks cover 89% of the population in high-income nations, coverage in low-income countries remains sporadic. With 68% of the population covered, Europe has the most comprehensive 5G coverage, followed by the Americas (59%) and the Asia-Pacific area (42%) [1]. In the Arab States area, coverage exceeds 12% of the population, while it is below 10 percent in the CIS region (8%) and Africa (6%) [1]. 4G covers 90% of the world's population, and where 5G isn't accessible, this remains an excellent alternative. However, 55% of those without 4G reside in low-income nations [1].

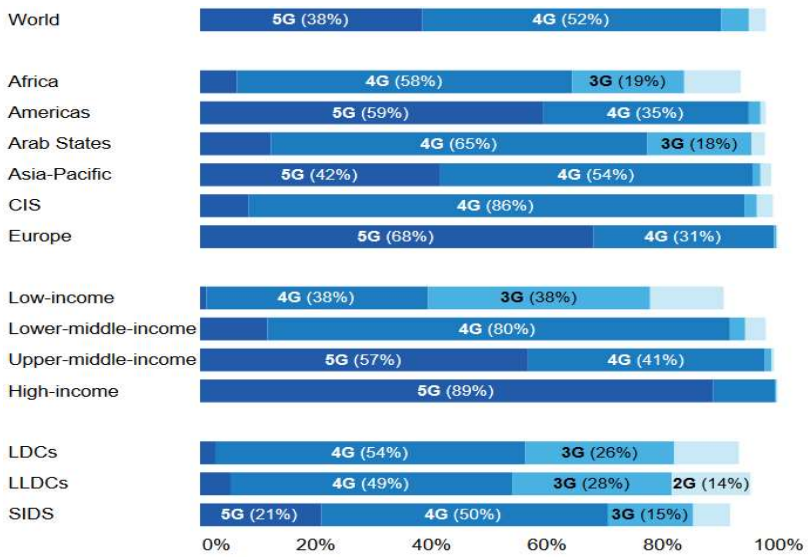

Figure 2-1: Population coverage by type of mobile network (2023) [1].

Global mobile-broadband traffic rates are expected to reach 913 exabytes (EB) in 2022, more than double the traffic in 2019 [1]. Fixed broadband traffic rates were expected to have climbed from 1991 EB in 2019 to 4378 EB in 2022 (almost five times that of mobile broadband traffic) [1]. Between 2019 and 2023, mobile and fixed-broadband traffic is expected to climb at a 30% yearly average, with a peak rate of growth around the onset of the COVID-19 pandemic in 2020 [1]. For significant Internet data usage, fixed broadband remains the option of choice. During the epidemic, a significant portion of mobile traffic was

diverted through fixed networks using Wi-Fi connections. In 2022, the mobile-broadband traffic had grown from 3.4% to 4.2% [1].

5G network requirements have successfully completed the standardization phase, and 5G-powered networks are being deployed globally [2]. The International Telecommunication Union (ITU) certified in November 2020 that the 5G New Radio (NR) and 5G Core technologies proposed by the Third Generation Partnership Project (3GPP) meet the IMT-2020 performance criteria [3].

The first 5G deployment (2019-2020) will focus on sub-6 GHz cells built on a cloud radio access network (C-RAN) architecture [4]. However, following rollouts will cover the complete 5G vision, including the hyperdense deployment of small cells based on millimetre-wave frequencies. This will be combined with extensive deployments of multiple antenna technology, which will have a multiplier impact on user peak data rates and cell capacity, allowing the 5G system to meet the performance metrics established by 3GPP [5].

In the direction of a society that is fully connected and an acceleration of the digital transformation, three primary use cases for 5G have been considered, namely, enhanced mobile broadband (eMBB), massive machine-type communications (mMTC), and ultra-reliable low-latency communications (URLLC) [2–6].

1. The eMBB aims to improve speed, capacity, coverage, broadband connectivity of 5G mobile networks to accommodate the escalating data traffic generated by mobile smartphones (e.g. high-grade photos and videos) and provide innovative applications such as augmented reality/virtual reality (AR/VR). The objective is to reach up to 10–20 Gbps mobile data rates offering connectivity in densely populated areas and events [2–6].
2. The mMTC use case intends to address difficulties, for example, connecting billions of machines or resource-restricted Internet of Things (IoT) units (e.g. sensors, actuators) to the network as new clients [2–6].
3. The URLLC focuses on supporting latency-critical applications, for example, autonomous driving, vehicle-to-everything (V2X) communications, vehicle-to vehicle (V2V), vehicle-to-infrastructure (V2I), unmanned aerial vehicles (UAV), intelligent transportation system (ITS), and smart grid, smart manufacturing, precision farming, railways. This use case aims to reduce the radio access network latency from 20 ms in 4G to 5 ms and eventually to less than 1 ms [2–6].

With its constituents being the software defined network (SDN), network functioning virtualization (NFV), network slicing (NS), mobile edge computing (MEC), massive multiple-input/multiple-output (MIMO), and millimeter-wave (mmW), the 5G mobile

network is primarily built on softwarization [6]. More than 100 times as many connected devices and greater "indoor coverage" are now possible due to 5G's improved energy efficiency and signal propagation attributes. Additionally, the "traffic density" will improve energy and spectral efficiency. Furthermore, this has sparked the development of new technological paradigms, such as Industry 4.0, edge intelligence (EI), nonorthogonal multiple access (NOMA), mixed reality (MR), driverless cars, Internet of Everything (IoE), and big intelligent surfaces (LIS). Conversely, novel and developing uses like extended reality (XR), unmanned aerial vehicles (UAV), and holographic telepresence (HT) are probably going to change the course of the future [6]. However, because they are bandwidth-hungry, these apps demand things like maximum speed, instantaneous access, low latency, etc., which 5G cannot provide. Densely networked wireless devices from a variety of application areas in transportation, industry, and health provide the foundation of the 5G ecosystem [2–6].

Since the advent of these novel ideas and technology, wireless backhauling has gained prominence in networks of the future, allowing densification with higher performance than that of earlier methods [7]. The usage of wireless connections for core network connectivity—for which fiber cables are often used—is known as wireless backhauling [7]. However, the performance requirements were no longer a constraint with the advent of mmW frequency, mMIMO, and beamforming. Furthermore, the fact that mmW is a fresh frequency band made it easier to use available spectrum resources, enabling wireless backhauling [7]. The deployment of a dense network with fiber connectivity is nearly difficult, which makes wireless backhauling necessary and important. Finally, there are a number of use-cases that stand to gain greatly from the widespread realization of wireless backhaul utilization. The usage of UAV and satellite backhauling are explicitly relied on wireless backhauling performance [7].

It is anticipated that 6G would differ from 5G in a number of ways. In terms of application needs, 5G expanded 4G's "Mobile Internet" to include the "IoE." 6G will build on 5G to further improve the IoE and mobile Internet while also extensively integrating them with big data and artificial intelligence to create an intelligent IoE [2–6]. Technically speaking, 6G will aim for more coverage, faster speeds, more connections, ultra-low latency, ultra-high positional precision, communications and sensing integration, increased intelligence, increased security, and improved substitutability over 5G [2–6].

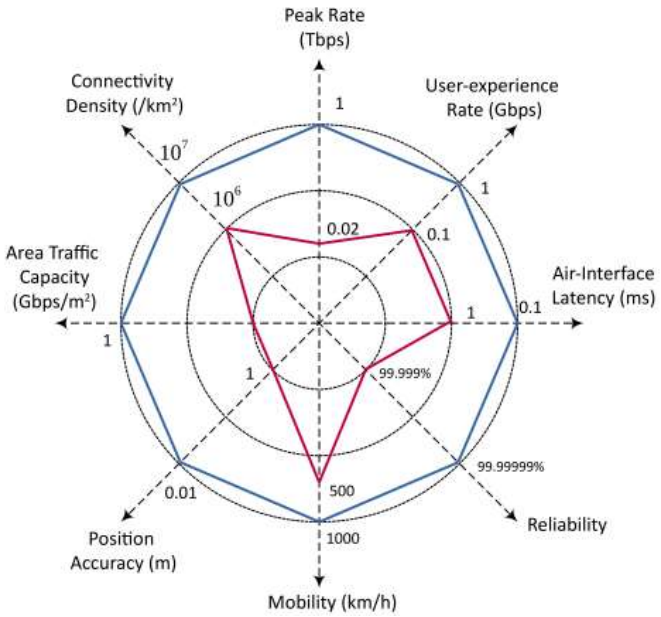

Figure 2-2: Technical requirements of 5G vs 6G. The inner polygon stands for 5G, while the outer octagon stands for 6G [3].

In Figure 2-2 the technical requirements of 5G are compared to the 6G ones [3]. While 5G can only achieve a maximum downlink rate of 20 Gbps and an uplink rate of 10 Gbps, 6G is predicted to attain speeds of up to 1 Tbps [3]. The minimum user layer latency in 5G is 1 ms for URLLC and 4 ms for eMBB. It is anticipated that this figure would fall considerably lower, to 100 µs or even 10 µs. The downlink and uplink maximum spectral efficiencies for 5G are 30 bps/Hz and 15 bps/Hz, respectively. Advanced 5G radio technologies are expected to attain a spectral efficiency that is three times lower than that of 6G. The chance of success for the minimum dependability criterion in 5G networks is $1-10^{-5}$. Improvements of at least two orders of magnitude are anticipated, i.e. $1 - 10^{-7}$ or 99.99999 %. Finally, the bandwidth requirement in 5G is at least 100 MHz while 6G will support up to 1 GHz [3]. The following five use cases look very promising for B5G/6G [2–6]:

1. Holographic telepresence enables real-time verbal communications along with realistic, full-motion, 3D images of far-off people and things that may be projected into a room (such as a meeting room, classroom, or surgical area).
2. A digital twin enables the creation of an executable, full, and real-time digital duplicate of a property, system, or subsystem (smart grid, Industry 4.0, for example).
3. Autonomous cars and connected robots enable the physical process, controller, sensors, actuators, and other components of a control system that are dispersed across a large

geographic area to be connected via a mobile infrastructure. Tactile Internet is a new use case for this application.

4. The goal of Internet of Things (IoT), distributed artificial intelligence (AI), and big data is to enable mobile networks to automate network functions through the use of AI, machine learning (ML), and big data technologies.
5. Blockchain has great promise for B5G/6G data storage as it provides decentralized, permanent, anonymous, and auditable repository of information.

Key technologies that are anticipated to propel the mobile industry toward B5G/6G include distributed artificial intelligence (AI) and big data, virtualized RAN, quantum and THz communications, visible light communication (VLC), energy harvesting and fog computing, and improved optical-wireless convergence [2–6].

One of the main ways that machine intelligence manifests itself is through ML [8–10]. In ML, a mathematical model is constructed to carry out a certain function (such as classification, regression, or clustering) without the need for explicit programming. The following are the three primary categories of ML [8–10]:

1. To learn a specific unknown mapping function that maps the input to the output, supervised learning makes use of a labeled data set, which contains both the input and the desired outcome [8–10]. In other words, after the model is trained on solved cases, it can forecast the result depending on fresh inputs. Artificial neural networks (ANNs), support vector machines (SVMs), k-nearest neighbours (KNN), and logistic regression are the main models used in supervised learning [8–10].
2. In unsupervised learning, the data is unlabeled (i.e., it merely consists of inputs), but the model must determine the underlying structure in the data [8–10]. The grouping of data into clusters based on shared characteristics is a good illustration of unsupervised learning. For instance, k-means clustering, principal component analysis (PCA), and Gaussian mixture model (GMM) utilize this learning approach [8–10].
3. The goal of reinforcement learning is for the agent to maximize the positive rewards from its interactions with the environment by assigning both positive and negative rewards to the actions it does [8–10]. As a result, no dataset is needed for training when using this learning technique. Q-learning, actor-critic learning, and multi-armed bandit learning are a few instances of algorithms that use reinforcement learning [8–10].

Benefits to be provided by using AI/ML in future 6G networks:

1. Overcoming modeling complications [8–10]: Due to the high mobility, the dynamic environment of space, the use of wireless links for most segments, the modelling of channels is very complicated in SpaceNets. The accuracy of these models has a significant impact on network performance and user satisfaction. However, ML techniques do not require accurate modeling.
2. Low computational and time complexity [8–10]: In the training phase, the model parameters are optimized to learn the structure of the data. This learning process is computationally complex. However, it can be implemented offline utilizing available data. During the testing phase, the trained model operates online with low complexity and a short response time. For instance, a trained ANN predicts the output for new inputs mainly by matrix multiplications. This reduces the computational complexity and response time during online operation. For example, it was shown that a trained deep neural network (DNN) could predict the power allocation for a network with 15 users in a response time of just 0.0149 ms.
3. Adaptability to dynamic environments [8–10]: SpaceNets are characterized by their highly dynamic environment. This includes a network topology that changes with time due to the movement of SNs, channel conditions that depend on the weather and location and traffic loads that differs from one spot to another. The development, configuration, and management of the network need to react to these changing conditions quickly and efficiently.
4. Scalability [8–10]: The increase in complexity when the network parameters scale up is lower than that of traditional approaches. This is suitable for SpaceNets which are required to serve a massive number of users per EOS as its footprint covers a wide area on the ground.

Challenges to be addressed to leverage the intelligence of AI/ML in future 6G networks:

1. Dataset availability [8–10]: High-quality data is essential for ML models, and their accuracy depends greatly on the amount of data used for training. In this regard, data for SpaceNets might not be available for all use cases due to cost or computational resource limits.
2. Suitable techniques [8–10]: There are numerous ML approaches that can be grouped under the three categories discussed in this section. Each technique has its own advantages and shortcomings. For example, supervised learning-based models can provide accurate

predictions for decision making. However, labeled data sets are required to train those models, which might not be available.

3. Distributed versus centralized [8–10]: To address scalability issues and avoid centralized processing shortcomings, distributed ML techniques, such as federated learning can be utilized. There is a trade-off between centralized and distributed ML techniques.
4. Standardization [8–10]: Despite the great interest that AI/ML has received, it is still in the study phase and is not widely standardized in wireless networks. In addition, AI/ML is included in the work items to be specified in Release 18. This means that AI/ML is beginning to find a place in wireless network standards. However, the technology is still in its infancy.
5. Unique characteristics of SpaceNets [8–10]: Compared with terrestrial networks, SpaceNets have unique characteristics that can impact the performance of AI/ML models and techniques. For example, the propagation delay in SpaceNets makes it challenging for AI/ML models to utilize such kind of data that could be outdated due to that delay. Another example is the highly dynamic topology or the communications environment in SpaceNets which makes the data susceptible to high errors due to pointing and polarization errors, weather conditions, radiation, and high interference.

Applications of AI/ML in future 6G networks:

1. Handover prediction and management [8–10]: Reinforcement learning is employed to design a user-centric handover method in which the user terminal makes decisions about the handover procedure based on predicted service time, channel resources, and relay overhead.
2. Routing [8–10]: An unsupervised learning technique to define clusters of traffic based on their data type while taking into account the geographical traffic distribution density. Then, a reinforcement learning approach was applied to learn following the replays and selecting the route with the lowest round-trip time.
3. Channel modelling and estimation [8–10]: A deep learning-based channel state information predictor for massive MIMO-based LEO satellite communications. The model was based on long short term with memory (LSTM).
4. Resource allocation [8–10]: In a resource allocation problem based on NOMA, deep learning is used to study the relationship between the queue and channel states and overcome the non-convexity of the power allocation problem.

5. At PHY, many optimization problems are nonconvex, e.g., sum-rate maximization. ML is a powerful tool to find good solution(s) for such nonconvex optimization problems. An Introduction to Deep Learning for the Physical Layer can be found in [11].

2.2 Overview of Satellite Communications

Unmanned aerial vehicles (UAVs), high altitude platforms (HAPs), and satellite networks are examples of non-terrestrial networks (NTNs) [12–16]. NTNs have historically been utilized for a variety of purposes, including remote sensing, television broadcasting, disaster management, and navigation. The development of terrestrial networks (TNs) in isolated or unreachable locations, such as rural areas, deserts, and oceans, may be prohibited by the inherent limits of ground infrastructure as well as by financial considerations [12–16]. User equipment (UE) in these un(der)served areas are consequently unable to receive terrestrial services. Network scalability may be made possible by the employment of NTNs in conjunction with the current terrestrial infrastructure as a practical and affordable solution for constant and widespread wireless coverage. In these situations, NTNs serve as access nodes to improve the capacity, coverage, reliability, delay, widespread presence, and overall performance of the current and future terrestrial networks [12–16].

For starters, NTNs can successfully improve "5G network reliability" by ensuring service continuity in circumstances where it cannot be provided by one or more types of terrestrial networks [12–16]. As an example, consider moving platforms (e.g., a vehicle, train, or airplane) with mission-critical communications. Secondly, NTNs can ensure "5G service ubiquity" in un-served (e.g., deserts, oceans, forests) or under-served (e.g., metropolitan regions) locations where a terrestrial network does not exist or is prohibitive to reach [12–16]. Last but not least, NTN can provide "5G service scalability" owing to the satellites' efficiency in multicasting or broadcasting over a large area. This can be quite effective for offloading the terrestrial network by broadcasting media to the network's edge [12–16].

Satellites have the unique ability to cover large geographical areas with minimal ground infrastructure, making them an appealing solution to meet the growing number of diverse applications and services, either as a stand-alone system or as an incorporated satellite-terrestrial network [17]. Satellite communications is currently gaining traction in the global telecommunications sector, as numerous network operators have begun to use satellites in backhauling infrastructures for connection and 5G system integration [18].

Because they are at such a high altitude, these satellites have such a large communication area that three GEO satellites may cover the entire planet. MEOs are found at altitudes ranging from 5,000 to 20,000 kilometres [19]. The Global Navigation Satellite System (GNSS) is one example, i.e., GPS and Galileo, or SES's o3b mPower system. LEOs are found at altitudes ranging from 500 to 1,500 kilometres. MEO and LEO differ from GEOs in several ways [20]. For starters, because they are lower in height than GEOs, they have substantially shorter propagation delay times and less propagation attenuation. Their high mobility, on the other hand, creates a large Doppler shift, therefore signal distortion must be considered [19]. The overall number of active satellites circling the Earth in 2016 was 1,459. Nonetheless, the number of operating satellites had increased to 4,550 by September 2021 (a more than 210% increase in less than 5 years). Furthermore, over 100,000 satellites are expected to be launched by 2030 [20]. Table 2-1 provides several examples of LEO-satellite constellations whose services have commenced or are scheduled to commence in the near future, demonstrating the strong trend towards these constellations.

Table 2-1: Satellite Constellations [43]

Company	**Service started**	**# of satellites**
O3b	2014	12
Oneweb	2023	648
Starlink	2020	12000
Telesat	2023	188
Iridium-next	2018	66

The high throughput satellite (HTS) system, which was deployed in 2011, offers high throughput service by leveraging a multi-beam layout but has the problem of supporting a relatively small area when compared to standard SatCom [21–22]. Many studies have been undertaken since then to discover a MIMO design that can use the multi-beam method for most SatCom designs [23–27].

SatCom channels differ substantially from those of the terrestrial network. There are two notable differences [28]: 1) significant signal attenuation and extended delay times due to great distances, and 2) high LoS channel properties. The enormous distance between the satellite and the earth causes significant signal attenuation. Path loss, attenuation caused by the Earth's atmosphere, and rainfall impacts are all examples of attenuation. Because there is no scatter near the satellite, signals coming from or going to it cannot take advantage of multi-

path [29]. Another concern is the significant Doppler shift. Satellites in MEO and LEO orbit at high speeds. For example, a satellite in 600 km LEO is traveling at 7.56 km/s. Motion at this rate will generate a significant Doppler shift in the signal path [30].

A satellite sends and receives data from the gateway [31]. At the same time, it sends and receives data from and from clients. SatCom is classified into two types: transparent and regenerative [32]. Transparent relay signals simply by amplifying the signal received from the gateway or user. The regenerative form, on the other hand, makes advantage of onboard processing (OBP). Thus, a regenerative satellite works similarly to a base station (BS) of the terrestrial infrastructure for switching and routing, modulation and demodulation, and coding [33]. The gateway and the satellite are connected via feeder links. The communication link between the user and the satellite is known as a service link. In the transparent scheme, OBP cannot be realized and inter-satellite links (ISL) are not supported. Consequently, the satellite should always have both a feeder and a service link.

Based on their features, each employed frequency band is separated into Ku, K, Ka, and V bands, which are fairly high frequency bands, and L, S, C, and X bands, which are comparatively low frequency bands [34]. In classic SatCom, the lower frequency bands are primarily utilized. GNSS and other navigation and tracking systems are the primary users of the L-band spectrum [35]. Television transmission, military communications, and high-capacity Internet connections all employ the relatively high frequency Ku, K, and Ka bands. This frequency range is specifically used for communication by LEO Internet service providers like OneWeb and Starlink, which recently started offering their services [36]. Recently, there has been talk about utilizing the V-band bandwidth for feeder links that have higher reliability and capacity demands [37].

The Ka and Ku bands are the bands that LEO enterprises are now using. Telesat operates in the 17.8–20.2 GHz downlink and 27.5–30 GHz uplink bands, both of which are Ka band frequencies [38]. OneWeb and Starlink use the 10.7-12.7 GHz spectrum for user downlink and the 14-14.5 GHz band for user uplink [39]. They also use the 17.8-19.3 GHz band for their gateway downlink and the 27.5-30 GHz Ka band for their gateway uplink. Regarding Amazon, it utilizes the 17.7–20.2 GHz Ka band for user downlink and gateway, the 27.5–30 GHz Ka band for gateway uplink, and the 28.35–30 GHz Ka band for user uplink. S (2–4 GHz), X (8–12 GHz), Ku (12–18 GHz) and Ka (26–40 GHz) are the frequency ranges utilized for satellite communications [40]. The need for higher data rates and restricted available spectrum is driving satellite operators to investigate the V (40–75 GHz) and W (75–110 GHz)

bands [41]. This move increases bandwidth for feeder links that can support a HTS and frees up Ka for the user link [42].

2.3 Overview of Free-Space Optical Communications

Due to its ability to meet the key requirements of high capacity, low latency, energy efficiency, dense connectivity, and a superior level of security against interception, free space optical communication (FSO) systems have recently attracted a lot of attention again as a viable wireless interconnecting solution for the 6G era [43]. As a possible wireless linking option, FSO systems—which transfer data through the air using infrared beams rather than radio waves or optical fibres—have recently garnered a lot of curiosity. They combine the benefits of the high transmission capacity made possible by optical device technologies with the mobility and convenience of deployment of the wireless networks. Furthermore, they are license-free and interference-free [44].

Despite being on the market for a while, three major problems have prevented the FSO systems from being implemented in the carrier-class networks of today [45]. These include of [46]:

1. Inherent system difficulties, like severe line-of-sight (LOS) requirements and meteorological disturbances.
2. The availability of radio frequency (RF) technologies like E-band mmW connectivity that could fulfil the present mobile network requirements.
3. Tight availability and reliability criteria enforced by telecom operators.

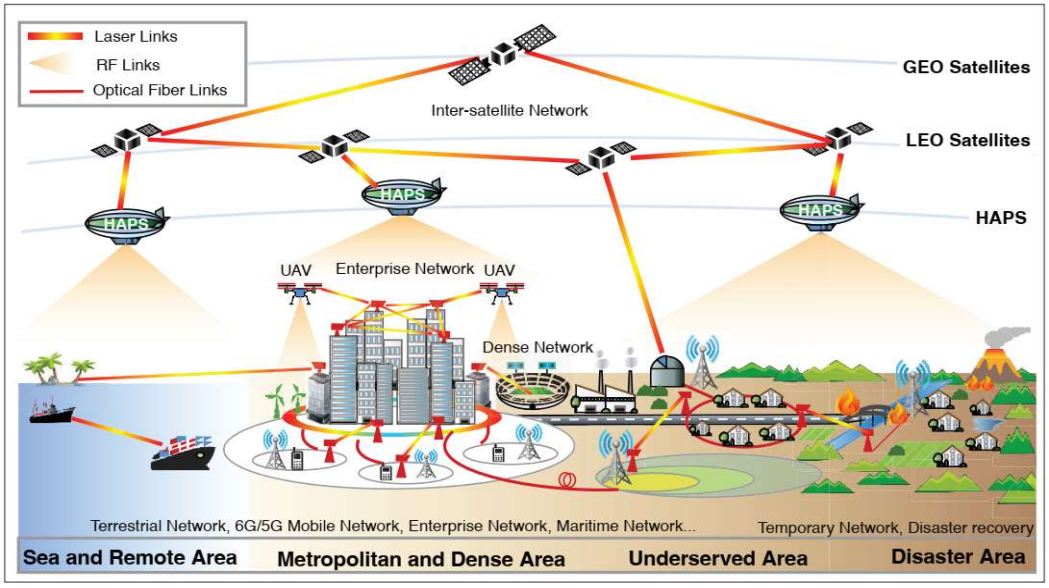

Figure 2-3: Potential applications of FSO systems in 6G network [47].

Lately, FSO systems have become a feasible choice for fulfilling the essential needs of 6G networks, which include high density connection, low latency, high capacity, energy efficiency, and high security (i.e., resistance to interception) [47]. It is true that the FSO communication bands are license- and interference-free, with transmission windows available in the 850 nm, 1310 nm, and 1550 nm [48]. Because FSO systems work with the current fibre infrastructure, they can provide a capacity that is similar to optical fibre at a much lower deployment cost [49]. The wireless capability of the FSO system allows for the expansion of Gb/s-class wireless coverage to the sea and space, as well as the establishment of flexible and robust communication links for rural, underserved, and disaster-affected areas [50].

Terrestrial, non-terrestrial, space, and deep-space are the four link subtypes that make up FSO. Building-to-building FSO links are instances of terrestrial FSO [51]. High altitude platform systems (HAPSs), HAPS-to-HAPS, and ground-to-UAVs are examples of non-terrestrial FSO linkages. Space FSO includes links that are satellite-to-satellite, satellite-to-ground, and satellite-to-satellite. A deep-space FSO link, such as the one established between Galileo and Earth, can be referred to as deep-space FSO. FSO links between satellites, often called laser intersatellite links (ISLs) [52]. Figure 2-3 illustrates all the possible FSO applications in future 6G networks.

The input data are transformed at the transmitter into a modulated electrical signal that modifies the laser current in the driver to adjust the laser's output light intensity. This modified laser beam is focused at the telescope at the receiver by the telescope at the transmitter [53]. After passing across the medium, this optical signal is picked up by the telescope of the receiver. This optical signal is converted to an electrical signal at the receiver by the photodetector, which is subsequently demodulated to recover the sent data. The background sun radiation is eliminated at the receiver via an optical filter. An FSO transmitter can employ a laser diode (LD), a light emitting diode (LED), or an array of LDs/LEDs. LDs discharge high-bandwidth coherent and razor-sharp light beams with a highly narrow divergence angle, in the order of milliradians. On the contrary, LEDs emit wide-beam light and enable multipoint connections, therefore suitable for short-range multicasting or broadcasting usages [54].

In order to prepare for the hazards revealed by quantum computing, quantum key distribution (QKD), a revolutionary technique for secret key agreement between authorized parties, purports to offer potential mitigation from the public cryptosystem [55]. Instead of relying on the notion that a mathematical problem is difficult, QKD's security is based on the principles of quantum mechanics, as opposed to traditional key distribution systems. Bennett

and Brassard devised the first QKD system in 1984 by encoding secret information on photons to securely transfer messages of Wiesner in 1983 [56].

The FSO/QKD system, which makes use of satellites, can make it possible for fixed and wireless users, including UAVs and driverless cars, to access global quantum networks [57]. Research has been done on the topic of FSO connection optimization, which includes bit error rate minimization, bandwidth maximization, and security against optical jamming. Additionally, because space lacks an atmosphere like Earth does, it offers ideal circumstances for optical communication. However, precise aiming is necessary for point-to-point optical transmission. Furthermore, the quantity of optical communication components that each satellite can have is restricted, and each component can only be connected to one satellite at a time [58].

Laser ISLs are envisioned between satellites in upcoming LEO satellite constellations. The RF links operate in Ka and mm-wave bands, and the transmit power is considered as 10, 20, and 50 W for FSO, mmW, and Ka links, respectively [59]. At a data rate of 2.5 Gb/s over an intersatellite distance of 5000 km, the RF ISL in either Ka or mm-wave bands requires at least 19 times the antenna diameter, and more than twice the onboard power and mass compared to an FSO ISL [60]. The small beam width is the main advantage of FSO as it eliminates interference from neighbours. However, in laser ISLs, the small beam width turns into a disadvantage.

Such demonstrations and solutions include the European Data Relay System (EDRS) operational since 2016, the Laser Communications Relay Demonstration (LCRD), launched at the end of 2021, Laser Utilizing Communication System (LUCAS), launched in 2020. Semiconductor Inter-satellite Link Experiment (SILEX), Ground/Orbiter Lasercomm Demonstration (GOLD), Optical Inter-orbit Communications Engineering Test Satellite (OICETS), KIrari's Optical Downlink to Oberpfaffenhofen (KIODO), Engineering Test Satellite VI (ETS-VI), ARTEMIS GEO satellite, the High-speed Communication with Advanced Laser Instrument (HICALI) payload. One such example is the OSIRIS4CubeSat (O4C), also called PIXL-1 payload, developed by the German Aerospace Center (DLR), NASA's TBIRD program, The CubeSat Laser Infrared CrosslinK (CLICK) was deployed from the International Space Station (ISS) in July 2022 [44–46].

These difficulties include random variations in beam angle-of-arrival (AOA) brought on by air turbulence, such as scintillation and beam wander, as well as absorption and scattering losses from rain, snow, and fog [44–46]. The design of the FSO link presents extra difficulties, including aiming problems, geometrical losses, and eye safety laws. The FSO link margin can

be increased and geometrical losses can be decreased by using a narrow beam. Advanced laser beam pointing and tracking systems are necessary since it can potentially increase pointing error losses. Introducing mobility will make this effect worse. The radiated optical power is governed by eye safety laws although FSO links do not require a license [44–46].

Mitigation techniques for compensating FSO atmospheric impairments:

1. Hybrid RF/FSO [44–46]: Downlink/uplink RF and FSO communications are influenced by opposing circumstances and exhibit complementing behaviors. Consequently, a hybrid RF/FSO system is an effective way to ensure dependable communication and enhance system availability. One strategy in this case is to employ the RF link as a backup link, with the FSO operating first and the RF activating only in the event of an FSO loss.
2. Aperture averaging [44–46]: By averaging out all random variations over the aperture region, increasing the aperture diameter at the receiver to a size big enough to manage turbulent eddies enhances communication performance and lessens channel fading as compared to a point receiver.
3. Relay-based transmission [44–46]: Research has demonstrated that cooperative transmission outperforms single-hop communication in terms of performance and enhances the signal-to-noise ratio (SNR).
4. Power control [44–46]: To provide a specific degree of communication quality, power is managed by varying the transmit power.
5. Diversity [44–46]: To further increase connection availability and the bit-error-rate (BER) performance of communications, diversity in frequency, time, and space is strongly advised.
6. Error control coding [44–46], commonly known as channel coding, was also taken into consideration as a way to enhance channel dependability in SN downlink transmission. This involves adding redundant bits to the sent data.
7. Modulation [44–46]: A number of modulation techniques can be used to increase spectral efficiency and lessen the negative impacts of turbulence.

2.4 Outline – Structure of the Thesis

In Chapter 2, an introduction to terrestrial 5G, B5G, 6G networks is provided with emphasis on satellite communications and free-space optical communications. In Chapter 3, a methodology for generating received irradiance time series for an optical satellite link is given. Atmospheric turbulence is taken into account for the modeling. Extensive validation of the synthesizer using both first- and second-order statistics is presented. In Chapter 4, a power allocation methodology for a multi-channel optical satellite downlink is proposed. The methodology is based on convex optimization and the water-filling algorithm. A theoretical MIMO optical satellite system in weak turbulence conditions with various scintillation indices is considered. Moreover, the power optimization problem for an optical hybrid network with a satellite source, a ground optical gateway and the user equipment is investigated. In Chapter 5, a power allocation methodology for LEO optical downlinks using HARQ is proposed. In Chapter 6, a robust power allocation strategy for a downlink optical satellite system with pointing jitter is investigated. In Chapter 7, a model-free power allocation methodology for optical satellite systems based on DRL and DNNs is presented. The Thesis concludes with Chapter 8 where the main conclusions are drawn and possible future work is outlined.

Chapter References

[1] ITU. Measuring Digital Development – Facts and Figures 2023. https://www.itu.int/hub/publication/d-ind-ict_mdd-2023-1/.

[2] Wang, C. X., You, X., Gao, X., Zhu, X., Li, Z., Zhang, C., ... & Hanzo, L. (2023). On the road to 6G: Visions, requirements, key technologies and testbeds. *IEEE Communications Surveys & Tutorials*.

[3] Jiang, W., Han, B., Habibi, M. A., & Schotten, H. D. (2021). The road towards 6G: A comprehensive survey. *IEEE Open Journal of the Communications Society*, *2*, 334-366.

[4] Ikram, M., Sultan, K., Lateef, M. F., & Alqadami, A. S. (2022). A road towards 6G communication—A review of 5G antennas, arrays, and wearable devices. *Electronics*, *11*(1), 169.

[5] Bertin, E., Crespi, N., & Magedanz, T. (Eds.). (2021). *Shaping Future 6G Networks: Needs, Impacts, and Technologies*. John Wiley & Sons.

[6] Asghar, M. Z., Memon, S. A., & Hämäläinen, J. (2022). Evolution of wireless communication to 6g: Potential applications and research directions. *Sustainability*, *14*(10), 6356.

[7] Tezergil, B., & Onur, E. (2022). Wireless backhaul in 5G and beyond: Issues, challenges and opportunities. *IEEE Communications Surveys & Tutorials*.

[8] Fontanesi, G., Ortíz, F., Lagunas, E., Baeza, V. M., Vázquez, M. Á., Vásquez-Peralvo, J. A., ... & Chatzinotas, S. (2023). Artificial Intelligence for Satellite Communication and Non-Terrestrial Networks: A Survey. *arXiv preprint arXiv:2304.13008*.

[9] Shehzad, M. K., Rose, L., Butt, M. M., Kovács, I. Z., Assaad, M., & Guizani, M. (2022). Artificial intelligence for 6G networks: Technology advancement and standardization. *IEEE Vehicular Technology Magazine*, *17*(3), 16-25.

[10] Abdelsadek, M. Y., Chaudhry, A. U., Darwish, T., Erdogan, E., Karabulut-Kurt, G., Madoery, P. G., ... & Yanikomeroglu, H. (2022). Future space networks: Toward the next giant leap for humankind. *IEEE Transactions on Communications*, *71*(2), 949-1007.

[11] O'shea, T., & Hoydis, J. (2017). An introduction to deep learning for the physical layer. *IEEE Transactions on Cognitive Communications and Networking*, *3*(4), 563-575.

[12] Azari, M. M., Solanki, S., Chatzinotas, S., Kodheli, O., Sallouha, H., Colpaert, A., ... & Ottersten, B. (2022). Evolution of non-terrestrial networks from 5G to 6G: A survey. *IEEE communications surveys & tutorials*.

[13] Al-Hraishawi, H., Chougrani, H., Kisseleff, S., Lagunas, E., & Chatzinotas, S. (2022). A survey on non-geostationary satellite systems: The communication perspective. *IEEE Communications Surveys & Tutorials*.

[14] Rinaldi, F., Maattanen, H. L., Torsner, J., Pizzi, S., Andreev, S., Iera, A., ... & Araniti, G. (2020). Non-terrestrial networks in 5G & beyond: A survey. *IEEE access*, *8*, 165178-165200.

[15] Araniti, G., Iera, A., Pizzi, S., & Rinaldi, F. (2021). Toward 6G non-terrestrial networks. *IEEE Network*, *36*(1), 113-120.

[16] Giordani, M., & Zorzi, M. (2020). Non-terrestrial networks in the 6G era: Challenges and opportunities. *IEEE Network*, *35*(2), 244-251.

[17] Kim, J., Lee, J., Ko, H., Kim, T., & Pack, S. (2022). Space mobile networks: Satellite as core and access networks for B5G. *IEEE Communications Magazine*, *60*(4), 58-64.

[18] Xing, R., Ma, X., Zhou, A., Dustdar, S., & Wang, S. (2023). From earth to space: A first deployment of 5G core network on satellite. *China Communications*, *20*(4), 315-325.

[19] De Gaudenzi, R., Luise, M., & Sanguinetti, L. (2022). The open challenge of integrating satellites into (beyond-) 5G cellular networks. *IEEE Network*, *36*(2), 168-174.

[20] Sun, Y., Peng, M., Zhang, S., Lin, G., & Zhang, P. (2022). Integrated satellite-terrestrial networks: architectures, key techniques, and experimental progress. *IEEE Network*, *36*(6), 191-198.
[21] Abdelsalam, N., Al-Kuwari, S., & Erbad, A. (2023). Physical Layer Security in Satellite Communication: State-of-the-art and Open Problems. *arXiv preprint arXiv:2301.03672*.
[22] Furqan, M., & Goswami, B. (2022). Satellite communication networks. *Handbook of Real-Time Computing; Tian, Y.-C., Levy, DC, Eds*, 1-22.
[23] A. D. Panagopoulos, P.-D. M. Arapoglou, P. G. Cottis, "Satellite Communications at Ku, Ka and V Bands: Propagation Impairments and Mitigation Techniques", IEEE Communication Surveys and Tutorials, 2004.
[24] C. N. Efrem and A. D. Panagopoulos, "Dynamic Energy-Efficient Power Allocation in Multibeam Satellite Systems", IEEE Wirel. Comm. Letters, vol. 9, no. 2, pp. 228 231, Feb. 2020.
[25] A. Destounis, and A. D. Panagopoulos, "Dynamic Power Allocation for Broadband Multi-Beam Satellite Communication Networks," IEEE Commun. Lett., vol. 15, no. 4, pp. 380 382, April 2011.
[26] Roumeliotis, A. J., Kourogiorgas, C. I., & Panagopoulos, A. D. (2018). Optimal dynamic capacity allocation for high throughput satellite communications systems. *IEEE Wireless Communications Letters*, *8*(2), 596-599.
[27] Papafragkakis, A. Z., Kouroriorgas, C. I., & Panagopoulos, A. D. (2021). Performance of Micro-Scale Transmission & Reception Diversity Schemes in High Throughput Satellite Communication Networks. *Electronics*, *10*(17), 2073.
[28] Darwish, T., Kurt, G. K., Yanikomeroglu, H., Bellemare, M., & Lamontagne, G. (2022). LEO satellites in 5G and beyond networks: A review from a standardization perspective. *IEEE Access*, *10*, 35040-35060.
[29] Chen, S., Sun, S., & Kang, S. (2020). System integration of terrestrial mobile communication and satellite communication—the trends, challenges and key technologies in B5G and 6G. *China communications*, *17*(12), 156-171.
[30] Peng, D., He, D., Li, Y., & Wang, Z. (2022). Integrating terrestrial and satellite multibeam systems toward 6G: Techniques and challenges for interference mitigation. *IEEE Wireless Communications*, *29*(1), 24-31.
[31] Heo, J., Sung, S., Lee, H., Hwang, I., & Hong, D. (2023). Mimo satellite communication systems: A survey from the phy layer perspective. *IEEE Communications Surveys & Tutorials*.
[32] Fang, X., Feng, W., Wei, T., Chen, Y., Ge, N., & Wang, C. X. (2021). 5G embraces satellites for 6G ubiquitous IoT: Basic models for integrated satellite terrestrial networks. *IEEE Internet of Things Journal*, *8*(18), 14399-14417.
[33] Jiang, B., Yan, Y., You, L., Wang, J., Wang, W., & Gao, X. (2022). Robust secure transmission for satellite communications. *IEEE Transactions on Aerospace and Electronic Systems*.
[34] Jiang, W. (2023). Software defined satellite networks: A survey. *Digital Communications and Networks*.
[35] Kodheli, O., Lagunas, E., Maturo, N., Sharma, S. K., Shankar, B., Montoya, J. F. M., ... & Goussetis, G. (2020). Satellite communications in the new space era: A survey and future challenges. *IEEE Communications Surveys & Tutorials*, *23*(1), 70-109.
[36] Guidotti, A., Vanelli-Coralli, A., Conti, M., Andrenacci, S., Chatzinotas, S., Maturo, N., ... & Cioni, S. (2019). Architectures and key technical challenges for 5G systems incorporating satellites. *IEEE Transactions on Vehicular Technology*, *68*(3), 2624-2639.
[37] Khammassi, M., Kammoun, A., & Alouini, M. S. (2023). Precoding for high throughput satellite communication systems: A survey. *IEEE Communications Surveys & Tutorials*.

[38] Völk, F., Liolis, K., Corici, M., Cahill, J., Schwarz, R. T., Schlichter, T., ... & Knopp, A. (2019). Satellite integration into 5G: Accent on first over-the-air tests of an edge node concept with integrated satellite backhaul. *Future Internet*, *11*(9), 193.
[39] Deutschmann, J., Hielscher, K. S., & German, R. (2022). Next-Generation Satellite Communication Networks.
[40] Al Homssi, B., Al-Hourani, A., Wang, K., Conder, P., Kandeepan, S., Choi, J., ... & Moores, B. (2022). Next generation mega satellite networks for access equality: Opportunities, challenges, and performance. *IEEE Communications Magazine*, *60*(4), 18-24.
[41] Sharma, S. K., Chatzinotas, S., & Arapoglou, P. D. (2018). *Satellite communications in the 5G era*. Institution of Engineering and Technology.
[42] Liolis, K., Geurtz, A., Sperber, R., Schulz, D., Watts, S., Poziopoulou, G., ... & Chuberre, N. (2019). Use cases and scenarios of 5G integrated satellite-terrestrial networks for enhanced mobile broadband: The SaT5G approach. *International Journal of Satellite Communications and Networking*, *37*(2), 91-112.
[43] Kolev, D. R., Carrasco-Casado, A., Trinh, P. V., Shiratama, K., Ishola, F., Kotake, H., ... & Toyoshima, M. (2023). Latest Developments in the Field of Optical Communications for Small Satellites and Beyond. *Journal of Lightwave Technology*.
[44] Hemmati, H. (Ed.). (2020). *Near-earth laser communications* (Vol. 1). CRC press.
[45] L. Andrews, R. Phillips, "Laser Beam Propagation through Random Media" SPIE Press, 2005.
[46] Kaushal, H., & Kaddoum, G. (2016). Optical communication in space: Challenges and mitigation techniques. *IEEE communications surveys & tutorials*, *19*(1), 57-96.
[47] Bekkali, A., Hattori, M., Hara, Y., & Suga, Y. (2023). Free Space Optical Communication Systems FOR 6G: A Modular Transceiver Design. *IEEE Wireless Communications*, *30*(5), 50-57.
[48] Samy, R., Yang, H. C., Rakia, T., & Alouini, M. S. (2022). Space-air-ground FSO networks for high-throughput satellite communications. *IEEE Communications Magazine*, *60*(12), 82-87.
[49] Lyras, N. K., Efrem, C. N., Kourogiorgas, C. I., Panagopoulos, A. D., & Arapoglou, P. D. (2019). Optimizing the ground network of optical MEO satellite communication systems. *IEEE Systems Journal*, *14*(3), 3968-3976.
[50] Chaudhry, A. U., & Yanikomeroglu, H. (2020). Free space optics for next-generation satellite networks. *IEEE Consumer Electronics Magazine*, *10*(6), 21-31.
[51] Marbel, R., Yozevitch, R., Grinshpoun, T., & Ben-Moshe, B. (2022). Dynamic network formation for fso satellite communication. *Applied Sciences*, *12*(2), 738.
[52] Alqaraghuli, A. J., Siles, J. V., & Jornet, J. M. (2023). The Road to High Data Rates in Space: Terahertz vs. Optical Wireless Communication. *IEEE Aerospace and Electronic Systems Magazine*.
[53] Majumdar, A. K. (2022). *Laser Communication with Constellation Satellites, UAVs, HAPs and Balloons*. Springer International Publishing.
[54] Celik, A., Romdhane, I., Kaddoum, G., & Eltawil, A. M. (2022). A top-down survey on optical wireless communications for the internet of things. *IEEE Communications Surveys & Tutorials*.
[55] Ahmad, I., Nguyen, K. D., Letzepis, N., & Lechner, G. (2020). On the next-generation high throughput satellite systems with optical feeder links. *IEEE Systems Journal*, *15*(2), 2000-2011.
[56] Wei, Z., Wang, Z., Zhang, J., Li, Q., Zhang, J., & Fu, H. Y. (2022). Evolution of optical wireless communication for B5G/6G. *Progress in Quantum Electronics*, *83*, 100398.

[57] Vu, M. Q., Le, H. D., Pham, T. V., & Pham, A. T. (2023). Design of Satellite-Based FSO/QKD Systems using GEO/LEOs for Multiple Wireless Users. *IEEE Photonics Journal*.
[58] Ntanos, Argiris, et al. "Leo satellites constellation-to-ground QKD links: Greek quantum communication infrastructure paradigm." *Photonics*. Vol. 8. No. 12. MDPI, 2021.
[59] Wenning, M., Autenrieth, A., Elbers, J. P., & Mas-Machuca, C. (2023, April). Availability and Throughput Evaluation of Optical Based High Throughput Satellite Networks. In *2023 19th International Conference on the Design of Reliable Communication Networks (DRCN)* (pp. 1-8). IEEE.
[60] Chaaban, A., Rezki, Z., & Alouini, M. S. (2021). On the capacity of intensity-modulation direct-detection Gaussian optical wireless communication channels: A tutorial. *IEEE Communications Surveys & Tutorials*, *24*(1), 455-491.

Chapter 3
Time Series Irradiance Synthesizer for Optical GEO Downlinks: Validation with ARTEMIS Experimental Measurements[1,2]

Next-generation 5G networks generate a need for broadband, low latency, and power-efficient backhauling and data-relay services. In this Chapter, optical satellite communications links, as an integrated component of 5G networks, are studied. A methodology for the generation of received irradiance/power time series for a GEO downlink concentrated on small aperture receiver terminals is reported. The synthesizer takes into account the atmospheric phenomena that degrade the propagation of the optical signal especially the turbulence effects. For modelling the scintillation effects, the Kolmogorov spectrum is assumed, and Rytov's approximation under weak turbulence is also used. The time series are generated using the theory of stochastic differential equations. Finally, the proposed synthesizer is compared in terms of first and second-order statistics with experimental data from the European Space Agency's ARTEMIS GEO optical satellite link campaign with very good agreement. Finally, simulated received power statistics for various weather conditions are presented using the proposed validated methodology. Some important conclusions are drawn.

3.1 Introduction

Next-generation networks such as Long-Term Evolution (LTE) Advanced Pro, and 5G are expected to have rigorous specifications concerning connectivity so that every user globally can connect to high-bandwidth mobile internet for accessing a variety of services. Satellite communications are planned to provide edge delivery services, effectively establishing fixed

5G backhaul links between terrestrial nodes to infrastructures and optimizing the backhaul links for high mobility means of transport [1–4].

During the last years, laser communication system technology has become increasingly mature making it an attractive opportunity for space communication systems. Optical communication systems demonstrate important advantages compared with the already existing Radio Frequency (RF) satellite communication systems, like [5–6] a) reduced mass, power, and volume of needed equipment, b) hundreds of times more spectral bandwidth and higher data rates can be accomplished c) there is improved security and no interception due to the highly directive antennas d) up to now there is no need of frequency regulation. Therefore, many experimental missions are being conducted for the investigation of the performance of optical satellite communication systems. Experimental missions have been demonstrated for inter-satellite links, for the bi-directional ground to GEO and ground to LEO among others [5–6].

Unguided light beam propagation suffers from numerous adverse atmospheric phenomena and most importantly the occurrence of fog and clouds [2],[5–6]. While rain is the dominant attenuation factor for an mmWave link inducing losses up to 50 dB/km for a 150 mm/h rain rate [2], in the case of an optical link fog losses can reach even 350dB/km due to the comparable fog droplet size to the optical wavelength [5]. Moreover, dense clouds and mostly cirrus clouds may completely block Line of Sight (LOS) communication [7–10]. Therefore, mitigation techniques are employed, such as hybrid Free Space Optics/Radio Frequency (FSO/RF) systems, site diversity through an interconnection of optical ground stations (OGSs), or wavelength diversity [7–10].

Atmospheric turbulence comes from the variations in wind speed, pressure, and temperature which result in variations in the refractive index [1–2]. Therefore, the strength of turbulence effects depends on the time of the day, the slant path, i.e., the elevation angle of the link, and the altitude of the station among others. Turbulence is more severe during the day, in lower elevation angles (longer propagation path) and for low altitude stations (denser atmosphere) [1–2]. Many theoretical models are used to accurately analyze the downlink scintillation effects, but the most common are the log-normal distribution for weak turbulence conditions, gamma-gamma distribution for strong turbulence, and double-Weibull for moderate to strong intensity [1,5,6,12].

This Chapter is concentrated on the downlink propagation case. In downlink, atmospheric turbulence is closer to the receiver and these turbulence effects are exhibited as small-scale fluctuations of the received irradiance known as scintillation and as beam effects, such as

beam spreading and beam wander. Scintillation is the primary signal degradation factor in the downlink case while the beam aberrations are considered negligible. Physical layer methods like aperture averaging and adaptive optics are among the most applied techniques for mitigating scintillation. All in all, the optical system suffers from pointing and tracking errors caused by weak earthquakes, equipment vibrations, and optical misalignments [1,5,6].

The aperture averaging effect is higher with the larger aperture diameters. However, for small apertures, the scintillation effects are present and degrade the performance of the optical signal. Since the cost of a large receiving aperture may be forbidden for a great variety of possible optical satellite applications for the reliable design of an optical GEO downlink, the accurate prediction of scintillation for small apertures is required. In Figure 3-1 the downlink irradiance cumulative distribution functions (CDFs) for two different apertures Figure 3-1(a) 1 m diameter (ESA's Terminal), and Figure 3-1(b) 0.26 m diameter (LUCE Terminal), are presented [13–14]. For the estimation of these curves' experimental measurements, (time series) from the ARTEMIS optical campaign are used. More information about the ARTEMIS campaign is reported in Section 3.2. It can be easily pinpointed that in the case of a 1 m receiver, the effects of turbulence are minimized. However, in the case of a 0.26 m receiver, for probabilities of interest, losses of more than 4–5 dBs may be caused.

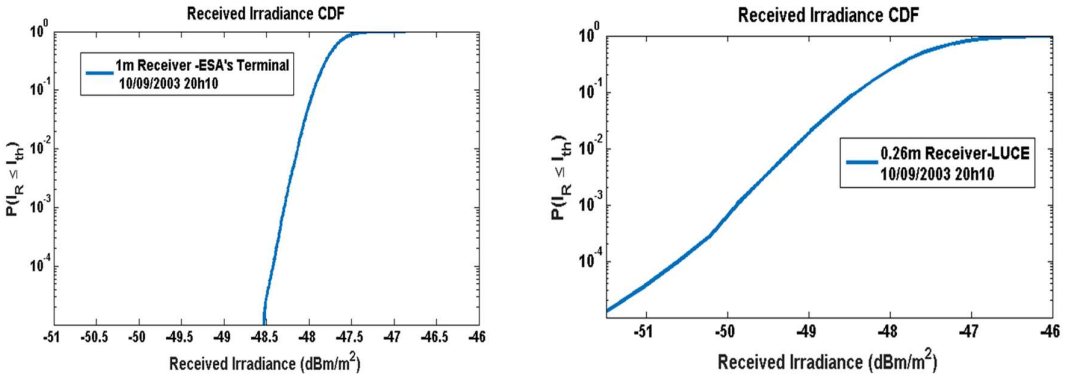

(a) (b)

Figure 3-1: Downlink Received Irradiance CDF (a) 1 m aperture (b) 0.26 m aperture.

In this Chapter, a synthesizer for the generation of received irradiance/power time series taking into account the turbulence effects among others for an optical GEO downlink is proposed. The synthesizer is benefited from the use of stochastic differential equations for the incorporation of scintillation effects. The synthesizer is validated in terms of first and second-order statistics with actual experimental data from the ARTEMIS campaign [13–14]. The main assumptions of the methodology are summarized:

i. Downlink Propagation

ii. GEO satellite-to-ground optical link

iii. Rytov's theory is considered and Kolmogorov's spatial spectrum of refractive index is applied

iv. Optical links with elevation angle greater than 20 deg are assumed

v. A single collimated Gaussian beam is transmitted

vi. Perfect link pointing and tracking

The remainder of the Chapter is structured as follows: in Section 3.2 a brief summary of ARTEMIS optical satellite experimental campaign is presented; in Section 3.3 the required theoretical background is reported including important metrics regarding the downlink's turbulence effects and followed by the proposed methodology for the generation of received irradiance time series; in Section 3.4 numerical results using the synthesized data are validated with experimental results derived from ARTEMIS campaign and simulated received power statistics for various weather conditions are reported using the validated methodology; and finally Section 3.5 concludes this Chapter.

3.2 Recap of ARTEMIS Optical Campaign

In 2003 European Space Agency (ESA) established bi-directional optical links between the ESA's ground station in Tenerife Spain at an altitude of 2.4 km over the sea favorable for optical satellite communications and the ARTEMIS GEO satellite (launched in 2001) at 21.5 deg East for the study and characterization of laser beam propagation through atmospheric turbulence [13]. Additionally, the Japanese Aerospace Exploration Agency (JAXA) developed the LUCE optical terminal and set it up at ESA's OGS in Tenerife, where bi-directional sessions were established. Therefore, measurements are used as receivers for both the ESA's 1 m terminal [13] and the 0.26 m LUCE receiver [14]. The elevation angle of the link was 37 deg. For downlink transmission, the wavelength used is 819 nm and the laser diameter is 125 mm [13]. The ARTEMIS location and technical features are reported in Table 3-1 and Table 3-2 accordingly.

Table 3-1: ARTEMIS location parameters

Longitude	**Latitude**	**Altitude**	**Elevation Angle**
21.5° East	0.0° ± 2.81° North	35,787 km	37°

Table 3-2: ARTEMIS technical features

Wavelength	**Beam Diameter ($1/e^2$)**	**Transmitted Power**
819 nm	125 mm	10 mW

In this Chapter, we concentrate on the LUCE terminal which has a shorter receiver. In Figure 3-2(a) the configuration of the experiment is exhibited while in Figure 3-2(b) a snapshot of concurrent irradiance measurements for both LUCE and ESA's terminal is reported. The aperture averaging effect is higher in ESA's terminal which is equipped with a larger receiver and as a result, the measurements appear with smaller fluctuations. Additionally, per the experimental measurements, concurrent meteorological recordings were available.

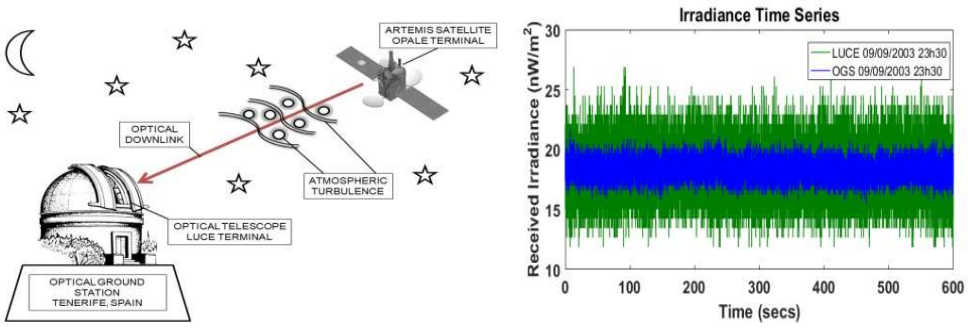

(a) (b)

Figure 3-2: (a) ARTEMIS campaign configuration (b) concurrent irradiance time series.

3.3 Proposed Synthesizer

In this section, the proposed synthesizer is reported. To begin with, for a downlink optical GEO satellite communication system the received irradiance time series can be given according to the next formula:

$$I_{\mathrm{R}}\left(r,L,t\right)=L_T\cdot L_R\cdot L_{atm}\cdot I\left(r,L,t\right) \tag{3.1}$$

where $L\left(m\right)$ is the link distance (slant path), t is the time(s), and r is the radial distance from the beam centre. L_T , L_R are efficiencies of the transmitter and receiver respectively. In L_{atm} the atmospheric transmittance and cirrus clouds transmittance are incorporated. In $I\left(W/m^2\right)$ the transmitter gain, free space losses, and turbulence effects are incorporated. From (3.1) received power in Watts can be given as $P_R=I_R*\pi D_R^2/4$, where D_R is the receiver's aperture diameter.

Firstly, *I* will be expressed in the case of no turbulence without the time dependence [6,11]:

$$I(r,L)=\frac{2}{\pi}\cdot\frac{P_T}{W^2(L)}\cdot e^{-\frac{2r^2}{W^2(L)}} \tag{3.2}$$

Where $P_T(W)$ is the transmitted power and $W(L)$ is the beam waist in meters after propagation of distance *L* given according to the next formula [6,11]:

$$W^2(L)=W_0^2\left[1+\left(\frac{\lambda L}{\pi W_0^2}\right)^2\right] \tag{3.3}$$

where $W_0(m)$ is the beam radius of the source at which the irradiance falls to $1/e^2$ (spot size). In order to incorporate in *I* the turbulence effects the structure constant of refractive index $C_n^2(h)$ for the whole slant path is required. Therefore, a modified version of Hufnagel–Valley Model (H-V) where the altitude above the sea level (*h*) and the ground station's altitude $H_{GS}(m)$ are incorporated is employed [5–6].

$$C_n^2(h)=A_0\exp\left(-\frac{H_{GS}}{700}\right)\exp\left((H_{GS}-h)/100\right)+5.94\times10^{-53}\times\left(\frac{u_{rms}}{27}\right)^2 h^{10}\exp\left(-\frac{h}{1000}\right)+2.7\times10^{-16}\exp\left(-\frac{h}{1500}\right) \tag{3.4}$$

where $A_0\left(m^{-2/3}\right)$ is the refractive index structure parameter at ground level and $u_{rms}(m/s)$ is the rms wind speed on slant path:

$$u_{rms}=\sqrt{\frac{1}{15\times10^3}\int_{5\times10^3}^{20\times10^3}V^2(h)dh} \tag{3.5}$$

Where $V(h)$ can be estimated using the Bufton wind model [11]:

$$V(h)=w_s h+V_g+30\exp\left[-\left(\frac{h-9400}{4800}\right)^2\right] \tag{3.6}$$

$w_s(rad/\mathrm{s})$ is the slew rate expressing the relative motion between the satellite and the ground station and $V_g(m/s)$ is the wind speed on ground. It must be pinpointed that turbulence is negligible for altitudes higher than 20 km [11] i.e. assuming $H_{turb}=20000\,m$, $C_n^{\,2}(h>H_{turb})=0$.

Now for downlink propagation where turbulence causes only scintillation effects (no beam wandering) and assuming there is perfect tracking of beam centre then assuming the

Rytov theory and the Kolmogorov spectrum expression (3.2) is modified in order the turbulence effects are incorporated as follows [6,11]:

$$I\left(L,t\right)=\frac{2}{\pi}\cdot\frac{P_T}{W^2{}_{LT}\left(L\right)}\cdot e^{2X_v} \tag{3.7}$$

$W_{LT}\left(L\right)$ is the effective beam spot size after propagation distance L considering the scintillation effects. However, since in downlink propagation the beam spreading due to scintillation is negligible it is assumed that $W_{LT}\left(L\right)=W\left(L\right)$.

Before we continue with the other terms firstly the scintillation index (SI) is exhibited. Scintillation index is the normalized variance of the received irradiance $\sigma_I^2=\frac{\left\langle I^2\right\rangle}{\left\langle I\right\rangle^2}-1$ where I is the irradiance. In this analysis only the weak turbulence (i.e. SI<1) is investigated. In expression (3.8) the theoretical expression for the estimation of scintillation index for a point receiver [11] based on plane wave approximation is exhibited while for the incorporation of aperture averaging effect, aperture averaging factor $\left(A\left(D_R\right)=\sigma_{\mathrm{I}}^2/\sigma_{\mathrm{I},po\mathrm{int}}^2\right)$ is used and SI is estimated as $\sigma_{\mathrm{I}}^2=A\left(D_R\right)\sigma_{\mathrm{I},po\mathrm{int}}^2$. Aperture averaging factor $A\left(D_R\right)$ can be theoretically estimated depending on the diameter of the aperture of the receiver using expression (3.9) as derived from [15]. In case that experimental data are available aperture averaging factor can be estimated directly from the data as $A\left(D_R\right)=\frac{\left\langle\sigma_{I,data}^2\right\rangle}{\left\langle\sigma_{I,po\mathrm{int}}^2\right\rangle}$ where $\sigma_{I,data}^2$ is the scintillation computed from the data.

$$\sigma_{point}^2=2.25k^{\frac{7}{6}}sec^{\frac{11}{6}}\left(\zeta\right)\int_{H_{GS}}^{H_{GS}+H_{turb}}C_n^2\left(h\right)\left(h-h_0\right)^{\frac{5}{6}}dh \tag{3.8}$$

where $k=2\pi/\lambda\left(rad/m\right)$ is the wavenumber, $\lambda\left(m\right)$ is the wavelength, ζ is the azimuth angle.

$$A\left(D\right)=\left[1+1.1\left(\frac{D_R{}^2}{\lambda h_s\cos\left(\zeta\right)}\right)^{\frac{7}{6}}\right]^{-1},\ where\ h_s=\left[\frac{\int_{H_{GS}}^{H_{GS}+H_{turb}}C_n^2\left(h\right)\left(h-H_{GS}\right)^2dh}{\int_{H_{GS}}^{H_{GS}+H_{turb}}C_n^2\left(h\right)\left(h-H_{GS}\right)^{5/6}dh}\right]^{6/7} \tag{3.9}$$

Additionally for weak turbulence the log amplitude variance is defined as $\sigma_\chi^2=\ln\left(\sigma_I^2+1\right)/4$.

Another fundamental metric for the full description of the optical turbulent channel is the Fried parameter $r_0(m)$ [5,6,11]:

$$r_0 = \left[0.42 \sec(\zeta) k^2 \int_{H_{GS}}^{H_{Turb}} C_n^2(h) dh \right]^{-3/5} \tag{3.10}$$

The fried parameter constitutes the atmospheric coherence length and describes the quality of the propagating optical wave front. The larger r_0 is the smaller the turbulence effects [5,6,11].

Finally, in $\exp(2X_v)$ the scintillation effects are incorporated. X_v is the normalized log-amplitude. For weak turbulence the normalized log amplitude can be considered as a zero mean-unity variance low pass Gaussian process with -80/3 dB/decade slope. Assuming weak turbulence conditions the log-amplitude is a normally distributed Gaussian process with $-\sigma_\chi^2$ mean value, σ_χ^2 variance [16] and low pass PSD with -80/3 dB/decade slope. In Figure 3-3 the PSD of downlink irradiance as received by LUCE is displayed along with the graph of the function $(cf)^{-\frac{8}{3}}$ where c is a constant. In log-log scale the latter function is a straight line with -8/3 slope and verifies that the spectra of downlink scintillation decrease with -80/3 dB/decade.

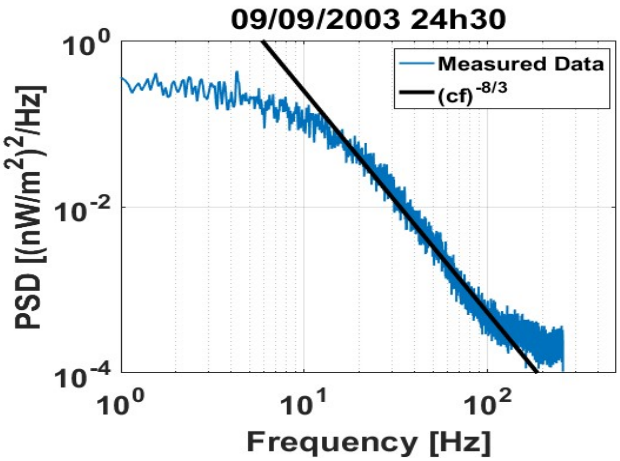

Figure 3-3: The power spectral density (PSD) of scintillation decreases with -80/3 dB/decade.

Stochastic differential equations (SDEs) driven by fractional Brownian motion are used to reproduce such processes as reported in [17]. The requested Gaussian process is the solution of the following SDE [17]:

$$dX_{t,1} = -\lambda_s X_{t,1} dt + \sigma dB_H \tag{3.11}$$

where $X_{t,1}$ is given by:

$$X_{t,1}(t) = e^{-\lambda_s t}\sigma\int_0^t e^{\lambda_s u} dB_u^H \tag{3.12}$$

The λ_s and σ depend on the dynamic parameters of the stochastic process and its long-term statistics, respectively [17]. $(0 < H < 1)$ is the Hurst exponent [17]. The log-amplitude time series $\mathrm{X}_s(t)$ can now be expressed as:

$$X_s(t) = -\sigma_\chi^2 + \sigma_\chi X_{t,1}(t) \tag{3.13}$$

where

$$\sigma_\chi^2 = \frac{1}{4}\ln(\sigma_I^2 + 1) \tag{3.14}$$

3.4 Validation

In this section, the accuracy, performance and capability of the proposed synthesizer to reproduce the received irradiance statistics will be evaluated. Therefore, good agreement in terms of first and second order irradiance statistics between the numerical and the experimental results is necessary. The validation procedure is the following:

i. Computation of the first order statistics, that is, normalized probability density function (PDF), cumulative distribution function (CDF) of the available data from ARTEMIS optical experiments. For every session the SI is also calculated.

ii. Computation of the second order statistics, that is, power spectral density (PSD) of the available experimental data.

iii. Generation of received irradiance time-series using the proposed methodology. The model inputs are the ARTEMIS coordinates and transmitting settings given by Tables 3-1 and 3-2, the refractive index structure parameter at ground level A_0 which was kept fixed at a value of $10^{-15}\left(m^{-2/3}\right)$ due to the fact that the sessions took place at night, the session's ground wind speed V_g which was provided by the nearby installed weather station and the aperture averaging factor $A(D_r)$ where D_r is the LUCE's diameter. The $A(D_r)$ is estimated close to 0.1 using (3.9).

iv. Computation of normalized PDF, CDF and PSD of the synthesized data and the corresponding SIs.

v. Comparison of the derived numerical results with the respective experimental results and examination of possible discrepancies.

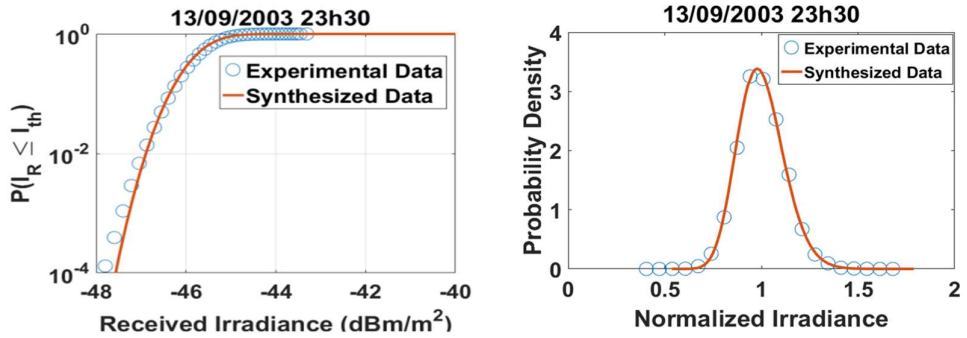

(a) (b)

Figure 3-4: First order statistics validation for session on 13/09/2003 23:30 (a) experimental CDF vs synthesized CDF (b) experimental normalized PDF vs synthesized normalized PDF.

To begin with, the first session is reported is on 13/09/2003 23:30. The wind speed on ground taken from the meteorological data was 0.29 m/s. The SI computed from the methodology is 0.0142 which is very close to the one computed from the experimental data which is 0.0140. In Figure 3-4 the synthesizer is tested in terms of first order statistics (a): CDF and (b): normalized PDF for this session.

The second session is on 16/09/2003 21:10. The wind speed on ground taken from the meteorological data was 2.8 m/s. The SI computed from the methodology is 0.0170 which is very close to the one computed from the experimental data which is 0.0164. In Figure 3-5 the synthesizer is tested in terms of first order statistics (a): CDF and (b): normalized PDF.

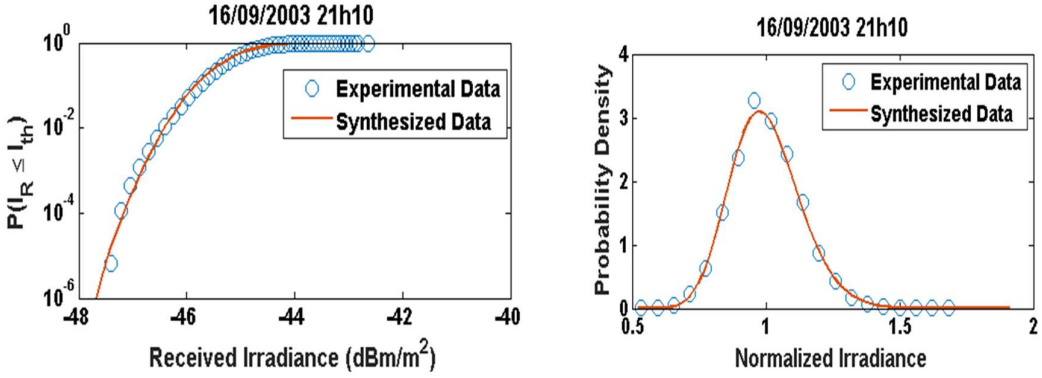

(a) (b)

Figure 3-5: First order statistics validation for session on 16/09/2003 21:10 (a) experimental CDF vs synthesized CDF (b) experimental normalized PDF vs synthesized normalized PDF.

From Figures 3-4, 3-5 it can be observed that the proposed synthesizer can reproduce the first order statistics of received irradiance for a GEO optical downlink with very good accuracy.

The next session examined took place on 13/09/2003 during 23:30–23:50. In Table 3-3 the recorded ground wind speed, the derived SI from the synthesized data and the measured SI are given. In Figure 3-6 the numerical first order statistics, that is, normalized PDF and CDF for this session are presented and compared to the experimental results. In Figure 3-7 the second order statistics (PSD) are shown and tested against the experimental results.

Table 3-3: Methodology Scintillation Index vs. Experimental Scintillation Index

Session Date	Wind speed on ground (m/s)	Methodology scintillation index	Measured scintillation index
13/09/2003 23h30	0.3	0.0142	0.0140
16/09/2003 21h10	2.8	0.0170	0.0164
10/09/2003 20h10	4.3	0.0190	0.0183

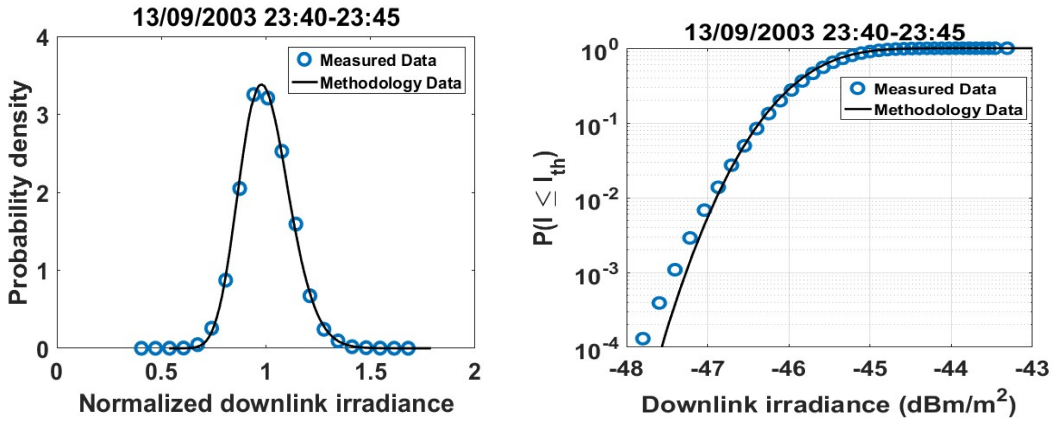

(a) (b)

Figure 3-6: First order irradiance statistics validation for session on 13/09/2003 23:30. (a) Normalized probability density function (PDF) of measured data vs. Normalized PDF of generated data; (b) cumulative distribution function (CDF) of measured data vs. CDF of generated data.

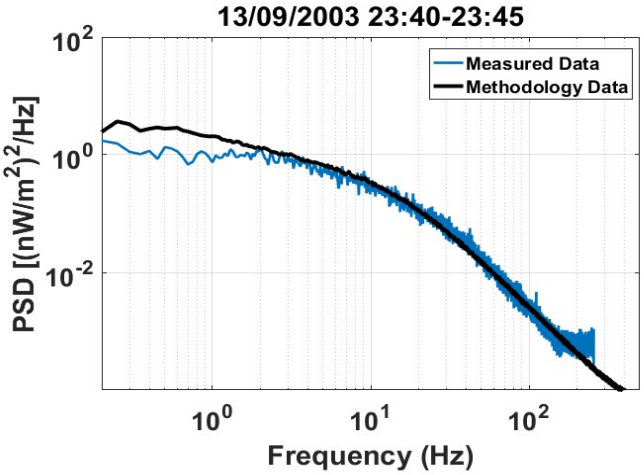

Figure 3-7: Second order irradiance statistics validation for session on 13/09/2003 23:30. PSD of measured data vs. PSD of generated data.

The next experimental session took place on 16/09/2003 during 21:10—21:30. In Table 3-3 the recorded ground wind speed, the derived SI from the synthesized data and the measured SI is given. In Figure 3-8 the numerical first order statistics, that is, normalized PDF and CDF for this session are presented and compared to the experimental results. In Figure 3-9 the second order statistics, that is, PSD are shown and tested against the experimental results.

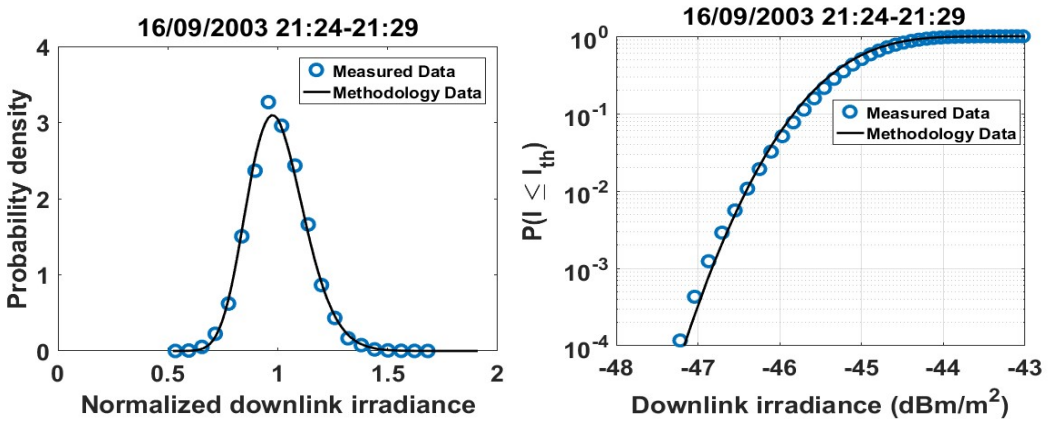

(a) (b)

Figure 3-8: First order irradiance statistics validation for session on 16/09/2003 21:10. (a) Normalized PDF of measured data vs. Normalized PDF of generated data; (b) CDF of measured data vs. CDF of generated data.

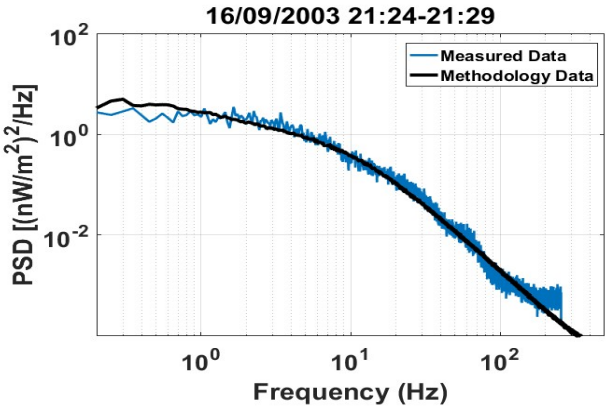

Figure 3-9: Second order irradiance statistics validation for session on 16/09/2003 21:10. PSD of measured data vs. PSD of generated data.

The following experimental session took place on 10/09/2003 during 20:10–20:30. In Table 3-3 the recorded ground wind speed, the derived SI from the synthesized data and the measured SI is given. In Figure 3-10 the numerical first order statistics, that is, normalized PDF and CDF for this session are presented and compared to the experimental results. In Figure 3-11 the numerical second order statistics, that is, PSD are shown and tested against the experimental results.

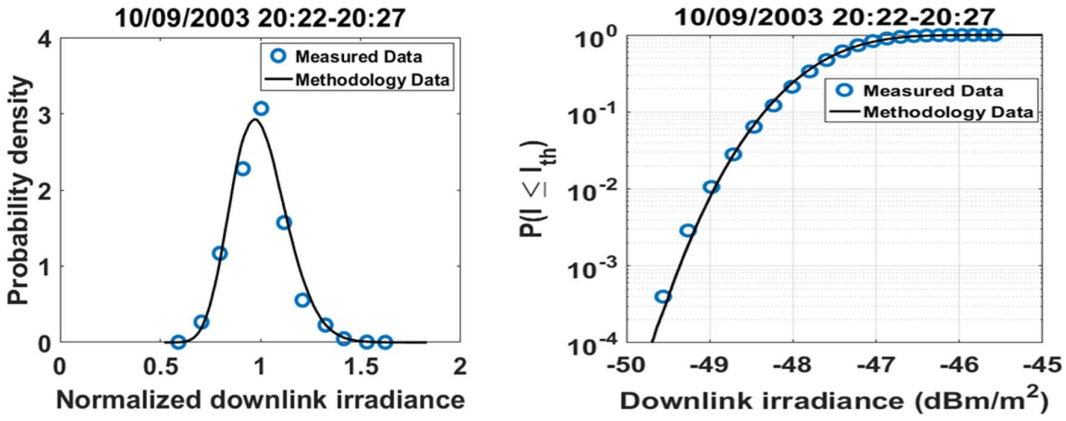

(a) (b)

Figure 3-10: First order irradiance statistics validation for session on 10/09/2003 20:10. (a) Normalized PDF of measured data vs. Normalized PDF of generated data; (b) CDF of measured data vs. CDF of generated data.

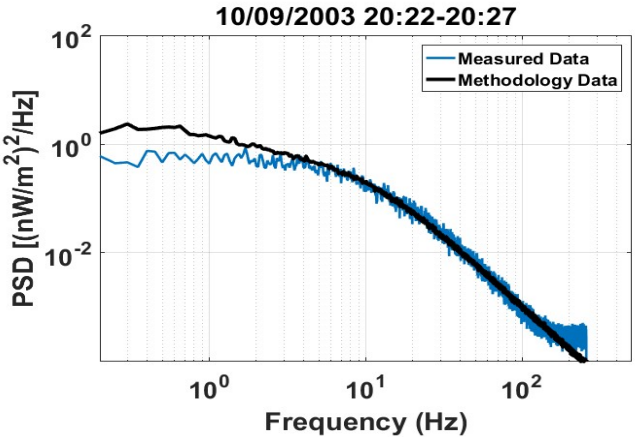

Figure 3-11: Second order irradiance statistics validation for session on 10/09/2003 20:10. PSD of measured data vs. PSD of generated data.

It was observed that the long-term irradiance statistics are re-produced by the proposed synthesizer and fully represent the experimental ones. Concerning the first order statistics results, the scintillation indexes computed from the time-series generated are very similar to the measured ones as well as the corresponding normalized PDFs and CDFs which almost coincide. It is clear that the various wind speeds on the vertical (to the slant path) path cause different turbulence conditions and the larger the wind speed, the greater the SI value. Regarding the second order statistics results, the methodology-obtained PSDs show good agreement with the ones computed from the optical experimental data. Moreover, it can be seen that the scintillation effect is dominant in the frequency range under 10 Hz with a 3dB bandwidth between 6 Hz and 8 Hz. From 10 Hz and after the power spectrum decreases steadily until the 100 Hz where the noise power spectra becomes significant.

In this section the long-term received power statistics, the first order statistics, are presented using the validated synthesizer. The simulation of the turbulent optical channel is performed under various weather conditions in terms of different $C_n^2(h)$ values, that is, different V_g, A_0 leading to various Fried parameters and scintillation index values. The model hypothetical inputs are given below:

Communication wavelength is λ=1040 nm; transmitting power is $P_T = 5$ W ; transmitter's efficiency is $\eta_T = 0.7$; receiver's efficiency is $\eta_R = 0.3$ including the quantum efficiency; the atmospheric transmittance is $\eta_{Atm} = 0.8$; receiver's aperture diameter is $D_r = 260$ mm ; beam diameter is $2W_0 = 125$ mm ; ground station's height is $H_{GS} = 1500$ m with elevation angle 37°. In Figure 3-12 the simulated CDFs are demonstrated.

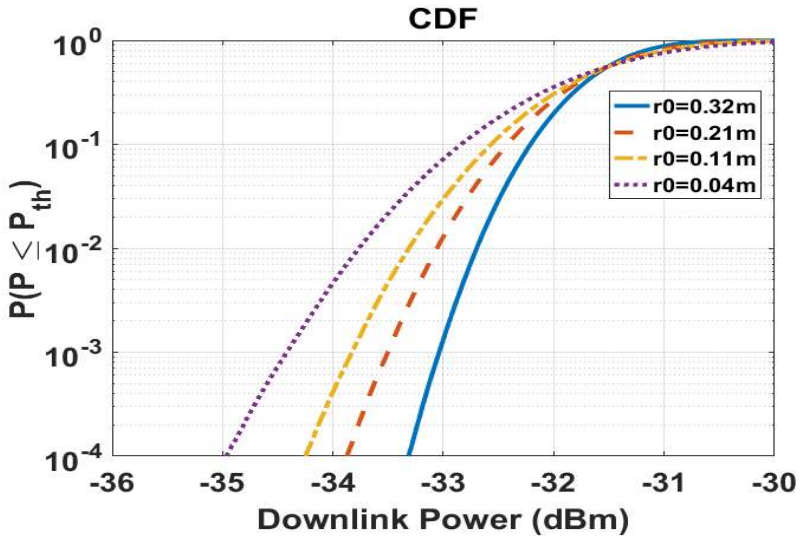

Figure 3-12: Downlink received power for various weather conditions.

In Table 3-4 the resulting Fried parameters and SIs from the numerical data are also given. It is concluded that the worse the turbulence effects the smaller the Fried parameter and the larger the SI, leading to reduced received power as it is easily observed by the simulated CDFs.

Table 3-4: Fried parameter and scintillation index values for different $C_n^2(h)$

V_g (m/s)	A_0	r_0 (m)	SI_{point}
0	10^{-15}	0.32	0.126
8	1.7×10^{-14}	0.21	0.215
12	10^{-13}	0.11	0.302
12	8×10^{-13}	0.04	0.459

3.5 Conclusions

Optical communication satellite systems are the next step to a global network of the upcoming 5G cellular systems as they offer a variety of advantages. Still, they also suffer from harsh atmospheric phenomena. In the case of an optical GEO downlink, air turbulence causes the scintillation of the optical signal, resulting in received irradiance fluctuations. The scintillation effects are more intense for short aperture ground receivers which are the most practical and affordable to employ and therefore the need emerges for scintillation profile modelling. In this Chapter, a time series synthesizer for the accurate prediction of downlink irradiance scintillation is proposed. For modelling, the Rytov weak disturbance theory was considered and the Kolmogorov spatial spectrum was applied along with the integration of stochastic differential equations (SDEs). First and second-order long-term irradiance statistics from the ARTEMIS optical link program were presented and used to validate the proposed methodology successfully. In contrast, numerical results of received power statistics demonstrated the impact of atmospheric turbulence on the optical link.

Chapter References

[1] Illi, E.; El Bouanani, F.; Ayoub, F. A Performance Study of a Hybrid 5G RF/FSO Transmission System. In Proceedings of the 2017 International Conference on Wireless Networks and Mobile Communications (WINCOM), Rabat, Morocco, 1–4 November 2017.

[2] Leitgeb, E. Future Applications of Optical Wireless and Combination Scenarios with RF Technology. In Proceedings of the 2017 40th International Convention on Information and Communication Technology, Electronics and Microelectronics (MIPRO), Opatija, Croatia, 22–26 May 2017.

[3] Jou, B.T.; Vidal, O.; Cahill, J.; Arnal, F.; Honssin, L.M.; Boutin, M.; Chau, D.K. Architecture Options for Satellite Integration into 5G Networks. In Proceedings of the 2018 European Conference on Networks and Communications (EuCNC), Ljubljana, Slovenia, 18–21 June 2018.

[4] Sharma, S.K.; Chatzinotas, S.; Arapoglou, P.D. *Satellite Communications in the 5G Era*, 1st ed.; The Institution of Engineering and Technology: London, UK, 2018.

[5] H. Kaushal, G. Kaddoum, "Optical Communication in Space: Challenges and Mitigation Techniques," in IEEE Comm. Surv. & Tut., no.99, pp.1-1.

[6] H. Hemmati, "Near-Earth Laser Communications" Boca Raton: CRC Press, 2009.

[7] N. K. Lyras, et.al, "Cloud Attenuation Statistics Prediction From Ka-Band to Optical Frequencies: Integrated Liquid Water Content Field Synthesizer," in IEEE Transactions on Antennas and Propagation, vol. 65, no. 1, pp. 319-328, Jan. 2017.

[8] N. K. Lyras et.al, "Optimum Monthly Based Selection of Ground Stations for Optical Satellite Networks," in IEEE Communications Letters, vol. 22, no. 6, pp. 1192-1195, June 2018.

[9] Lyras, N.K.; Kourogiorgas, C.I.; Panagopoulos, A.D. Cloud Free Line of Sight Prediction Modelling for Optical Satellite Communication Network. *IEEE Commun. Lett.* **2017**, *21*, 1537–1540.

[10] Kourogiorgas, C.I.; Lyras, N.; Panagopoulos, A.D.; Tarchi, D.; Vanelli-Coralli, A.; Ugolini, A.; Colavolpe, G.; Arapoglou, P.D. Capacity Statistics Evaluation for Next Generation Broadband MEO Satellite Systems. *IEEE Trans. Aerosp. Electron. Syst.* **2017**, *53*, 2344–2358.

[11] L. Andrews, R. Phillips, "Laser Beam Propagation through Random Media", SPIE Press, 2005.

[12] Kolev, D.R.; Toyoshima, M. Received-Power Fluctuation Analysis for LEO Satellite-to-Ground Laser Links. *J. Lightwave Technol.* **2017**, *35*, 103–112.

[13] A. Alonso, M. Reyes, Z. Sodnik, "Performance of satellite-to-ground communications link between ARTEMIS and the Optical Ground Station". Proc. SPIE 5572, Optics in Atmospheric Propagation and Adaptive Systems, VII, 372, 2004.

[14] M. Toyoshima et al. "Long-term statistics of laser beam propagation in an optical ground-to-geostationary satellite communications link," in IEEE Transactions on Antennas and Propagation, vol. 53, no. 2, pp. 842-850 February 2005.

[15] Yura, H.T., McKinley, W.G., "Aperture averaging of scintillation for space-to-ground optical communications", Applied Optics, vol. 22, no. 11, 1983.

[16] Reyes, M.; Comeron, A.; Alonso, A.; Rodriguez, A.; Rubio, J.A.; Dios, V.F.; Chueca, S.; Sodnik, Z. Ground-to-satellite bidirectional laser links for validation of atmospheric turbulence model. *Proc. SPIE Free Space Laser Commun. Act. Laser Illum. III* **2003**, *5160*, 44–55.

[17] Y. Shao, "The Fractional Ornstein-Uhlenbeck Process as a Representation of Homogeneous Eulerian Velocity Turbulence", Physica D 1995 83, pp. 461-477, 1995.

Chapter 4
Optimum Power Allocation Strategies in Optical Satellite Downlinks and Hybrid Optical Satellite Networks[3,4,5]

The globally introduced 5G mobile networks enable a variety of broadband applications from massive machine type communications (mMTC) to ultra-reliable low latency communications (URLLC). Within this context, optical technologies such as radio over fiber (RoF), radio over free space optics (RoFSO) and optical satellite networks are designated to provide excellent backhaul, relay and gateway services. The integration of optical satellite links in the next-generation networks and in the fifth-generation cellular systems has been proposed to guarantee the handling of the extreme data traffic growth and the high-pitched demand for networks' resources.

In this Chapter, the optical satellite communication downlink is studied and more specifically, a geostationary satellite with multiple transmitters and an optical ground station with multiple receiving terminals are considered. The allocation methodology takes into account the scintillation effects due to atmospheric turbulence and maximizes the ergodic network capacity under total expected power and peak power constraints. The analytical optimizing schemes are based on convex optimization methods and have been inspired by waterfilling algorithm. We present emulated power allocation results using real experimental downlink data from ARTEMIS optical satellite campaign and then we investigate the performance of the proposed algorithm with extended numerical results and comparison with other allocation policies. In particular, the new power allocation strategy achieves the highest

[3]Copyright © 2020 Springer Nature. Reproduced with permission, from: T. T. Kapsis and A. D. Panagopoulos, "Optimum Power Allocation Based on Channel Conditions in Optical Satellite Downlinks," *Wireless Personal Communications,* vol. 116, pp. 2997-3013, 2020. Personal use of this material is permitted, but republication/redistribution requires Springer Nature permission.
[4]Copyright © 2020 IEEE. Reprinted, with permission, from: T. T. Kapsis and A. D. Panagopoulos, "Optimized Power Allocation Scheme in Optical Satellite Communication Downlinks," *2020 12th International Symposium on Communication Systems, Networks and Digital Signal Processing (CSNDSP)*, Porto, Portugal, 2020, pp. 1-6. Personal use of this material is permitted, but republication/redistribution requires IEEE permission.
[5]Copyright © 2021 SPIE. Reprinted, with permission, from: T. T. Kapsis and A. D. Panagopoulos, "Optimized Power Allocation Strategies in Hybrid Optical Satellite Networks," *International*

Conference on Space Optics—ICSO 2020, vol. 11852, SPIE, June 2021. Personal use of this material is permitted, but republication/redistribution requires SPIE permission.
spectral efficiency, according to the power constraints, for various channel conditions and attenuation profiles and also surpasses two simple baseband allocation methods by intelligently taking advantage of the number of channels and the total expected power. The superiority of the new algorithm is shown in terms of bitrate and spectral efficiency through comparison simulations.

Moreover, the power optimization problem is investigated for a fully optical hybrid satellite network. Specifically, the dual hop decode-and-forward optical downlink is considered with a geostationary satellite source, an optical ground gateway and an optical user equipment. The power allocation problem is formulated as a convex optimization problem under separate total and peak power constraints and then a methodology is proposed for the maximization of system's capacity. The proposed methodology takes into account the atmospheric attenuation, the optical channel correlation and turbulence effects and its performance is evaluated through numerical simulations and comparisons with other power allocation implementations. Results regarding the spectral efficiency are presented and commented proving the proposed methodology's superiority.

4.1 Introduction

The satellite communications industry is seeking innovative and efficient solutions to conform to the high demanding standards introduced by the upcoming 5G mobile networks. The applications of satellite networks vary greatly from providing remote connections in disaster events and anyplace on earth, sea and air e.g. trains, ships, aircrafts to assisting the current terrestrial networks [1–4]. Especially, relay services i.e. earth observation and deep space missions as well as backhaul services from/to cell towers through satellite Internet gateways are some of the various use cases of 5G satellite communication links [1–4]. Additionally, mmWave frequencies (Q/V bands) may also be utilized for uplinks to release other useful spectrum and diverse satellite systems consisting of both GEO and LEO can be employed to combine wide coverage with minimal latency [1–4].

The optical technology is undoubtedly the dominant and the most efficient solution of connecting users and computer networks. The fibre optics are used to serve as the backbone of Internet and of every telecommunication infrastructure offering high speed and security [5–6]. Similarly, Free Space Optics (FSO) is a wireless, laser transmitting technology that can provide augmented backhaul or gateway services and comes with a variety of advantages e.g.

cheap operational cost, unlimited and unlicensed bandwidth, EMI security and line of sight (LOS) communication [5–7]. Terrestrial uses include building-to-building links in urban areas and campuses while optical inter satellite and satellite-to-ground links are constantly drawing attention [5–7]. The major limiting factors regarding commercial use are the expensive stabilization and alignment devices and the presence of tall buildings that block the LOS signal. In satellite communications on the other hand the fog, clouds and intense atmospheric phenomena can cause hundreds of dBs attenuation leading to the blockage of the link. Moreover, scintillation due to atmospheric turbulence, leads to received power fluctuations, both temporal and spatial [5–7]. Especially, the Cloud Free Line of Sight (CFLOS) probability for GEO and MEO links is closely investigated in [8–9] and some prediction models have been proposed. In [10–11] the problem of optimal selection of optical ground stations ensuring target link availabilities with a view to minimize the optical network is studied.

For an optical satellite network, in order to achieve increased transmission rate and spectral efficiency one could employ higher order modulation schemes but that would certainly result in higher bit error rate due to the unstable weather conditions [5–7]. Another technique would be Wavelength Division Multiplexing (WDM) since it allows transmitting different bit streams in parallel using non-overlapping optical carriers [5–7]. However, the spatial correlation between the channels is strong therefore this technique lacks the flexibility to mitigate the atmospheric effects. A more costly in overhead but very effective way to improve bit rate and address the atmospheric problem is the employment of Multiple Input Multiple Output (MIMO) Spatial Multiplexing technique [12]. It requires multiple optical telescopes for transmission and reception, placed in a distance large enough so that the parallel channels are considered uncorrelated.

MIMO-based relay systems are commonly employed to improve reliability and coverage especially when the direct link qualities are poor and the need for cooperative or two-hop communication emerges [13]. The relay transmission schemes are classified primarily into decode-and-forward (DF) and amplify-and-forward (AF) where the DF is better opted for good source-relay channels [13]. The power allocation problem for two-hop, MIMO-based relay networks has been studied in [14–15] and methodologies have been proposed for uncorrelated Rayleigh channels.

In this Chapter, we consider an optical GEO satellite-to-ground downlink in a parallel MIMO channel configuration and propose an optimal power allocation methodology inspired by waterfilling algorithm that takes into account the effects of the turbulent atmospheric channels. Additionally, a power allocation methodology is proposed for a hybrid fully optical

satellite network comprising of a GEO satellite multi-channel source, an optical ground relay station (gateway) and an optical user equipment (edge node). A dual hop, DF scheme is employed for the downlink optical channels that are affected by attenuation, scintillation and spatial correlation. The objective function that is optimized is the network's ergodic capacity under the total expected power constraint and the peak transmitting power limitation e.g. to avoid non-linearities of the amplifiers. The optimization problem is decomposed into simpler, independent convex sub-problems that are solved using the appropriate theory in [16–17]. The whole methodology is guided by the well-known waterfilling algorithm [12]. The contributions of this Chapter are summarized as follows:

i. A novel power allocation methodology and an iterative allocation algorithm are presented for a next generation optical satellite downlink with multiple transmitters and multiple receivers.
ii. A power allocation scheme is proposed for a hybrid fully optical satellite network comprising of a GEO satellite multi-channel source, an optical ground relay station (gateway) and an optical user equipment (edge node). A dual hop, DF scheme is employed for the downlink optical channels that are affected by attenuation, scintillation and spatial correlation. The transmitting nodes have separate powers therefore the power allocation is performed with respect to both source's and relay's power constraints.
iii. The satellite downlink's ergodic capacity under the total expected power constraint and the peak transmitting power limitation is optimized.
iv. Real experimental downlink data have been employed to apply the proposed allocation strategies.
v. The algorithm is presented under both weak and strong turbulence conditions therefore the extreme cases of clear air turbulence.
vi. Network simulations with numerical data investigating the sensitivity of the algorithm to scintillation and to atmospheric attenuation are presented.
vii. The proposed algorithm is very flexible, it converges rapidly and scales well with the number of channels.

The remainder of the Chapter is structured as follows: in Section 4.2 the system architectures and channel models are given including the necessary theory, formulas and the main assumptions; in Section 4.3 the power allocation problems for the optical satellite networks under examination are reported, followed by the proposed methodology and the

proposed iterative algorithm; in Section 4.4 network emulations and simulations are executed and the outcomes are presented and commented; Section 4.5 concludes this Chapter.

4.2 System Model and Channel Model

4.2.1 System and Channel Model for a parallel MIMO optical satellite downlink

The first system model is an optical satellite network consisting of a geostationary satellite equipped with N optical transmitters (T_x) and an optical MIMO ground receiver with N telescopes (R_x) establishing N one-to-one optical downlinks. The communication channels use the same wavelength $\lambda(m)$ and an Intensity Modulation/Direct Detection (IM/DD) scheme is employed. Moreover, perfect pointing and tracking conditions are assumed thus neglecting possible co-channel interferences, alignment and orbital errors. Also, the atmosphere is assumed free of clouds and fog in our analysis. The optical elements must be sufficiently spatially separated in order the parallel optical channels to be uncorrelated and independent. To secure the decorrelation, the receivers are installed in distances greater than Fried parameter. The Fried parameter $r_0(m)$ is defined as the coherence length of the atmosphere and incorporates the turbulence profile [18–20]:

$$r_0 = \left[0.423k^2 \sec(\zeta) \int_{H_{GND}}^{H_{GEO}} C_n^2(z)dz \right]^{-3/5} \tag{4.1}$$

where $k = 2\pi/\lambda$ (rad/m) is the wavenumber, sec() is the secant function, ζ is the zenith angle, $C_n^2(z)$ is the refractive index structure parameter, $z(m)$ is the altitude on the vertical path and H_{GEO}, H_{GND} are the heights of the GEO satellite and the ground receiver. The $C_n^2(z)$ depends heavily on the ground weather conditions e.g. wind speed, day/night time, temperature while the Hufnagel-Valley model is commonly used [18–20]. In Figure 4-1 a simplified illustration of an optical satellite downlink with multiple receivers is depicted.

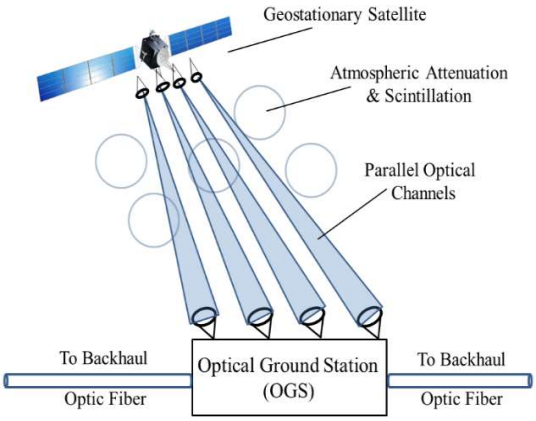

Figure 4-1: Parallel MIMO optical satellite network for downlink backhaul services.

Strong turbulence leads to small values of r_0 (few centimetres) while weak turbulence to a larger r_0 (few decimetres) and for distances over Fried's length the channels are assumed uncorrelated.

In the optical downlink propagation, there is signal attenuation due to molecule absorption, beam spreading due to diffraction but most importantly irradiance scintillation which is a phenomenon similar to a star twinkling due to anomalies in the refractive index. Therefore, an explicit model for the optical channel is:

$$h = h_{att} \cdot h_{sc\,\mathrm{int}} \tag{4.2}$$

where h_{att} is the propagation attenuation term given by [18-19]:

$$\left|h_{att}\right|^2 = \eta_{Tx} \cdot \eta_{Rx} \cdot \eta_{Atm} \cdot G_{Tx} \cdot G_{Rx} \cdot FSL \tag{4.3}$$

where η_{Tx}, η_{Rx} are the quantum efficiencies of transmitter and receiver, η_{Atm} is the atmospheric transmittance, G_{Tx}, G_{Rx} are the aperture gains of transmitter and receiver and FSL are the free space losses. Finally, $h_{sc\,\mathrm{int}}$ is the scintillation effect with [20]:

$$\left|h_{sc\,\mathrm{int}}\right|^2 = e^{2X_{\mathrm{scint}}} = I/\langle I \rangle \tag{4.4}$$

where X_{scint} is the log-amplitude of the optical wave, I is the received irradiance and $\langle I \rangle$ is the average received irradiance.

The turbulence strength is measured with the scintillation index (SI) which constitutes the normalized variance of the received irradiance [18–20]:

$$\sigma_I^2 = \left(\langle I^2 \rangle - \langle I \rangle^2\right) / \langle I \rangle^2 \tag{4.5}$$

For weak turbulence (SI<1) and for very small (point) receivers the following formula is provided from Rytov theory [18–20]:

$$\sigma_{I,po\,\mathrm{int}}^2 = 2.25k^{\frac{7}{6}} \sec^{\frac{11}{6}}(\zeta) \int_{H_{GND}}^{H_{GEO}} C_n^2(z)(z - H_{GND})^{\frac{5}{6}}\, dz \tag{4.6}$$

and I follows the lognormal distribution with Probability Density Function (PDF) [5–7]:

$$\mathrm{f}_I(I) = \frac{1}{I\sqrt{2\pi}\sigma_I} \exp\left\{ -\frac{\left[\ln\left(I/\langle I\rangle\right) + \frac{1}{2}\sigma_I^2\right]^2}{2\sigma_I^2} \right\} \tag{4.7}$$

For strong turbulence conditions $(\mathrm{SI} > 1)$ I is a Gamma - Gamma distributed process with PDF [5–7]:

$$\mathrm{f}_I(I) = \frac{2(ab)^{\frac{a+b}{2}}}{\Gamma(a)\Gamma(b)} \left(\frac{I}{\langle I\rangle}\right)^{\frac{a+b}{2}-1} \mathrm{K}_{a-b}\left(2\sqrt{ab\frac{I}{\langle I\rangle}}\right) \tag{4.8}$$

where K_x is the x-order modified Bessel function of the second kind, $\Gamma(\ )$ is the gamma function and *a, b* are parameters that are related to the large-scale and to the small-scale scintillation accordingly and are connected to the SI as follows [5–7]:

$$\sigma_I^2 = \frac{1}{a} + \frac{1}{b} + \frac{1}{ab} \tag{4.9}$$

The channel's *i* instantaneous SNR can be expressed as follows [18–20]:

$$\mathrm{S/N}_i = \frac{P_{t_i} \cdot |h_i|^2}{\sigma_{\mathrm{N}_{opt}}^2} = P_{t_i} \cdot \frac{|h_{att,i}|^2}{\sigma_{th}^2 + \sigma_{shot}^2 + \sigma_{bkg}^2} \cdot e^{2X\mathrm{scint}} \tag{4.10}$$

where σ_{th}^2 is the thermal noise variance, σ_{shot}^2 is the shot noise variance and σ_{bkg}^2 is the background radiation noise variance [21]. In our analysis the noise variances shall be considered constant and independent of the transmitted power P_{t_i}. Let γ_i be the channel's *i* state:

$$\gamma_i = \frac{|h_{att,i}|^2}{\sigma_{th}^2 + \sigma_{shot}^2 + \sigma_{bkg}^2} \cdot e^{2Xsc\,\mathrm{int}} = \langle \gamma_i \rangle \cdot e^{2Xsc\,\mathrm{int}} \tag{4.11}$$

where $\langle \gamma_i \rangle$ declares the average optical channel gain. It is easily observed from (4.6), (4.13) that γ is also log-normally distributed with parameters $\mu = \langle \gamma \rangle$ and $\sigma_\gamma^2 = \sigma_I^2$. The Channel State Information (CSI) is assumed that is perfectly known both to T_xs and to R_xs.

4.2.2 System and Channel Model for a hybrid fully optical satellite network

The second system model under investigation is a three-node network consisting of a GEO satellite source equipped with N_T optical transmit telescopes, an optical ground relay station (OGRS) with N_T optical transmit and N_R optical receive telescopes installed, and the optical ground user station (OGUS) with also N_R optical receivers. The GEO-OGRS and OGRS-OGUS links form N_R x N_T optical MIMO antenna systems and is assumed that the channels are correlated in general and half-duplex which implies that the end-to-end transmission takes place in two distinct time slots. In Figure 4-2 a simplified illustration of a three-node hybrid fully optical satellite network with multiple receivers is depicted.

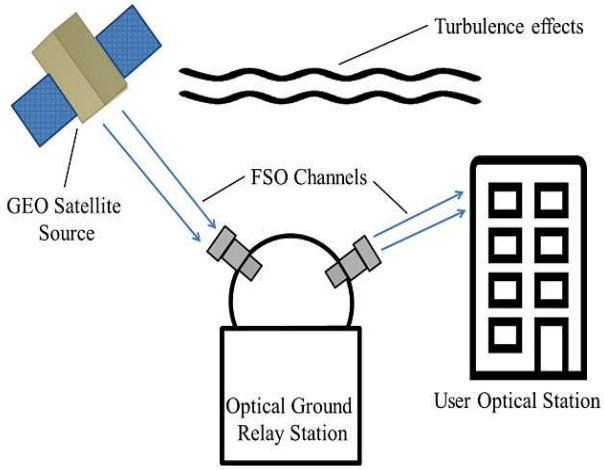

Figure 4-2: Network architecture. The GEO source, the OGRS gateway and the OGUS form hybrid optical MIMO systems over correlated, turbulent channels.

The channel spatial correlation depends on many factors i.e., the aperture size, the optical link distance, the type of turbulence and primarily the transmitter/receiver element spacing [22–23]. The spatial correlation coefficient between channels *n* and *m* of distance d_{nm} is given by the following expression [22–23]:

$$\rho_{nm}(d_{nm}) = \frac{R_{nm}(d_{nm})}{\sqrt{\sigma_{I,n}^2 \sigma_{I,m}^2}} \tag{4.14}$$

where $-1 \le \rho_{nm} \le 1$ is the spatial correlation coefficient, R_{nm} is the spatial covariance and σ_I^2 is the scintillation index which is defined as the normalized variance of the received irradiance. The spatial covariance of channels *n* and *m* is in turn [23]:

$$R_{nm}(d_{nm}) = \frac{\langle I_n I_m \rangle}{\langle I_n \rangle \langle I_m \rangle} - 1 \tag{4.15}$$

Regarding the communication technical characteristics, the simple On-Off-Keying NRZ (OOK-NRZ) modulation scheme is employed for transmission and the Direct Detection (DD) decoding scheme for reception while the optical wavelength is assumed equal to $\lambda = 1550$ nm. The optical link pointing/tracking errors are assumed arbitrarily small and therefore neglected while a feedback channel provides CSIT knowledge to both source and relay. Cloud-free conditions are presumed. Only the atmospheric attenuation and turbulence are considered.

4.3 Optimal Power Allocation

4.3.1 Proposed methodology for a parallel MIMO optical satellite downlink

In this Section, the power allocation problem for the MIMO optical satellite network is developed by defining our objective function and the power constraints and solving it afterwards using convex optimization methods. Specifically, the network's channel capacity is given by [24–27]:

$$\sum_{i=1}^{N} C_i = \sum_{i=1}^{N} \log_2(1 + P_{t_i} \cdot \gamma_i) \text{ (bps/Hz)} \tag{4.16}$$

Due to downlink scintillation, a more useful metric is the ergodic network capacity [24–27] that is to be maximized with respect to the transmitting power P_{t_i}. The problem is defined then as follows:

$$\arg\max_{P_{t_i}} \mathrm{E}\left[\sum_{i=1}^{N} \log_2(1 + P_{t_i} \cdot \gamma_i)\right] \tag{4.17}$$

$$\text{s.t. } 0 \le P_{t_i} \le \overline{P_{peak}} \text{ and } \mathrm{E}\left[\sum_{i=1}^{N} P_{t_i}\right] \le \overline{P_{total}} \tag{4.18}$$

where $\overline{P_{peak}}$ is the peak power that can be allocated to a single channel and $\overline{P_{total}}$ is the total expected power constraint.

The above optimization problem can be decomposed into N parallel maximization sub-problems since the channels are uncorrelated:

$$\arg\max_{P_{t_i}} \sum_{i=1}^{N} \mathrm{E}\left[\log_2(1 + P_{t_i} \cdot \gamma_i)\right] = \arg\max_{P_{t_i}} \sum_{i=1}^{N} \int_0^{\infty} \log_2(1 + P_{t_i} \cdot \gamma_i) \, \mathrm{f}_{\gamma}(\gamma_i) \mathrm{d}\gamma_i \tag{4.19}$$

Each sub-problem of the initial optimization problem is expressed then as:

$$\arg\max_{P_{t_i}} \int_0^{\infty} \log_2(1+P_{t_i}\cdot\gamma_i)\,\mathrm{f}_\gamma(\gamma_i)\mathrm{d}\gamma_i \tag{4.20}$$

s.t. (4.18)

which is a convex, constrained maximization problem.

The solution is stated below while the proof is extensively described in the "4.6 Appendix: Proof of the optimal solution".

$$P_{t_i}^* = \min\left\{\overline{P_{peak}}, \max\left\{\frac{1}{\nu}-\frac{1}{\gamma_i}, 0\right\}\right\} \tag{4.21}$$

The methodology steps are based on the waterfilling algorithm and is based on the formation of the Lagrangian function and the transformation of the initial constrained problem to an unconstrained, convex one. Afterwards the well-known Karush–Kuhn–Tucker (KKT) conditions are applied since they are necessary and sufficient to provide the optimal transmitted power in (4.21). In [28–30] similar problems have been investigated. The results are like the waterfilling principle i.e. the good channels (large γ_i so $1/\gamma_i$ small) are allowed to transmit more power $\left(1/\nu - 1/\gamma_i\right)$ but no more than $\overline{P_{peak}}$. The multiplier ν is derived by the following transcendental equation:

$$\begin{aligned} &\mathrm{E}\left[\sum_{i=1}^{N} P_{t_i}^*\right] = \overline{P_{total}} \Leftrightarrow \sum_{i=1}^{N}\int_0^{\infty} P_{t_i}^*\,\mathrm{f}_\gamma(\gamma_i)\mathrm{d}\gamma_i = \overline{P_{total}} \Leftrightarrow \\ &\Leftrightarrow \sum_{i=1}^{N}\left[\int_{\nu}^{\frac{\nu}{1-\nu\overline{P_{peak}}}}\left(\frac{1}{\nu}-\frac{1}{\gamma_i}\right)\mathrm{f}_\gamma(\gamma_i)\mathrm{d}\gamma_i + \int_{\frac{\nu}{1-\nu\overline{P_{peak}}}}^{\infty}\overline{P_{peak}}\,\mathrm{f}_\gamma(\gamma_i)\mathrm{d}\gamma_i\right] = \overline{P_{total}} \end{aligned} \tag{4.22}$$

The solution to (4.22) can be found numerically employing iterative root-finding algorithms e.g. bisection method, secant method, Newton's method [31]. Especially the simpler bisection method only requires an interval with a sign change to converge to the root of the equation. This interval is the $\nu\in\left(0, 1/\overline{P_{peak}}\right)$ because $\nu>0$ and $1-\nu\overline{P_{peak}}>0$ as implied from (4.22). Finally, the optimal average rate (bps/Hz) is:

$$\sum_{i=1}^{N}\mathrm{E}[C_i] = \sum_{i=1}^{N}\left[\int_{\nu}^{\frac{\nu}{1-\nu\overline{P_{peak}}}}\log_2\left(\frac{\gamma_i}{\nu}\right)\mathrm{f}_\gamma(\gamma_i)\mathrm{d}\gamma_i + \int_{\frac{\nu}{1-\nu\overline{P_{peak}}}}^{\infty}\log_2\left(1+\overline{P_{peak}}\gamma_i\right)\mathrm{f}_\gamma(\gamma_i)\mathrm{d}\gamma_i\right] \tag{4.23}$$

In case that there are available time series (data) for the atmospheric turbulence either from real experimental campaigns or realistic time series synthesizers, they can be used for the

emulation of the power allocation schemes. Therefore, for the emulation an iterative algorithm must be employed to approximate the solution for a given error tolerance. The proposed algorithm (**Algorithm 1**) converges to the optimal value of v and to the maximum ergodic capacity of the optical network.

Algorithm 1. Iterative Power Allocation Algorithm

---

1) Input parameters:
Enter the number of optical channels N,
the experimental data vectors $\mathbf{D}_i$ for $i = 1,2,3\ldots N$,
the experimental data vector length M
and the desired power constraints $\overline{P_{peak}}$, $\overline{P_{total}}$.

2) Initialization:
Enter the step size $t^{(0)}$, the dual variable $v^{(0)}$, the tolerance ε
and the iteration index $k = 0$.

3) Iterative methodology
do
  for i = 1 *to* N with step 1
    for j = 1 *to* M with step 1
    calculate the optimal power $P_{t_i}^{\bullet}$ *for the j channel state*:
    $P_{t_i}^{\bullet} = \min\left(\overline{P_{peak}}, \max\left\{0,\ 1/v^{(k)} - 1/\mathbf{D}_i(j)\right\}\right)$;
    calculate the average channel power and capacity:
    $pav(i) \mathrel{+}= P_{t_i}^{\bullet} \cdot \mathrm{f}_{\gamma}(j)$;
    $cav(i) \mathrel{+}= \log_2\left(1 + P_{t_i}^{\bullet} \cdot \mathbf{D}_i(j)\right) \cdot \mathrm{f}_{\gamma}(j)$;
    end
  divide by the sum to obtain probability density:
  $pav(i) = pav(i) / \sum_{j=1}^{M} \mathrm{f}_{\gamma}(j)$;
  $cav(i) = cav(i) / \sum_{j=1}^{M} \mathrm{f}_{\gamma}(j)$;
  end
compute the total average power $S = \sum_{i=1}^{N} pav(i)$;
update and check:
$v^{(k+1)} = v^{(k)} - t^{(k)}\left(\overline{P_{total}} - S\right)$;
$t^{(k+1)} = t^{(k)} / \left(k+1\right)$;
$k = k+1$;
while $|v^{(k+1)} - v^{(k)}| > \varepsilon$;
compute the maximum ergodic sum rate $C = \sum_{i=1}^{N} cav(i)$;

The Algorithm 1 employs a subgradient method with diminishing step size to find the optimal value v^* therefore it is proved that it converges with rate of $O(1/\varepsilon^2)$ [32]. However, with a good initial guess e.g. $v^{(0)} = 0.5/\overline{P_{peak}}$ and $t^{(0)} = 0.1$ no more than 50 iterations are usually needed.

Finally, in the case of non-ideal conditions i.e. imperfect pointing and alignment issues there will be channel interference and crosstalk. The average rate will be given then by the expressions (12) and (13) in [27] and the optimization problem may not be convex leading to a possible locally optimal solution and consequently lower network capacity. Moreover, the uncertainty of CSI would require a different, more robust approach similar to [33]. The incorporation of the non-ideal conditions and the uncertainties in the optimization procedure is a subject of future work.

4.3.2 Proposed methodology for a hybrid fully MIMO optical satellite network

The GEO-OGRS and OGRS-OGUS optical MIMO channel matrices will be referred to as $\mathbf{H}_1$ and $\mathbf{H}_2$ respectively of dimensions N_R x N_T. The systemic expressions are the following:

$$\mathbf{Y}_1 = \mathbf{H}_1\mathbf{X}_1 + \mathbf{n}_1 \tag{4.24}$$

$$\mathbf{Y}_2 = \mathbf{H}_2\mathbf{X}_2 + \mathbf{n}_2 \tag{4.25}$$

where $\mathbf{Y}_{1,2}$ are the received signal vectors of OGRS and OGUS respectively, $\mathbf{X}_{1,2}$ are the transmitted signal vectors of GEO and OGRS respectively and $\mathbf{n}_{1,2}$ are the optical detection noise vectors. There are three independent detection noise sources: The electronics noise e.g., thermal noise, the shot noise due to photonic interactions and the beat noise e.g., background radiation, amplified spontaneous emissions [5–7]. The optical noise variance shall be assumed constant in this analysis although it's a function of the incident optical power. Therefore:

$$\sigma_n^2 = \sigma_{elec}^2 + \sigma_{shot}^2 + \sigma_{beat}^2 = \text{const.} \tag{4.26}$$

The optical signal propagation through the atmosphere is deteriorated by the atmospheric attenuation and turbulence that cause irradiance losses and scintillation [18–19]:

$$I = I_{avg} \cdot e^{2X_t} \tag{4.27}$$

where I_{avg} is the average received irradiance and X_t is a random process representing the log-amplitude of the field fluctuations.

The average irradiance term for a collimated Gaussian beam is [18–19]:

$$I_{avg} = \frac{2}{\pi} P_t \cdot \eta_t \cdot \eta_r \cdot \eta_{atm} \cdot \frac{1}{W^2(D)} \cdot \exp\left(\frac{-2r^2}{W^2(D)}\right) \tag{4.28}$$

where η_t, η_r are the quantum efficiencies of the transmitter and receiver, η_{atm} is the atmospheric transmittance, D(m) is the optical link distance, r is the radial distance from the beam center and $W(D)$(m) is the beam waist after propagation of distance D. For perfect link pointing the r=0 and only the beam spreading effects take place.

The variance of X_t is directly related to the scintillation index (SI) according to the following formula [5–7]:

$$\sigma_I^2 = e^{4\sigma_{X_t}^2} - 1 \tag{4.29}$$

The special case of weak turbulence (SI<1) was thoroughly studied by Rytov from whom a theoretical closed-form expression for SI was derived [5–7]:

$$\sigma_I^2 = 2.25 k^{\frac{7}{6}} \sec^{\frac{11}{6}}(\zeta) \int_{A_{OGRS}}^{A_{GEO}} \mathrm{C}_\mathrm{n}^2(z)\left(z - A_{OGRS}\right)^{\frac{5}{6}} dz \tag{4.30}$$

Moreover, for satellite links with elevation angle greater than 20 degrees, I is a log-normally distributed process with Probability Density Function (PDF) [1], [18–19]:

$$\mathrm{f}_I(I) = \frac{1}{I\sqrt{2\pi}\sigma_I} \exp\left\{ -\frac{\left[\ln\left(I / I_{avg}\right) + \frac{1}{2}\sigma_I^2\right]^2}{2\sigma_I^2} \right\} \tag{4.31}$$

The channel capacity of the optical MIMO DF dual hop system in (bps/Hz) is derived from the Shannon theorem as [13–14]:

$$C_s = \min\left(C_1, C_2\right) \tag{4.32}$$

where the correspondent capacities in (4.32) are expressed as [14–15]:

$$C_1 = \frac{1}{2}\log_2\left|\mathbf{I} + \frac{1}{\sigma_n^2}\mathbf{H_1}\mathbf{Q_1}\mathbf{H_1^H}\right|,\ C_2 = \frac{1}{2}\log_2\left|\mathbf{I} + \frac{1}{\sigma_n^2}\mathbf{H_2}\mathbf{Q_2}\mathbf{H_2^H}\right| \tag{4.33}$$

where $\mathbf{I}$ (N_RxN_R) is the identity matrix, $\mathbf{Q_1}$ and $\mathbf{Q_2}$ are the covariance matrices of transmitted symbols $\mathbf{X_1}$ and $\mathbf{X_2}$ accordingly. From the Singular Value Decomposition (SVD) technique we obtain parallel, independent fading channels [14]:

$$\mathbf{H_1} = \mathbf{U}_1\mathbf{\Lambda}_1\mathbf{V}_1^H, \mathbf{H}_2 = \mathbf{U}_2\mathbf{\Lambda}_2\mathbf{V}_2^H \tag{4.34}$$

$$\mathbf{X_1} = \mathbf{V}_1\widetilde{\mathbf{X_1}},\ \mathbf{X}_2 = \mathbf{V}_2\widetilde{\mathbf{X}_2}, \widetilde{\mathbf{Y_1}} = \mathbf{U}_1^H\mathbf{Y_1}, \widetilde{\mathbf{Y}_2} = \mathbf{U}_2^H\mathbf{Y}_2 \tag{4.35}$$

$$\widetilde{\mathbf{Y_1}} = \mathbf{\Lambda}_1\widetilde{\mathbf{X_1}} + \widetilde{\mathbf{n}}_1, \widetilde{\mathbf{Y}_2} = \mathbf{\Lambda}_2\widetilde{\mathbf{X}_2} + \widetilde{\mathbf{n}}_2 \tag{4.36}$$

The (4.33) are then transformed to:

$$C_1 = \frac{1}{2}\sum_{k=1}^{rank(\mathbf{H}_1)} \log_2\left(1+\frac{P_{1,k}\cdot\gamma_{1,k}^2}{\sigma_n^2}\right), C_2 = \frac{1}{2}\sum_{k=1}^{rank(\mathbf{H}_2)} \log_2\left(1+\frac{P_{2,k}\cdot\gamma_{2,k}^2}{\sigma_n^2}\right) \tag{4.37}$$

where $P_{i,k}$ (i=1,2) are the transmitted powers regarding the GEO and OGRS transmitters, $\gamma_{i,k}$ (i=1,2) are the eigenvalues of matrices $\mathbf{\Lambda_1}$ and $\mathbf{\Lambda_2}$.

In this Section, the power allocation problem for an optical MIMO DF dual hop network is firstly structured and then a methodology is proposed that maximizes the system's capacity with respect to separate power constraints. The optimization problem is formulated as follows:

$$\text{PA1}: \quad \left\{P_{1,k}^*, P_{2,k}^*\right\} = \arg\max_{P_{i,k}} \min\left(C_1, C_2\right) \tag{4.38}$$

$$\text{s.t.} \quad 0 \le P_{1,k} \le P_{peak,1}, 0 \le P_{2,k} \le P_{peak,2}$$
$$\sum_{k=1}^{N_T} P_{1,k} \le P_{total,1}, \sum_{k=1}^{N_T} P_{2,k} \le P_{total,2} \tag{4.39}$$

where $P_{1,k}^*, P_{2,k}^*$ are the optimum transmission powers of channel k for GEO and OGRS accordingly, $P_{peak,i}$ (i=1,2) is the GEO peak transmitting power constraint and $P_{total,i}$ (i=1,2) is the OGRS total transmitting power constraint. In order to solve the max-min problem efficiently, the following transformation is applied:

$$\text{PA2}: \quad \left\{P_{1,k}^*, P_{2,k}^*\right\} = \arg\max_{P_{i,k}} \theta \tag{4.40}$$

$$\text{s.t. } \theta \le C_1, \theta \le C_2 \text{ and } (4.39) \tag{4.41}$$

where the slack variable θ is the minimum of C_1, C_2.

The PA2 is now in standard form to be solved with convex techniques since the objective function is the minimum of two concave functions and the constraints are also convex. Firstly, the Lagrangian is formed for the channel k but we will omit the k index notation [16–17]:

$$L(P_1^*, P_2^*) = \theta - \lambda_1(\theta - C_1) - \lambda_2(\theta - C_2) - \mu_1(P_1^* - P_{peak,1}) - \mu_2(P_2^* - P_{peak,2}) - \nu_1(\sum_{k=1}^{N_T} P_1^* - P_{total,1}) - \nu_2(\sum_{k=1}^{N_T} P_2^* - P_{total,2}) \tag{4.42}$$

where λ_i, μ_i, ν_i (i=1,2) are the non-negative Lagrange multipliers. Then the Karush-Kuhn-Tucker conditions are necessary and sufficient therefore we obtain [16–17]:

$$\nabla \cdot L(P_1^*, P_2^*) = 0 \Rightarrow \begin{cases} \dfrac{\partial L(P_1^*, P_2^*)}{\partial P_1^*} = 0 \\ \dfrac{\partial L(P_1^*, P_2^*)}{\partial P_2^*} = 0 \end{cases} \tag{4.43}$$

By calculating the first derivatives and applying the complementary slackness conditions we get:

$$P_1^* = \min\left\{P_{peak,1}, \max\left\{\frac{1}{\nu_1} - \frac{\sigma_n^2}{\gamma_1^2}, 0\right\}\right\},\ P_2^* = \min\left\{P_{peak,2}, \max\left\{\frac{1}{\nu_2} - \frac{\sigma_n^2}{\gamma_2^2}, 0\right\}\right\} \tag{4.44}$$

where the dual multipliers $\nu_1,\ \nu_2$ are computed numerically from the total power equations given below:

$$\sum_{k=1}^{N_T} P_{1,k}^* = P_{total,1}, \sum_{k=1}^{N_T} P_{2,k}^* = P_{total,2} \tag{4.45}$$

A root-finding algorithm such as the iterative subgradient method or the bisection method can be equally employed to solve for the ν_1, ν_2 optimal values. It is shown from (4.46) that ν_i lie in the interval $(0,\ 1/P_{peak,i})$ so an initial choice e.g. $\nu_i(0) = 0.5/P_{peak,i}$ and a small fixed step size e.g. 1e-3 are usually sufficient to rapidly converge to the optimum solution.

$$\sum_{k=1}^{N_T}\left(\frac{1}{\nu_i} - \frac{\sigma_n^2}{\gamma_i^2}\right) = P_{total,i} \Rightarrow \frac{1}{\nu_i} = \frac{1}{N_T}\left[P_{total,i} + \sum_{k=1}^{N_T}\frac{\sigma_n^2}{\gamma_i^2}\right] \Rightarrow \frac{1}{\nu_i} \geq \frac{P_{total,i}}{N_T} \geq P_{peak,i} \Rightarrow \nu_i \leq \frac{1}{P_{peak,i}} \tag{4.46}$$

4.4 Numerical Results and Discussion

4.4.1 Proposed methodology for a parallel MIMO optical satellite downlink

In this Section, the proposed power allocation methodology and algorithm will be evaluated firstly through emulations with experimental data and then there are presented network simulations and yielded numerical results investigating the sensitivity to scintillation and atmospheric attenuation as well as the scalability and the performance compared to other known algorithms.

For the emulation part, the channels' time series are provided by downlink irradiance measurements from the ARTEMIS optical satellite link campaign, a bidirectional data relay experiment carried out in 2003 by the European Space Agency (ESA) and JAXA [34–36]. It consisted of the GEO ARTEMIS satellite and ESA's optical ground station (OGS) in Tenerife, Spain that was equipped with a 1 m diameter telescope and a smaller 0.26 m aperture called LUCE terminal. In Figure 4-3 the irradiance PDF of an optical channel

computed directly from the ARTEMIS-to-LUCE downlink data is compared to the theoretical PDF of a lognormal distribution with the same mean and variance parameters: $\mu = 30.87\, nW/m^2$, $\sigma_I^2 = 0.0101$.

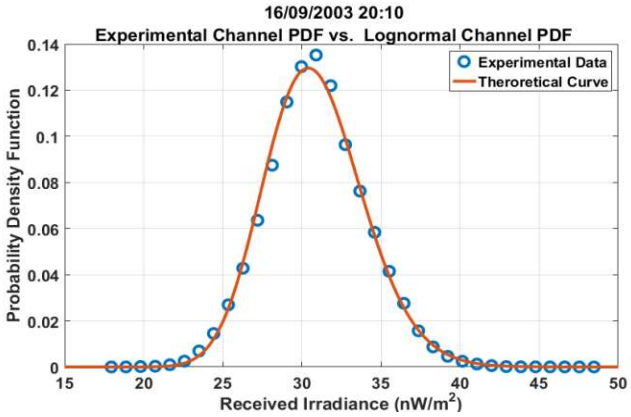

Figure 4-3: PDF of experimental data from ARTEMIS sessions versus PDF of lognormal distribution under weak turbulence conditions.

Table 4-1: Emulation input parameters

Channels	$\langle \gamma_i \rangle$	$\sigma^2_{\gamma_i}$	$r_0\,(cm)$
Ch. 1	1.0	0.0142	33
Ch. 2	1.0	0.0101	36
Ch. 3	1.0	0.0274	7
$\overline{P_{peak}} = 1$ W			

It is easily can be seen that the theoretical PDF curve reproduces the experimental one with great accuracy. For the emulation purposes we consider an 3×3 optical satellite MIMO network where the channels' time series are derived from ARTEMIS experimental sessions. The purpose is to exclusively examine the Algorithm's 1 sensitivity to weak(lognormal) scintillation so the channels' SNRs are normalized as it is reported in Table 4-1. The Fried parameter was calculated using the ARTEMIS-to-OGS technical details i.e. operating wavelength λ = 819 nm, elevation angle = 37°, H_{GND} = 2400 m, H_{GEO} = 35,787 km and the provided weather data for the C_n^2 estimation. The peak power is 1 W.

In Figure 4-4 the average power distribution to the three optical satellite channels and the maximum ergodic network capacity as a function of total expected power for the various scintillation indices are exhibited. It is deduced that the proposed algorithm allocates more power to the channels suffered by less turbulence. Here channel 2 has the smallest SI and transmits the most average power while channel 3 has the largest SI and transmits the least.

Moreover, the power constraints are held since each channel does not exceed the 1 W limitation and the total channel power does not exceed the expected $\overline{P_{total}}$. At $\overline{P_{total}} = 3$ W all channels transmit 1 W each. The maximum ergodic capacity also increases with the total expected power.

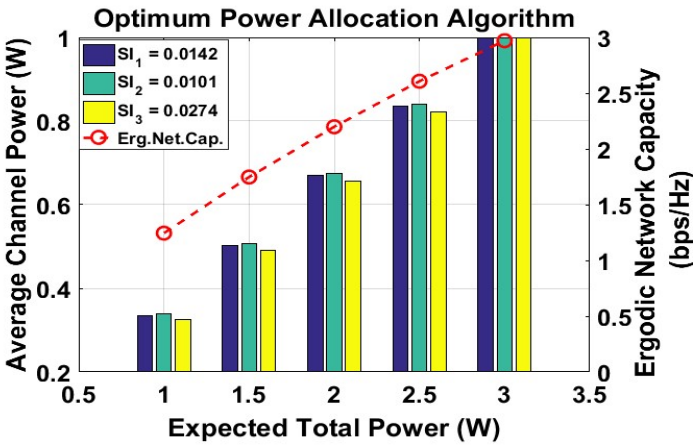

Figure 4-4: Proposed power allocation algorithm and maximum ergodic capacity for a 3×3 network versus the expected total power. Real experimental data.

In Figure 4-5 the performance comparisons between the proposed algorithm and two baseline power allocation algorithms: The Equal Power algorithm (EPA) and the Equal SNR or Channel Inversion algorithm (CINVA) are also demonstrated. The emulation input settings are the same as previously. It is concluded that the proposed algorithm achieves slightly higher spectral efficiency than the other two policies and at $\overline{P_{total}} = 3$ W it degenerates to the EPA which constitutes a moderate solution while CINVA the worst of them.

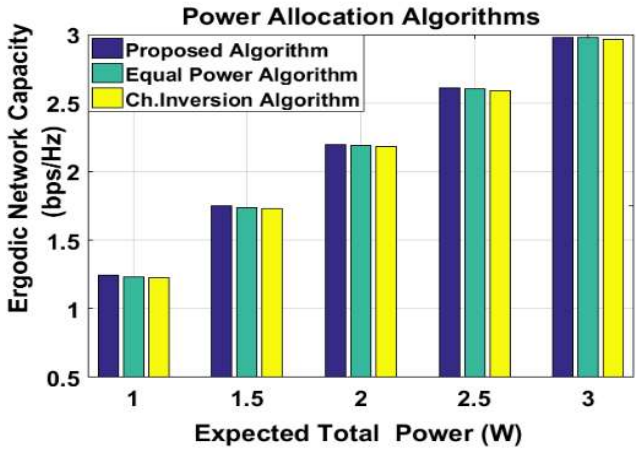

Figure 4-5: Various power allocation policies. The proposed algorithm achieves the largest network capacity.

Afterwards, a satellite downlink simulation is realized considering a 4×4 optical satellite MIMO system to exclusively examine the sensitivity of the proposed methodology to atmospheric attenuation while the clear air turbulence is considered the same for all channels as it is reported in Table 4-2. The wavelength is set to λ = 1550 nm, the zenith angle ζ = 50°, the altitudes H_{GND} = 1500 m and H_{GEO} = 357,87 km. The peak power is 1 W.

Table 4-2: Simulation input parameters

Channels	$\langle \gamma_i \rangle$	$\sigma_{\gamma_i}^2$	$r_0(cm)$
Ch. 1	0.95	0.15	9.94
Ch. 2	0.80	0.15	9.94
Ch. 3	0.55	0.15	9.94
Ch. 4	0.65	0.15	9.94
$\overline{P_{peak}} = 1\text{W}$			

In Figure 4-6 the average power distribution to the four optical channels and the maximum ergodic sum capacity as a function of total expected power for the various channel attenuations are displayed.

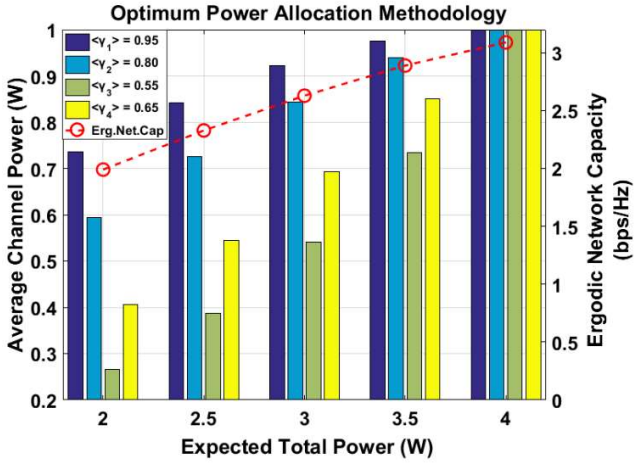

Figure 4-6: Proposed power allocation methodology and ergodic capacity for a 4×4 network versus the expected total power. The sensitivity to channel attenuation is examined.

It is observed that the allocation methodology allows more transmitting power to the less attenuated channels. Here channel 1 has the largest average SNR and transmits the most average power while the mostly attenuated channel 3 transmits the least one. Moreover, the power constraints are held since each channel does not exceed the 1 W limitation and the total channel power does not exceed the expected $\overline{P_{total}}$. At $\overline{P_{total}} = 4$ W all channels transmit 1 W each. The maximum ergodic sum capacity also increases with the total expected power.

The next simulation case concerns the scalability comparison between the proposed algorithm and the EPA and CINVA. We consider all identical channel profiles with $\langle \gamma_i \rangle = 0.6$, $\sigma_{\gamma_i}^2 = 0.2$ and fixed total expected power $\overline{P_{total}} = 5$ W and peak power $\overline{P_{peak}} = 2$ W. In Figure 4-7 the maximum ergodic sum capacity as a function of the number of optical channels is shown.

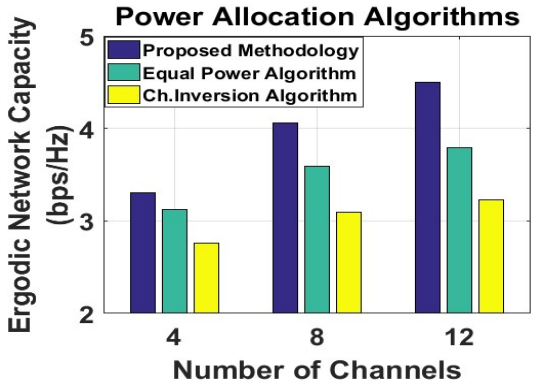

Figure 4-7: Various power allocation policies. The proposed methodology exhibits greater scalability than the others.

It is clear that the proposed algorithm scales considerably better with the number of channels and leverages more efficiently the available total power in contrast with the other methods. The last simulation compares the achievable ergodic sum rate under both weak(lognormal) and strong(gamma-gamma) turbulence as shown in Table 4-3:

Table 4-3: Simulation input parameters

Channels	$\langle \gamma_i \rangle$	$\sigma_{\gamma_i}^2$	$\sigma_{\gamma_i}^2$
Ch. 1	1.0	0.1	1.2
Ch. 2	1.0	0.3	2.0
Ch. 3	1.0	0.5	3.0
Ch. 4	1.0	0.7	5.0
$\overline{P_{peak}} = 1$W			

For small values of expected total power, the maximum ergodic sum rate is larger in the strong turbulence case than in the weak case due to the greater irradiance fluctuations. As the total power increases however the weak scintillation conditions benefit the network's ergodic capacity significantly more than the strong ones (Figure 4-8). Finally, the proposed methodology is compared in terms of performance and spectral efficiency to two

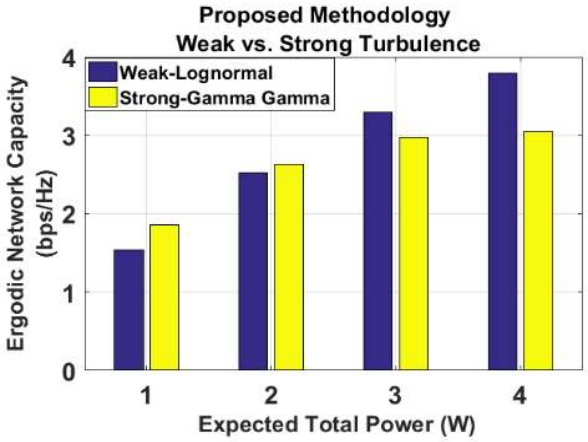

Figure 4-8: Ergodic network capacity for a 4×4 network employing the proposed methodology for weak and strong turbulence conditions.

other power allocation algorithms i.e. the Equal Power Algorithm (EPA) and the Greedy Algorithm (GA). The first one allocates P_{total}/M power in all channels, in all states while the second one is heuristic, fast and practical and allocates peak power to stronger channels while the weaker ones receive the remaining P_{total}. In other words, the Greedy prioritizes the higher gain channels and works in a binary-like way, allocating high or low power. Figure 4-9 and Figure 4-10 depict the achieved overall ergodic capacity versus the total on-board satellite expected power for the three power allocation strategies. In Figure 4-9 we assume that the channels' SNRs are comparable i.e. $|\Delta\gamma_0| \leq 0.5$, $|\Delta SI| \leq 0.2$ while in Figure 4-10 the channels' SNRs are subjected to largely different attenuation and scintillation levels. The maximum differences $|\Delta\gamma_0| \leq 2$, $|\Delta SI| \leq 0.6$ are considered accordingly for all the assumed cases. The final case may occur e.g. when thin clouds appear in some of the slant path optical channels.

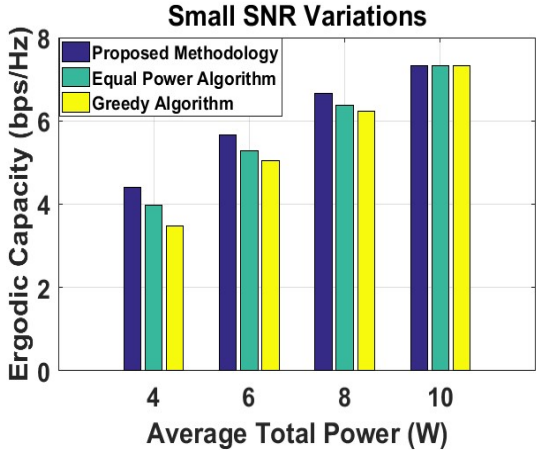

Figure 4-9: Performance comparison of the three power allocation strategies. The channels have small SNR variations. The proposed methodology offers higher capacity than the other ones.

In Figure 4-10, the proposed methodology leverages more efficiently the average total power and achieves much higher desired capacity rates than the other strategies. In this case, the EPA is a moderate solution while the GA is the worst. However, at 10 W the three algorithms perform as one and the same.

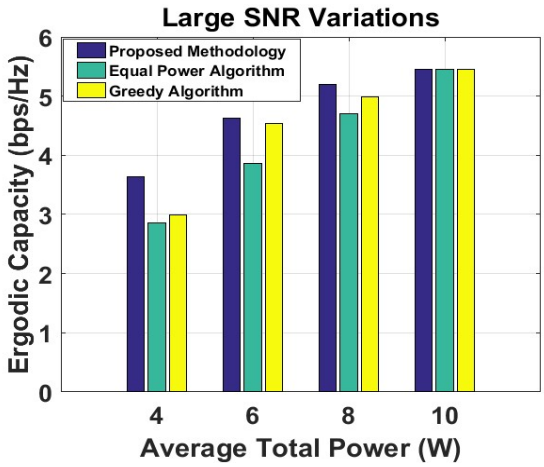

Figure 4-10: Performance comparison of the three power allocation strategies. The channels have greater SNR variations. Proposed methodology offers much higher capacity than the other ones.

In Figure 4-10, the proposed methodology is also shown as the dominant power allocation policy in contrast with the other methods but the GA scales a lot better than the EPA in the presented scenario. As the average total power reaches the 10 W though, the three algorithms perform almost identical.

4.4.2 Proposed methodology for a hybrid fully optical satellite network

In this Section, the proposed methodology is evaluated through numerical simulations for various network topologies and settings and its performance is tested against other known power allocation methods. Specifically, the impact of spatial correlation on the system's capacity is examined as well as the sum rate difference between the proposed allocation scheme and the Even Power Allocation algorithm. Finally, the special case of poor GEO-OGRS channel conditions is considered to investigate the power efficiency of the proposed scheme.

To begin with, the case of a 3x3 optical MIMO is assumed for both GEO-OGRS, OGRS-OGUS links under atmospheric attenuation and weak scintillation conditions. In order to solely examine the impact of correlation, the average irradiance of the channels is normalized to unity while the scintillation index is calculated using the following input parameters: λ=1550 nm, ζ=30°, A_{OGRS}=2000 m, A_{GEO}=35786 km while the Hufnagel-Valley model was

employed for the C_n^2 [5–7]. Furthermore, we assume correlated optical channels on the transmitter side for the GEO-OGRS links i.e., the columns of $\mathbf{H_1}$ are correlated, and on the receiver side for the OGRS-OGUS links i.e., the rows of $\mathbf{H_2}$ are correlated. As an example, the correlation matrix of first row of $\mathbf{H_1}$ is given below:

$$\mathbf{H}_1 = \begin{bmatrix} h_{11} & h_{12} & h_{13} \\ h_{21} & h_{22} & h_{23} \\ h_{31} & h_{32} & h_{33} \end{bmatrix} \xrightarrow[\text{Columns}]{\text{Correlated}} \mathbf{Corr}(\mathbf{H}_1) = \begin{matrix} \\ h_{11} \\ h_{12} \\ h_{13} \end{matrix} \begin{matrix} \begin{matrix} h_{11}^* & h_{12}^* & h_{13}^* \end{matrix} \\ \begin{bmatrix} 1 & \rho & \rho \\ \rho^* & 1 & \rho \\ \rho^* & \rho^* & 1 \end{bmatrix} \end{matrix} \tag{4.47}$$

For the first simulation, the peak transmitting power is fixed at $P_{peak,1} = P_{peak,2} = 1\,\text{W}$ and the system capacity is computed using the proposed methodology for a range of total available powers $P_{total,1} = P_{total,2} = P_{total}$ from 1 W to 3 W and for $\rho = 0,\ 0.5,\ 0.95$. The optical channels are subjected to weak scintillation thus are log-normally distributed and 1000 channel realizations were generated for each simulation run. In Figure 4-11, the system capacity is exhibited as a function of GEO's and OGRS's total power for different channel correlation coefficients.

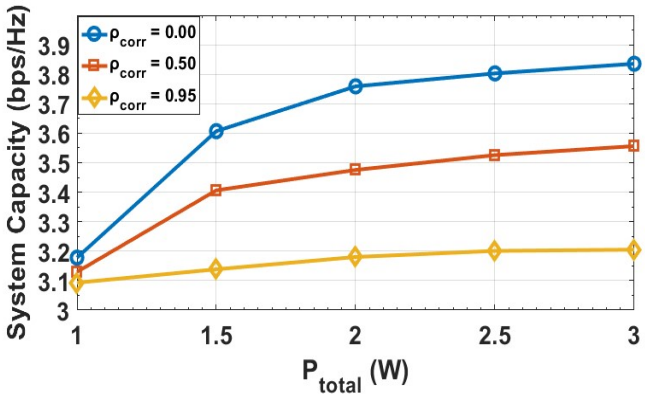

Figure 4-11: System capacity versus the total available power for various channel correlation coefficients. The higher the correlation the lower the network's spectral efficiency.

It is observed that the system capacity increases with the increment of total power. However, the correlated channels are significantly worse for data transmission than the uncorrelated ones since the capacity falls off with higher values of the correlation coefficient. Moreover, as the $\rho_{corr} \to 1$ the system capacity becomes less sensitive to the total available power by only showing a slight increase with larger total power.

Regarding the second simulation, the peak transmitting power is again fixed at $P_{peak,1} = P_{peak,2} = 1\,\text{W}$ and the proposed methodology shall be juxtaposed with the Even Power Allocation (EPA) Algorithm for a range of total available powers $P_{total,1} = P_{total,2} = P_{total}$ from 1

W to 3 W. The EPA algorithm is basically a reference algorithm in order to demonstrate the superiority of the proposed power allocation methodology in terms of bit rate performance.

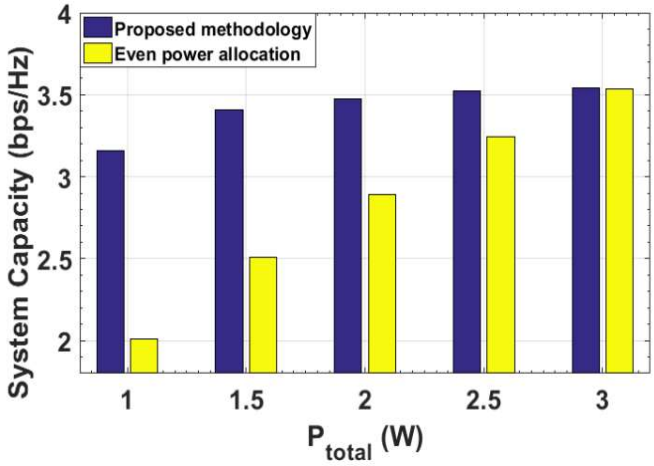

Figure 4-12: Performance comparison between the proposed power allocation methodology and the even power allocation algorithm. The proposed methodology achieves higher data rates over all total power values and outperforms the simpler even allocation.

In Figure 4-12, the performance comparison is depicted. It is clear that the proposed methodology outperforms the EPA algorithm by far, reaching greater data rates. Nevertheless, at 3W the proposed methodology works similarly to the EPA.

For the last simulation, it is assumed that the channel conditions of GEO-OGRS links are of poor quality (high attenuation, scintillation, correlation) and so the GEO transmits with full total available power $P_{total,1} = 3$ W. The proposed methodology is then employed over a range of OGRS's $P_{total,2}$ from 1 W to 3 W and the two sub-system capacities are computed. In Figure 4-13 the two channel capacities are exhibited to show that in this case, the OGRS can utilize 1.25 W total power to obtain the network's maximum power efficiency.

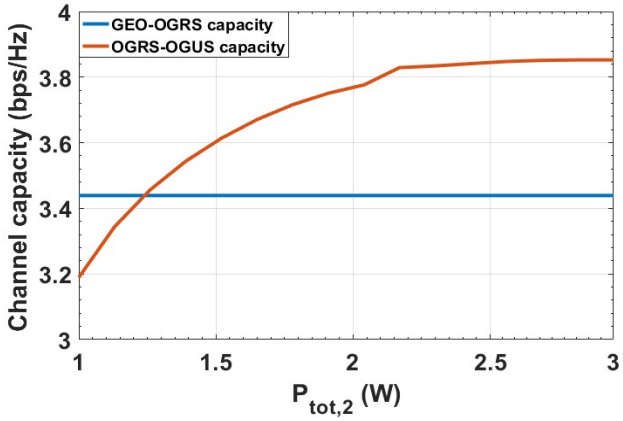

Figure 4-13: Channel capacities of GEO-OGRS, OGRS-OGUS in poor source-relay conditions. The

$P_{total,1} = 3$ W is fixed while the $P_{total,2}$ is sweeped from 1 W to 3 W using the proposed methodology. The OGRS needs no more than 1.25 W to reach the maximum capacity since the network capacity is the minimum of them two.

4.5 Conclusions

In this Chapter, optical satellite communication downlinks with multiple transmitters and multiple receivers have been considered and the optimal power allocation is extensively studied under the total expected power and the peak power constraints. The proposed methodology takes into account the optical attenuation and the turbulence-induced scintillation and derives a formula for the optimal transmitting power in an analogous approach as that of the classic waterfilling algorithm. An iterative, sub-gradient method-based algorithm is also proposed that converges to the maximum network ergodic capacity with great speed. Furthermore, emulation results using actual experimental data from ESA's ARTEMIS missions and simulation results are demonstrated to evaluate the performance of the algorithm and to study the impact of scintillation and atmospheric attenuation. Afterwards, the proposed algorithm is compared to Equal Power, Channel Inversion, and Greedy Algorithms in terms of data rate and scalability with outstanding results.

Finally, hybrid optical satellite links are investigated in a MIMO DF dual hop network formation. A power allocation methodology is then presented and proposed for the optimization of the system's capacity under separate peak and total power constraints. The power allocation problem is initially structured as a convex optimization problem and then solved with the corresponding convexity theory and SVD method whilst taking into account the spatial channel correlation, the atmospheric attenuation and the turbulence strength. Finally, numerical simulations are executed to examine the impact of correlation on system capacity, to evaluate the proposed algorithm's performance through comparison with the EPA algorithm and to give insight to the special case of poor source-relay conditions regarding the system's power efficiency. The derived numerical results are presented and remarks are made validating the proposed methodology in various network topologies and settings.

4.6 Appendix: Proof of the optimal solution

The maximum ergodic capacity is attained when the instantaneous channel capacity is maximum:

$$\arg\max_{P_{t_i}} \log_2(1 + P_{t_i} \cdot \gamma_i) \tag{4.48}$$

s.t. (4.18)

Therefore, for every convex sub-problem in (5.22) we get the Lagrangian:

$$\underset{P_{t_i}\geq 0}{\mathrm{L}(P_{t_i})} = -\log_2(1+P_{t_i}\cdot\gamma_i)+\lambda_i(P_{t_i}-\overline{P_{peak}})+\nu(\sum_{i=1}^{N}\mathrm{E}\left[P_{t_i}\right]-\overline{P_{total}}) \tag{4.49}$$

where λ_i is the Lagrange multiplier related to the $\overline{P_{peak}}$ constraint and ν is the Lagrange multiplier related to the $\overline{P_{total}}$ constraint. The KKT optimality conditions are necessary and sufficient since the problem is convex:

$$0 \leq P_{t_i}^{*} \leq \overline{P_{peak}},\ \sum_{i=1}^{N}\mathrm{E}\left[P_{t_i}^{*}\right] \leq \overline{P_{total}} \tag{4.50}$$

$$\lambda_i \geq 0,\ \nu \geq 0 \tag{4.51}$$

$$\lambda_i(P_{t_i}^{*}-\overline{P_{peak}})=0,\ \nu(\sum_{i=1}^{N}\mathrm{E}\left[P_{t_i}^{*}\right]-\overline{P_{total}})=0 \tag{4.52}$$

$$\underset{P_{t_i}^{*}\geq 0}{\nabla \mathrm{L}(P_{t_i}^{*})} = -\frac{\gamma_i}{1+P_{t_i}^{*}\cdot\gamma_i}+\lambda_i+\nu=0 \tag{4.53}$$

The complementary slackness condition (4.52) yields four cases now:

$$P_{t_i}^{*}-\overline{P_{peak}}=0,\ \sum_{i=1}^{N}\mathrm{E}\left[P_{t_i}^{*}\right]-\overline{P_{total}}=0 \tag{4.54}$$

$$\lambda_i=0,\ \sum_{i=1}^{N}\mathrm{E}\left[P_{t_i}^{*}\right]-\overline{P_{total}}=0 \tag{4.55}$$

$$P_{t_i}^{*}-\overline{P_{peak}}=0,\ \nu=0 \tag{4.56}$$

$$\lambda_i=0,\ \nu=0 \tag{4.57}$$

$$(4.54) \Rightarrow\ P_{t_i}^{*}=\overline{P_{peak}}\ \text{ and }\ \sum_{i=1}^{N}\mathrm{E}\left[P_{t_i}^{*}\right]=\overline{P_{total}}$$

$$(4.53)\ \&\ (4.55) \Rightarrow\ P_{t_i}^{*}=\left(\frac{1}{\nu}-\frac{1}{\gamma_i}\right)^{+}\ \text{ and }\ \sum_{i=1}^{N}\mathrm{E}\left[P_{t_i}^{*}\right]=\overline{P_{total}}$$

Giving the solution:

$$P_{t_i}^{*}=\min\left\{\overline{P_{peak}},\max\left\{\frac{1}{\nu}-\frac{1}{\gamma_i},0\right\}\right\} \tag{4.58}$$

Finally, the integration bounds in (4.22) and (4.23) are computed as shown:

$0 \le P_{t_i}^* \le \overline{P_{peak}} \Leftrightarrow 0 \le \frac{1}{\nu} - \frac{1}{\gamma_i} \le \overline{P_{peak}} \Leftrightarrow \nu \le \gamma_i \le \frac{\nu}{1-\nu\overline{P_{peak}}}$ while for $\gamma_i \le \nu \Rightarrow P_{t_i}^* = 0$ and for $\gamma_i \ge \frac{\nu}{1-\nu\overline{P_{peak}}} \Rightarrow P_{t_i}^* = \overline{P_{peak}}$ because the transmitted power $P_{t_i}^*$ cannot be negative and cannot exceed the peak power either.

Chapter References

[1] Liolis, K., Geurtz, A., & Sperber, R., et al. (2019). Use cases and scenarios of 5G integrated satellite-terrestrial networks for enhanced mobile broadband: The SaT5G approach. *International Journal of Satellite Communications, 37*(2), 91–112.

[2] Sharma, S. K., Chatzinotas, S., & Arapoglou, P. D. (2018). *Satellite communications in the 5G era*. London: The Institution of Engineering and Technology.

[3] J. Rodriguez, "Fundamentals of 5G Mobile Networks", Hoboken, NJ, USA: Wiley, 2015.

[4] Jaber, M., Imran, M. A., Tafazolli, R., et al. (2016). 5G backhaul challenges and emerging research directions: A survey. *IEEE Access, 4*, 1743–1766.

[5] Hemmati, H. (2009). *Near-earth laser communications*. Boca Raton: CRC Press.

[6] Kaushal, H., & Kaddoum, G. (2016). Optical communication in space: Challenges and mitigation techniques. *IEEE Communications Surveys & Tutorials, 19*, 57–96.
[7] Andrews, L., & Phillips, R. (2005). *Laser beam propagation through random media*. Bellingham, WA: SPIE Press.
[8] Lyras, N. K., Kourogiorgas, C. I., & Panagopoulos, A. D. (2017). Cloud attenuation statistics prediction from ka-band to optical frequencies: Integrated liquid water content field synthesizer. *IEEE Transactions on Antennas and Propagation, 65*, 319–328.
[9] Lyras, N. K., Kourogiorgas, C. I., & Panagopoulos, A. D. (2017). Cloud free line of sight prediction modelling for optical satellite communication network. *IEEE Communications Letters, 21*, 1537–1540.
[10] Lyras, N. K., Efrem, C. N., Kourogiorgas, C. I., & Panagopoulos, A. D. (2019). Medium earth orbit optical satellite communication networks: Ground terminals selection optimization based on the cloudfree line-of-sight statistics. *International Journal of Satellite Communications, 37*(4), 370–384.
[11] Lyras, N. K., Efrem, C. N., Kourogiorgas, C. I., Panagopoulos, A. D., & Arapoglou, P. (2020). Optimizing the ground network of optical meo satellite communication systems. *IEEE Systems Journal*.
[12] Scutari, G., Palomar, D. P., & Barbarossa, S. (2009). The MIMO iterative waterfilling algorithm. *IEEE Transactions on Signal Processing, 57*(5), 1917–1935.
[13] Fitzek, F. H., & Katz, M. D., "Cooperation in wireless networks: principles and applications," New York: Springer (2006).
[14] Lu, F., Liu, C., Fu, Y., & Zhao, H. A., "Joint Power Allocation for DF MIMO Relay Links with Hybrid Power Constraints," in IEEE 8th International Conference on Wireless Communications, Networking and Mobile Computing, 1-4 (2012).
[15] Hammerstrom, I., & Wittneben, A., "Power allocation schemes for amplify-and-forward MIMO-OFDM relay links," in IEEE Transactions on Wireless Communications, 6(8), 2798-2802 (2007).
[16] Boyd, S., & Vandenberghe, L. (2004). *Convex optimization*. Cambridge: Cambridge University Press.
[17] Bertsekas, D. P. (1982). *Constrained optimization and lagrange multiplier methods*. New York: Academic Press.
[18] Kapsis, T. T., Lyras, N. K., & Panagopoulos, A. D. (2019). Long term irradiance statistics for optical geo downlinks: Validation with artemis experimental measurements. *Progress In Electromagnetics Research, 82*, 89–94.
[19] Kapsis, T. T., Lyras, N. K., Kourogiorgas, C. I., & Panagopoulos, A. D. (2019). Time series irradiance synthesizer for optical geo satellite downlinks in 5g networks. *Future Internet, 11*(6), 131.
[20] Kolev, D. R., & Toyoshima, M. (2017). Satellite-to-ground optical communications using small optical transponder (SOTA): Received-power fluctuations. *Optics Express, 25*(23), 28319–28329.
[21] Yeaseen, M. H., Azam, F., Saha, S., & Islam, A. K. M. (2015). Free-space optical communication with BPSK subcarrier intensity modulation in presence of atmospheric turbulence and pointing error. In *18th International conference on computer and information technology, ICCIT*, Dhaka, pp. 516–521.
[22] T. V. Pham, T. C. Thang and A. T. Pham, "Average achievable rate of spatial diversity MIMO-FSO over correlated Gamma–Gamma fading channels," IEEE/OSA Journal of Optical Communications and Networking, 10(8), 662-674 (2018).
[23] Chen, Z., Yu, S., Wang, T., Wu, G., Wang, S., & Gu, W., "Channel correlation in aperture receiver diversity systems for free-space optical communication," Journal of Optics, 14(12), 125710 (2012).

[24] Goldsmith, A. J., & Varaiya, P. P. (1997). Capacity of fading channels with channel side information. *IEEE Transactions on Information Theory, 43*(6), 1986–1992.
[25] Nistazakis, H. E., Karagianni, E. A., Tsigopoulos, A. D., Fafalios, M. E., & Tombras, G. S. (2009). Average capacity of optical wireless communication systems over atmospheric turbulence channels. *Journal of Lightwave Technology, 27*(8), 974–979.
[26] Nistazakis, H. E., Tsiftsis, T. A., & Tombras, G. S. (2009). Performance analysis of free space optical communication systems over atmospheric turbulence channels. *IET Communications, 3*(8), 1402–1409.
[27] Dabiri, M. T., Saber, M. J., & Sadough, S. M. S. (2017). On the performance of multiplexing FSO MIMO links in log-normal fading with pointing errors. *Journal of Optical Communications and Networking, 9*(11), 974–983.
[28] Gao, Z., Eisen, M., & Ribeiro, A. (2019). Optimal WDM power allocation via deep learning for radio on free space optics systems. In *IEEE global communications conference (GLOBECOM)* (pp. 1–6). Waikoloa, HI.
[29] Zhou, H., Mao, S., & Agrawal, P. (2015). Optical power allocation for adaptive transmissions in wavelength-division multiplexing free space optical networks. *Digital Communication Network, 1*, 171–180.
[30] An, K., Liang, T., Yan, X., Li, Y., & Qiao, X. (2018). Power allocation in land mobile satellite systems: An energy-efficient perspective. *IEEE Communications Letters, 22*(7), 1374–1377.
[31] Süli, E., & Mayers, D. (2003). *An introduction to numerical analysis*. Cambridge: Cambridge University Press.
[32] Bertsekas, D. P. (1999). *Nonlinear programming*. Belmont: Athena Scientific.
[33] Kotchasarn, C. (2008). Joint power allocation for multi-user uplink mimo transmissions with imperfect CSI. In *International symposium on communications and information technologies*, Lao (pp. 121–125).
[34] Toyoshima, M., et al. (2005). Long-term statistics of laser beam propagation in an optical ground-to-geostationary satellite communications link. *IEEE Transactions on Antennas and Propagation, 53*(2), 842–850.
[35] Dios, F., et al. (2004). Scintillation and beam-wander analysis in an optical ground station satellite uplink. *Applied Optics, 43*(19), 3866–3873.
[36] Barrios, R. (2020). Fading loss for earth-to-space lasercom affected by scintillation and beam wander composite channel. *Optical Engineering, 59*(5), 056103.

Chapter 5
Power Allocation for Reliable and Energy-Efficient Optical LEO-to-Ground Downlinks with Hybrid ARQ Schemes[6]

Satellites in low earth orbit (LEO) are currently being deployed for numerous communication, positioning, space and Earth-imaging missions. To provide higher data rates in direct-to-user links and earth observation downlinks, the free-space optics technology can

be employed for LEO-to-ground downlinks. Moreover, the hybrid automatic repeat request (HARQ) can be adopted since the propagation latency is low for LEO satellites. In this work, a power allocation methodology is proposed for optical LEO-to ground downlinks under weak turbulence employing HARQ retransmission schemes. Specifically, the average power consumption is minimized given a maximum transmitted power constraint and a target outage probability threshold to ensure energy efficiency and reliability, respectively. The optimization problem is formulated as a constrained nonlinear programming problem and solved for Type I HARQ, chase combining (CC) and incremental redundancy (IR) schemes. The solutions are derived numerically via iterative algorithms, namely interior-point (IP) and sequential quadratic programming (SQP), and validated through an exhaustive (brute-force) search. The numerical simulations provide insight into the performance of the retransmission schemes regarding average power. More specifically, Type I HARQ has the worst output, CC has a moderate one, and IR exhibits the best performance. Finally, the IP algorithm is a slower but more accurate solver, and SQP is faster but slightly less accurate.

[6]

5.1 Introduction

As early as the 1960s, the development of optical and laser pumping brought free-space optical (FSO) communication to life [1–2]. Since then, FSO has been employed throughout the industry either for space telecommunication applications such as the modern SpaceX Starlink project for satellite interconnection, optical satellite feeder links and even terrestrial commercial and military applications, e.g., inter-building links [1]. The rollout of the fifth generation (5G) and beyond has especially shifted the research paradigm to optical frequency technologies in order to meet the strict broadband, reliability and latency requirements, leading to the massive installation of fibre optics and optical telescopes [2]. Albeit a relatively new field of communication, FSO systems are considered mature enough to be employed as

they hold many noteworthy advantages. More specifically, it is easy to establish point-to-point optical links due to the small-size equipment, lack of any digging, huge bandwidth availability and data rates, unlicensed operation, their strong immunity to unwanted interferences, low-power to ensure eye-safety and improved security due to employment of narrow beams [1–3]. Therefore, assuming good optical signal propagation conditions (clear sky), FSO links guarantee fast, convenient, economic, secure and reliable deployment as well as the efficient usage of the spectrum [1–3].

On the other hand, in the case of atmospheric impairments such as opaque fog and clouds or line-of-sight interruption in general, the irradiance losses can reach hundreds of dBs, leading to an optical link outage [1–3]. Moreover, the atmospheric refractive index is not spatially or temporally homogeneous but is varied with wind speed, temperature and wavelengths, which subsequently cause atmospheric turbulence [2–4]. The turbulence in turn influences the slant path propagation, causing scintillation of the received irradiance and beam spreading [2–4]. There are also many more sources of deterioration such as pointing jitter and background noise, but these are beyond the scope of this Chapter [4]. Typical mitigation techniques regarding the physical layer include aperture averaging, adaptive optics, hybrid radio frequency (RF)/FSO and spatial diversity, but there are also upper-layer solutions such as automatic repeat request (ARQ) retransmission schemes [3–4].

In particular, hybrid ARQ (HARQ) combines error detection with error correction by adding redundancy bits to the transmitted frames, and if the message decoding fails, a series of retransmission rounds are performed [5–8]. Depending on whether the erroneous message is discarded or stored, the HARQ is categorized as Type I HARQ or soft combining HARQ, respectively [5–8]. The latter is performed in practice based on the following two methods: Chase combining (CC), in which the transmitter sends identical copies of the corrupted frame on each round and the receiver employs maximal ratio combining, whereas in incremental redundancy (IR) the transmitter sends more parity bits on each round, increasing the successful decoding probability [5–8]. The HARQ is superior when reliability and link adaptation are required due to the joint error detection and correction, while costwise it is potentially cheaper. HARQ for optical links has shown good performance and can operate in parallel with the aforementioned physical layer techniques [3]. A low Earth orbit (LEO) satellite operates at an altitude less than 2000 km, has a full period of about two hours and exhibits a latency of a few milliseconds (17 times lower than GEO) [2]. If equipped with an optical transmitter it can provide high-definition data at reduced latency. Several optical LEO-to-ground experiments have been conducted to study the feasibility and obtain measurements

for channel characterization and modelling [2,9,10]. In [6] a new HARQ protocol for FSO multi-user systems is proposed, and in [8,11,12] a performance analysis of FSO HARQ systems and estimations of the packet error probability are derived. In [13–15] power allocation strategies for RF HARQ links under Rayleigh fading are reported. The LEO satellite-to-ground links are also used for quantum key distribution (QKD). LEO-to-ground QKD links have also very recently been demonstrated to reach distances up to 1200 km and key rates up to kbps [16]. The key rate is the exchange rate of polarized photons (encryption keys) over an optical fibre or FSO link. Moreover, a study has been evaluated for QKD performance on a hypothetical constellation with ten satellites in sun-synchronous LEOs that are assumed to communicate over a period of one year with an optical infrastructure (three optical ground stations) located in Greece [17]. The atmospheric effects of turbulence and the background solar radiance have been considered [17].

For optical satellite downlinks with HARQ schemes under weak turbulence, there has not been a power allocation investigation in the literature. In this Chapter, a power allocation methodology is proposed for optical LEO-to-ground downlinks under weak scintillation conditions employing HARQ retransmission schemes. The contributions of this Chapter are summarized as follows:

i. Three power allocation methodologies based on the Type I HARQ, CC and IR schemes are proposed, and their performances are compared and ranked from best to worst in terms of the average power consumption.
ii. The energy efficiency and the reliability of the optical links are optimized by formulating the optimization problem as a constrained nonlinear programming problem with an objective function, the average power usage, constraints, the maximum transmitted power and a target outage probability accordingly.
iii. Only the channel statistics (long-term channel state information) are required to obtain the optimal power allocation strategy and not the instantaneous channel states.
iv. The proposed solutions are derived numerically via iterative algorithms, namely interior point and sequential quadratic programming, and validated through an exhaustive or brute force search [18–19].
v. Simulations are executed for various channel conditions and system settings by simulating a LEO passing over various turbulence intensities and ground weather conditions to investigate the sensitivity of the three HARQ schemes to weak scintillation, path loss and target outage probability. Novel numerical results are reported and commented on.

The remainder of the Chapter is structured as follows: In Section 5.2 the LEO-to-ground system model is given along with the necessary FSO theory and assumptions regarding the weak fluctuation model. In Section 5.3 the optimal power allocation problem under maximum power and outage probability constraints is developed by taking into account the three HARQ schemes, and the proposed solutions are reported. In Section 5.4 simulations of various scintillation, weather conditions and constraints are obtained using the proposed methodology, and numerical results are derived, compared and commented on. Finally, Section 5.5 concludes this Chapter.

5.2 System Model

A single, cloud-free optical LEO-to-ground communication downlink is considered subject to path losses and weak atmospheric turbulence. The optical channel is generally dynamic due to the elevation angle–varying link distance and the LEO satellite's slew rate, thus leading to temporal signal fluctuations known as scintillation [2,9]. For the transmission, the intensity modulation with on-off-keying (OOK) is assumed, and direct detection is used for the reception. It is also hypothesized that a negative acknowledgment (NACK) or no acknowledgment at all to a particular frame transmission by the receiving terminal will initiate a series of retransmissions via an HARQ protocol [5–8]. The maximum number of HARQ rounds is predefined and equal to *M.* During these *M* rounds, the receiver either successfully decodes the message and responds with a positive acknowledgment (ACK) or fails to decode it, and the re-transmission stops. In order to achieve independent fading states, the minimum retransmission time between rounds must be equal to the coherence time τ_0 (sec) of the optical channel. According to the weak turbulence model the coherence time is given by [9–10]:

$$\tau_0 = \left(118\lambda^{-2} \sec\left(90° - e\right) \int_{H_{OGS}}^{H_{LEO}} C_n^2(\mathrm{z}) V^{5/3}(\mathrm{z}) \mathrm{dz} \right)^{-3/5}, \tag{5.1}$$

where $\lambda(m)$ is the communication wavelength, sec(x) is the secant function, $e(deg)$ is the elevation angle, $H_{\mathrm{OGS}}(m)$, $H_{\mathrm{LEO}}(m)$ are the altitudes of the optical ground station (OGS) and LEO satellite, $C_n^2(z)$ is the refractive index structure parameter usually given by the Hufnagel–Valley model, $z(m)$ is the altitude, and $V(z)(m/s)$ is the wind speed (vertical path) usually described by the Bufton model. Therefore, for transmission periods greater

than τ_0 the fading states can be considered uncorrelated. In Figure 5-1, the system model is depicted.

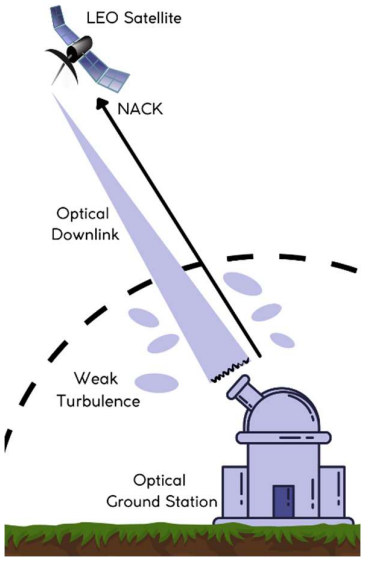

Figure 5-1: Optical LEO-to-ground downlink. The atmospheric turbulence attenuates the signal, distorts the wavefront and induces scintillation.

Weak turbulence is often represented by the lognormal (LN) distribution, which fits well and exhibits good agreement with first-order statistics from experimental data [2,20]. The *LN* model does not fully apply only for elevation angles < 20°, and the reason is the saturation of scintillation [2]. The normalized received irradiance $I\left(W/m^2\right)$ is an *LN* random variable according to the following probability density function (PDF) [4,20]:

$$p(I)=\frac{1}{I\sqrt{2\pi}\sigma_I}\exp\left\{-\frac{\left[\ln\left(I/\langle I\rangle\right)+0.5\sigma_I^2\right]^2}{2\sigma_I^2}\right\}, \tag{5.2}$$

where $\langle I\rangle$ is the average irradiance, and σ_I^2 is the so-called scintillation index (SI). A theoretical expression for SI in the case of weak turbulence (SI < 0.5) and point receivers is derived from Rytov, which is expressed by the formula [9,20]:

$$\sigma_I^2=2.25k^{\frac{7}{6}}\sec^{\frac{11}{6}}\left(90°-e\right)\int_{H_{OGS}}^{H_{LEO}}C_n^2\left(\mathrm{z}\right)\left(\mathrm{z}-H_{OGS}\right)^{\frac{5}{6}}\mathrm{dz}\,, \tag{5.3}$$

where $k(rad/m)$ is the wavenumber, $e(deg)$ is the elevation angle, and the rest of the parameters are defined as in (5.1). The Kolmogorov spectrum is assumed, and it is also assumed that the optical wavefront is approximated by a plane wave far from the source. For

moderate (SI~0.5) or strong turbulence (SI~1), other distributions such as gamma– gamma are more suitable [2]. If experimental data are to be employed then SI is simply the normalized variance of *I*: $\sigma_I^2 = \langle I^2 \rangle / \langle I \rangle^2 - 1$ [9,20].

The optical channel for the downlink follows the *LN* distribution considering weak scintillation conditions. By incorporating the quantum efficiencies of the transmitter η_{LEO} and receiver η_{OGS}, the atmospheric transmittance T_{Atm}, the gains of transmitter g_{LEO} and receiver g_{OGS}, the large-scale path loss PL, the small-scale loss due to scintillation e^{2X_s} where X_s is the log-amplitude of the optical wave and hence Gaussian (normally) distributed, the optical channel is expressed by [4,21]:

$$h_{opt} = \eta_{LEO}\eta_{OGS}T_{Atm}g_{LEO}g_{OGS}PL\ e^{2X_s} \tag{5.4}$$

Additionally, therefore, the signal-to-noise ratio (SNR) is given by [4,21]:

$$SNR = \frac{P_T\ \eta_{LEO}\eta_{OGS}T_{Atm}g_{LEO}g_{OGS}PL\ e^{2X_s}}{\sigma_{n_{opt}}^2} = \frac{P_T\ h_{opt}}{\sigma_{n_{opt}}^2} = P_T\ h \tag{5.5}$$

where P_T is the transmitted power, $\sigma_{n_{opt}}^2$ is the signal-independent optical noise variance, and $h\left[Watts^{-1}\right]$ represents the ratio $h_{opt}/\sigma_{n_{opt}}^2$.

In particular, the optical noise is a zero mean, a constant variance random variable that describes the environmental optical interference. It incorporates the background radiation from the various celestial bodies, the amplified spontaneous emission (ASE) from optical preamplifiers and the electronic detection noise [4,21]. By using narrow passband optical filters and small field-of-view telescopes the receiver can eliminate the ambient background radiation and ASE, while the thermal and shot noises can be considered as additive white Gaussian noise [2]. Now, for a fixed $\sigma_{n_{opt}}^2$ it is easy to see that *h* is also a *LN* variable, and its PDF is derived from (5.2) with parameters $\langle h \rangle$, $\sigma_h^2 = \sigma_I^2$.

5.3 Power Allocation Problem and Methodology

In this subsection, the power allocation problem for an HARQ optical LEO-to-OGS downlink is formulated under a maximum transmitted power constraint and a guaranteed outage probability constraint. Specifically, assuming *M* rounds of retransmissions via Type I, CC, IR HARQ schemes the optimization problem considers the minimization of the average total transmitted power:

$$\arg\min_{P_1,P_2,...,P_M} P_{Avg} \tag{5.6}$$

$$\begin{aligned} s.t.\ \ & 0 \le P_m \le \overline{P},\ \text{for} 1 \le m \le M \\ & 0 \le P_{out,M}\left(C_{out}\right) \le \varepsilon_{\text{target}}\ , \end{aligned} \tag{5.7}$$

where $P_i\,(i=1,..,M)$ is the transmitted power at each round, $\overline{P}$ is the peak transmitted power, C_{out} is the defined outage capacity, $P_{out,M}$ is the decoding failure probability after all the M re-transmissions, and $\varepsilon_{\text{target}}$ is the target outage probability. The $P_{out,m}$ is analyzed below for the three HARQ schemes individually.

The P_{Avg} for all three investigated HARQ schemes is reported as follows [13–15]:

$$P_{Avg} = P_1 + P_2 \cdot P_{out,1} + ... + P_M \cdot P_{out,M-1} = \sum_{m=1}^{M} P_m \cdot P_{out,m-1} \tag{5.8}$$

Note that $P_{out,0} = 1$ because no transmission is achieved at round m = 0. Successful decoding occurs when the channel capacity on the mth round $C_m > C_{out}$; otherwise, a re-transmission is requested [13–14]. After M failures, the buffer empties, and the source proceeds to the next packet. In our analysis, the bit error rate (BER) is not included in (5.7) because it is complex and requires specific knowledge of coding and modulation. The BER performance for a variety of binary modulations can be found in [12].

In a Type I HARQ scheme, the received packets are not buffered but discarded on each round. Thus, after the mth round the channel capacity and outage probability are [5,15]:

$$C_m = W\log_2\left(1+h_m P_m\right)\left(bps\right) \tag{5.9}$$

$$P_r\left(C_m \le C_{out}\right) = P_r\left(h_m \le \frac{2^{\frac{C_{out}}{W}}-1}{P_m}\right) = \frac{1}{2}\text{erfc}\left(-\frac{\ln\left(\frac{2^{\frac{C_{out}}{W}}-1}{\langle h_m\rangle P_m}\right)+0.5\sigma_h^2}{\sigma_h\sqrt{2}}\right) \tag{5.10}$$

$$P_{out,m} = P_r\left(C_1 \le C_{out},...,C_m \le C_{out}\right) = \prod_{i=1}^{m} P_r\left(C_i \le C_{out}\right), \tag{5.11}$$

where W is the allocated bandwidth, and erfc(x) is the complementary error function.

For example, in the case of M=3 rounds then the optimization problem is the following:

$$\underset{P_1,P_2,P_3}{\arg\min}\ P_1+P_2\cdot\frac{1}{2}\operatorname{erfc}\left(-\frac{\ln\left(\frac{2^{C_{out}/W}-1}{\langle h_1\rangle P_1}\right)+0.5\sigma_{h_1}^2}{\sigma_{h_1}\sqrt{2}}\right)+P_3\cdot\frac{1}{4}\operatorname{erfc}\left(-\frac{\ln\left(\frac{2^{C_{out}/W}-1}{\langle h_1\rangle P_1}\right)+0.5\sigma_{h_1}^2}{\sigma_{h_1}\sqrt{2}}\right)\cdot\operatorname{erfc}\left(-\frac{\ln\left(\frac{2^{C_{out}/W}-1}{\langle h_2\rangle P_2}\right)+0.5\sigma_{h_2}^2}{\sigma_{h_2}\sqrt{2}}\right) \tag{5.12}$$

$$P_{out,3}=\frac{1}{8}\operatorname{erfc}\left(-\frac{\ln\left(\frac{2^{\frac{C_{out}}{W}}-1}{\langle h_1\rangle P_1}\right)+0.5\sigma_{h_1}^2}{\sigma_{h_1}\sqrt{2}}\right)\cdot\operatorname{erfc}\left(-\frac{\ln\left(\frac{2^{\frac{C_{out}}{W}}-1}{\langle h_2\rangle P_2}\right)+0.5\sigma_{h_2}^2}{\sigma_{h_2}\sqrt{2}}\right)\cdot\operatorname{erfc}\left(-\frac{\ln\left(\frac{2^{\frac{C_{out}}{W}}-1}{\langle h_3\rangle P_3}\right)+0.5\sigma_{h_3}^2}{\sigma_{h_3}\sqrt{2}}\right) \tag{5.13}$$

In a CC scheme, the received packets are buffered and MRC-combined on each round. Thus, after the *m*th round the channel capacity and outage probability are [5,14]:

$$C_m=W\log_2\left(1+\sum_{i=1}^{m}h_iP_i\right)(bps) \tag{5.14}$$

$$P_r\left(C_m\le C_{out}\right)=P_r\left(W\log_2\left(1+\sum_{i=1}^{m}h_iP_i\right)\le C_{out}\right)=P_r\left(h_1P_1+\ldots+h_mP_m\le 2^{\frac{C_{out}}{W}}-1\right) \tag{5.15}$$

$$P_{out,m}=P_r\left(C_1\le C_{out},\ldots,C_m\le C_{out}\right)=P_r\left(C_m\le C_{out}\right) \tag{5.16}$$

For example, in the case of $M = 3$ rounds then the optimization problem is the following:

$$\underset{P_1,P_2,P_3}{\arg\min}\ P_1+P_2\cdot\frac{1}{2}\operatorname{erfc}\left(-\frac{\ln\left(\frac{2^{C_{out}/W}-1}{\langle h_1\rangle P_1}\right)+0.5\sigma_{h_1}^2}{\sigma_{h_1}\sqrt{2}}\right)+P_3\cdot P_r\left(h_1P_1+h_2P_2\le 2^{C_{out}/W}-1\right) \tag{5.17}$$

$$P_{out,3}=\int_{h_1=0}^{\frac{2^{C_{out}/W}-1}{P_1}}\int_{h_2=0}^{\frac{2^{C_{out}/W}-1-h_1P_1}{P_2}}\int_{h_3=0}^{\frac{2^{C_{out}/W}-1-h_2P_2-h_1P_1}{P_3}}\frac{1}{h_1h_2h_3\sigma_{h_1}\sigma_{h_2}\sigma_{h_3}\sqrt[3]{2\pi}}e^{\left(-K(h)\right)}dh_1dh_2dh_3 \tag{5.18}$$

where:

$$\mathrm{K}(h)=\frac{\left(\ln h_1/\langle h_1\rangle+0.5\sigma_{h_1}^2\right)^2}{2\sigma_{h_1}^2}+\frac{\left(\ln h_2/\langle h_2\rangle+0.5\sigma_{h_2}^2\right)^2}{2\sigma_{h_2}^2}+\frac{\left(\ln h_3/\langle h_3\rangle+0.5\sigma_{h_3}^2\right)^2}{2\sigma_{h_3}^2} \tag{5.19}$$

In an IR scheme, the received packets are buffered, and the information is added on each round because the packets contain new parity bits. Thus, after the *m*th round the channel capacity and outage probability are [5,13]:

$$C_m=\sum_{i=1}^{m}W\log_2\left(1+h_iP_i\right)\left(bps\right) \tag{5.20}$$

$$P_r\left(C_m\le C_{out}\right)\Rightarrow P_r\left(\sum_{i=1}^{m}W\log_2\left(1+h_iP_i\right)\le C_{out}\right)\Rightarrow P_r\left(\left(1+h_1P_1\right)\cdots\left(1+h_mP_m\right)\le 2^{\frac{C_{out}}{W}}\right) \tag{5.21}$$

$$P_{out,m}=P_r\left(C_1\le C_{out},...,C_m\le C_{out}\right)=P_r\left(C_m\le C_{out}\right) \tag{5.22}$$

For example, in the case of $M = 3$ rounds then the optimization problem is the following:

$$\underset{P_1,P_2,P_3}{\arg\min}\ P_1+P_2\cdot\frac{1}{2}\mathrm{erfc}\left(-\frac{\ln\left(\frac{2^{C_{out}/W}-1}{\langle h_1\rangle P_1}\right)+0.5\sigma_{h_1}^2}{\sigma_{h_1}\sqrt{2}}\right)+P_3\cdot P_r\left(\left(1+h_1P_1\right)\left(1+h_2P_2\right)\le 2^{C_{out}/W}\right) \tag{5.23}$$

$$P_{out,3}=\int_{h_1=0}^{\frac{2^{C_{out}/W}-1}{P_1}}\int_{h_2=0}^{\frac{2^{C_{out}/W}}{P_2\left(1+h_1P_1\right)}-\frac{1}{P_2}}\int_{h_3=0}^{\frac{2^{C_{out}/W}}{P_3\left(1+h_2P_2+h_1P_1+h_1P_1h_2P_2\right)}-\frac{1}{P_3}}\frac{1}{h_1h_2h_3\sigma_{h_1}\sigma_{h_2}\sigma_{h_3}\sqrt[3]{2\pi}}\mathrm{e}^{\left(-\mathrm{K}(h)\right)}\mathrm{dh}_1\mathrm{dh}_2\mathrm{dh}_3 \tag{5.24}$$

where K(h) is defined in (5.19).

The (5.16) and (5.22) are based on the fact that in chase combining and incremental redundancy, the channel capacity C_m at the end of *m*th round is *non-decreasing* for all fading-sequence realizations because the packets are soft-combined [13–14]. That is: $C_1\le C_2\le...\le C_m$. Therefore, if $C_m\le C_{out}$ it means that all the previous rounds' capacities are also less than C_{out}.

The outage probabilities in (5.18) and (5.24) are intractable and cannot be solved in closed-form, but even numerical computations are challenging for a large *M*. In this Chapter we will investigate the scenario with $M = 3$ rounds of re-transmission.

From the aforementioned analysis in Section 5.3, it was observed that both the objective function and the constraints are non-linear and non-convex. The finding of a global minimum

is then NP-hard because it may exist in many feasible regions and many local minima, so a global solution is very difficult to obtain. However, according to the Weierstrass theorem, if the objective function is continuous and the feasible region is closed and bounded, then there exists a global optimum [18–19]. All three HARQ power allocation subproblems satisfy these requirements, and the constraints can be plotted to determine if the feasible region is closed and bounded. The global minimum can always be found then with an exhaustive/brute-force search [13].

In spite of the lack of convexity, the Karush–Kuhn–Tucker conditions are necessary (but not sufficient) for P^* to be an optimum solution to the problem. Specifically, for M = 3 rounds and the Lagrangian $\mathrm{L}(P_1^*, P_2^*, P_3^*, \lambda^*)$ [19]:

Stationarity:

$$\frac{\partial \mathrm{L}(P_1^*, P_2^*, P_3^*, \lambda^*)}{\partial P_1^*} = \frac{\partial \mathrm{L}(P_1^*, P_2^*, P_3^*, \lambda^*)}{\partial P_2^*} = \frac{\partial \mathrm{L}(P_1^*, P_2^*, P_3^*, \lambda^*)}{\partial P_3^*} = 0 \tag{5.25}$$

Primal feasibility:

$$0 \le P_1^*, P_2^*, P_3^* \le \overline{P}\ ,\ 0 \le P_r\left(C_3 \le C_{out}\right) \le \varepsilon_{\text{target}} \tag{5.26}$$

Complementary slackness:

$$\lambda^* \cdot \left(P_r\left(C_3 \le C_{out}\right) - \varepsilon_{\text{target}}\right) = 0 \tag{5.27}$$

Dual feasibility:

$$\lambda^* \ge 0 \tag{5.28}$$

where $\varepsilon_{\text{target}}$ is the target outage probability from (5.7).

Besides the brute-force or exhaustive search, the standard methods for solving constrained non-linear optimization problems include interior-point (IP) methods, sequential quadratic programming (SQP) or even projected gradient descent (PGD) [18]. IP and SQP require the objective and constraint functions to be twice differentiable and exhibit polynomial time complexity for linear and non-linear problems, but the strong advantage of SQP lies in its property that the initial guess and the iteration steps do not need to be feasible points [18]. SQP is an active-set method that works in two stages: Firstly, the objective function is neglected, and a feasible point is obtained that satisfies the constraints. Secondly, the objective function is optimized while keeping the feasibility. In contrast, the IP iterations must stay inside the feasible region and avoid the infeasible region, but it yields better approximations, and it is scalable [18].

5.4 Numerical Results and Discussion

In this section, the optimal power allocation problem for an optical LEO-to-ground downlink with HARQ schemes is solved, and a variety of simulations are carried out from which conclusive results are drawn. In our Chapter, the MATLAB software is employed to numerically obtain a very good approximation of the global minimum of the constrained non-linear optimization problems. Specifically, the IP and SQP methods are employed, and the outcomes are validated through a brute-force search. Moreover, the average power is minimized for Type I, CC, IR HARQ schemes, and the sensitivity to the scintillation index, average path loss and target outage probability is examined. It must be clarified that we are more focused on the proposed allocation methodologies and less on the transmission characteristics.

A M = 3 rounds HARQ protocol is considered, and an optical LEO-to-ground link is assumed under atmospheric path loss and weak scintillation conditions. The choice of M = 3 is supported by the fact that LEO satellites have a short contact time (~5 min); therefore, it is realistic to assume a few HARQ rounds. The wavelength is set to λ=1550 nm, the slew rate w_s = 0.001, the altitudes H_{OGS} = 2000 m and $H_{\mathrm{LEO}} = H_{\mathrm{turb}}$ = 20 km and elevation angle e = 50° while the ground weather conditions, i.e., wind speed, $C_n^2(z)$, were varied to obtain the scintillation indices and the corresponding coherence times using the (5.1). The Bufton and Hufnagel–Valley models were employed for the wind and $C_n^2(z)$. From Table 5-1 it is implied that the worse the scintillation effects the less coherence time is needed because the channel fluctuations are greater and rapid. Finally, the maximum transmitted power is set to $\overline{P} = 1$ W for all simulations.

Table 5-1: Scintillation index versus the channel coherence time for various weather conditions.

SI	**τ_0 (ms)**
0.1	5.2
0.2	1.8
0.3	1.2
0.4	0.9
0.5	0.8

Table 5-2: First simulation's input parameters for the optical channels.

$\varepsilon_{\mathrm{target}}$	C_{out} / W	$\langle h_1 \rangle$	$\langle h_2 \rangle$	$\langle h_3 \rangle$	$\sigma_{h_1}^2$	$\sigma_{h_2}^2$	$\sigma_{h_3}^2$
0.01	0.5	1	1	1	0.01–0.5	0.01–0.5	0.01–0.5

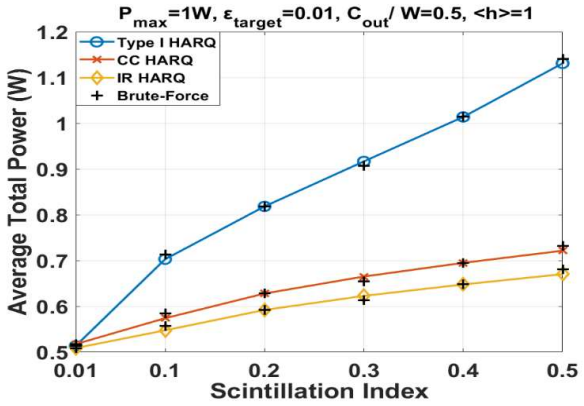

Figure 5-2: Optimization of average total power versus the scintillation index for Type I, CC and IR HARQ schemes.

In the first simulated scenario, the impact of SI on the average total power is evaluated for the three HARQ protocols. The target outage probability, the outage capacity-bandwidth ratio, and the optical channel statistics over the three retransmission rounds are given in Table 5-2, while it is assumed that $SI_1 = SI_2 = SI_3$. The proposed methodology is simulated using the IP and SQP algorithms and validated with a brute-force search. In Figure 5-2 the numerical results are given.

In Figure 5-2, it can be observed that the higher the SI the more power is consumed by all HARQ schemes with a rate of 12% (Type I), 6% (CC) and 5.2% (IR). Type I is the worst and results in the largest average total power and CC is moderate, while IR is the most energy-efficient HARQ protocol. At SI = 0.3, the average total powers of Type I and CC are 47.2% and 6.8% larger than IR, respectively.

In the second scenario of simulations, the impact of $\langle h \rangle$ on the average total power is evaluated for the three HARQ protocols. The target outage probability, the outage capacity-bandwidth ratio, and the optical channel statistics over the three retransmission rounds are given in Table 5-3, while it is assumed that $\langle h_1 \rangle = \langle h_2 \rangle = \langle h_3 \rangle$. The proposed methodology is simulated using the IP and SQP algorithms and validated with a brute-force search. In Figure 5-3 the numerical results are presented.

Table 5-3: Second simulation's input parameters for the optical channel.

$\varepsilon_{\text{target}}$	C_{out}/W	$\langle h_1 \rangle$	$\langle h_2 \rangle$	$\langle h_3 \rangle$	$\sigma_{h_1}^2$	$\sigma_{h_2}^2$	$\sigma_{h_3}^2$
0.01	0.5	0.5–1	0.5–1	0.5–1	0.1	0.1	0.1

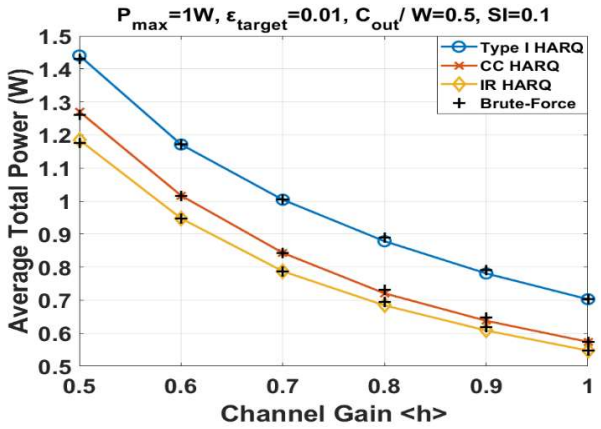

Figure 5-3: Optimization of average total power versus the channel gain for Type I, CC and IR HARQ schemes.

In Figure 5-3, it is shown that the higher the channel gain the less power is consumed by all HARQ schemes with a rate of 12.5% (Type I), 14.5% (CC) and 13.1% (IR). Type I is the worst and results in the largest average total power and CC is moderate, while IR is the most energy-efficient HARQ protocol. At $\langle h \rangle = 0.8$, the average total powers of Type I and CC are 28.4% and 5.4% larger than IR, respectively.

In the third hypothetical simulation, the impact of $\varepsilon_{\text{target}}$ on the average total power is evaluated for the three HARQ protocols. The outage-capacity-to-bandwidth ratio, and the optical channel statistics over the three retransmission rounds, are given in Table 5-4. The proposed methodology is simulated using the IP and SQP algorithms and validated with a brute-force search. In Figure 5-4 the numerical results are given.

Table 5-4: Third simulation's input parameters for the optical channel.

$\varepsilon_{\text{target}}$	C_{out}/W	$\langle h_1 \rangle$	$\langle h_2 \rangle$	$\langle h_3 \rangle$	$\sigma_{h_1}^2$	$\sigma_{h_2}^2$	$\sigma_{h_3}^2$
$10^{-7} - 10^{-1}$	0.5	1	1	1	0.2	0.2	0.2

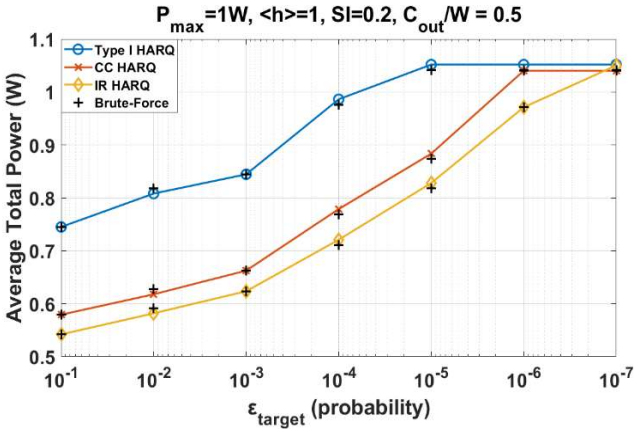

Figure 5-4: Optimization of average total power versus the target outage probability for Type I, CC and IR HARQ schemes.

In Figure 5-4, it is observed that the lesser the $\varepsilon_{\text{target}}$, the more power is consumed by all HARQ schemes with a rate of 6.7% (Type I), 13.4% (CC) and 14.8% (IR). Type I is the worst and cannot achieve an $\varepsilon_{\text{target}} < 1\times10^{-5}$ and CC is moderate and cannot achieve an $\varepsilon_{\text{target}} < 1\times10^{-6}$, while IR is the most energy-efficient HARQ protocol, reaching a threshold of $\varepsilon_{\text{target}} = 1\times10^{-7}$. At $\varepsilon_{\text{target}} = 1\times10^{-5}$, the average total powers of Type I and CC are 27% and 6.7% larger than IR, respectively.

In the fourth simulation, the channel power distribution is evaluated among the three retransmission rounds. The outage-capacity-to-bandwidth ratio, and the optical channel statistics over the three HARQ rounds, are given in Table 5-5. The proposed methodology is simulated using the IP and SQP algorithms and validated with a brute-force search. In Figure 5-5(a) the numerical results are given only for the IR HARQ protocol, which shows the best performance. In Figure 5-5(b) the proposed methodologies are simulated for arbitrary input parameters given in Table 5-5. The average and allocated power are exhibited.

Table 5-5: Fourth simulation's input parameters for the optical channel.

Sim	$\varepsilon_{\text{target}}$	C_{out}/W	$\langle h_1 \rangle$	$\langle h_2 \rangle$	$\langle h_3 \rangle$	$\sigma_{h_1}^2$	$\sigma_{h_2}^2$	$\sigma_{h_3}^2$
(a)	$10^{-7}-10^{-1}$	0.5	1	1	1	0.2	0.2	0.2
(b)	10^{-4}	0.44	0.92	0.97	0.88	0.24	0.30	0.22

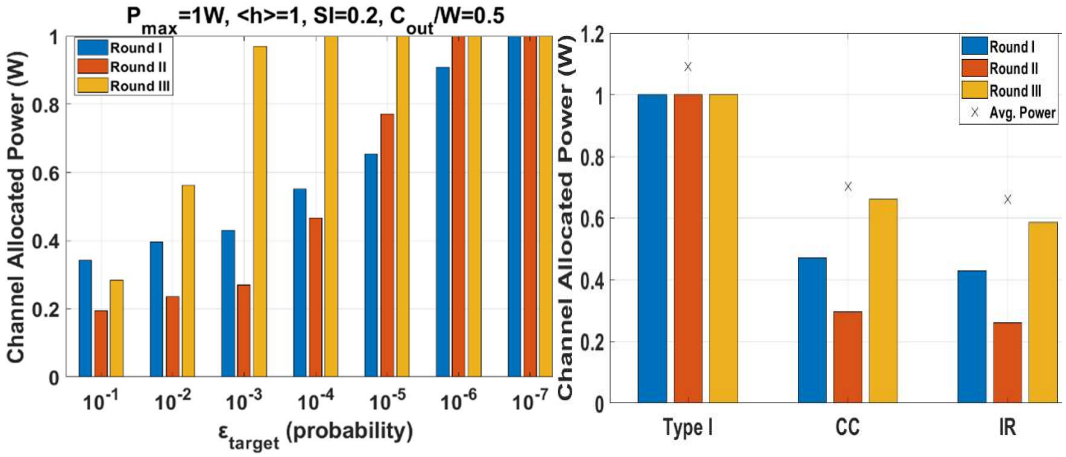

(a) (b)

Figure 5-5: (a) Channel-allocated power versus the target outage probability for the IR HARQ protocol; (b) channel-allocated power and average power of the three HARQ schemes for arbitrary input channel parameters.

In Figure 5-5(a), as the $\varepsilon_{\text{target}}$ gets smaller, it can be observed that the average total power is minimized by allocating the most power on the third round and the least power during the first round until 1×10^{-7} where maximum power is allocated over all three rounds. This is reasonable because from (5.23) the $P_3 \cdot P_r\left(C_2 \le C_{out}\right)$ yields a much smaller term than $P_2 \cdot P_r\left(C_1 \le C_{out}\right)$ or P_1; therefore, P_3 is allocated with maximum power first, followed by less power in P_2 and finally by the least power in P_1. In Figure 5-5(b) it can be observed that CC and IR perform much more efficiently than Type I, and in a similar way, by allocating more power on the first and third rounds. It must be mentioned that not all *M* re-transmissions are required; the proposed methodologies simply indicate the gradual increment of allocated power till the successful decoding or depletion of HARQ rounds [15].

Lastly, a comparison between IP and SQP algorithms has been implemented and shown for the previous case of IR HARQ. The stopping criteria, the termination tolerances of the constraints, the step sizes and the initial power vector $P^{(0)}$ are given in Table 5-6. In Tables 5-7 and 5-8 the algorithms' performance parameters are reported.

Table 5-6: Optimization parameters of IP and SQP algorithms.

	Stopping Criterion	Termination Tolerance	Step Size	Initial Vector
IP	1000 iterations	1×10^{-6}	1×10^{-10}	$P^{(0)} = [0.5\ 0.5\ 0.5]^T$ W
SQP	400 iterations	1×10^{-6}	1×10^{-6}	$P^{(0)} = [0.5\ 0.5\ 0.5]^T$ W

Table 5-7: Performance Parameters of Interior-Point Algorithm

ε_{target}	Iterations	Function Evaluations	1st Order Optimality	Constraint Violations
1×10^{-1}	13	58	3.8×10^{-8}	0
1×10^{-2}	12	53	4×10^{-7}	0
1×10^{-3}	20	91	9.3×10^{-7}	0
1×10^{-4}	22	101	1.6×10^{-8}	0
1×10^{-5}	29	131	3.2×10^{-7}	0
1×10^{-6}	29	133	8×10^{-8}	0
1×10^{-7}	30	139	5.7×10^{-7}	5.7×10^{-7}

Table 5-8: Performance Parameters of Sequential Quadratic Programming Algorithm.

ε_{target}	Iterations	Function Evaluations	1st Order Optimality	Constraint Violations
1×10^{-1}	10	45	3.5×10^{-7}	2.7×10^{-17}
1×10^{-2}	9	43	6.5×10^{-7}	3.1×10^{-11}
1×10^{-3}	8	37	7.3×10^{-7}	2.4×10^{-11}
1×10^{-4}	8	36	1.9×10^{-8}	8.2×10^{-15}
1×10^{-5}	10	44	1.6×10^{-7}	1.4×10^{-17}
1×10^{-6}	12	52	6.7×10^{-7}	3×10^{-15}
1×10^{-7}	9	68	8.6×10^{-7}	8.6×10^{-7}

Although the two algorithms (IP and SQP) yield the same numerical results in all the examined cases, as exhibited previously in Figures 5-2 – 5-5, they require a different number of iterations and function evaluations. Additionally, they converge to a local minimum with different first-order optimality and constraint violations. The first-order optimality translates to the maximum absolute value (infinity norm) of the gradient of the Lagrangian, and ideally

it should be zero at the minimum. The constraint violations refer to the nonlinear target outage probability constraints and ideally, they should be zero.

From Tables 5-1 and 5-2 it is observed that IP algorithm requires approximately 3 times more iterations and function evaluations than SQP, especially at $\varepsilon_{\text{target}} = 1 \times 10^{-7}$, which means that IP is slower. This outcome is reasonable since IP by definition is required to stay inside the feasible region and bounds at all iterations, while SQP allows some constraint and bound violations. On the other hand, IP achieves better first-order optimality has almost no constraint violations, which makes IP a better approximation of the local minimum than SQP.

5.5 Conclusions

In this Chapter, optical HARQ-based LEO-to-ground downlinks under weak turbulence conditions are studied, and a power allocation methodology is proposed to ensure reliable and energy-efficient transmission. Specifically, to optimize the system's energy efficiency and reliability, the average power consumption is minimized given a maximum transmitted power constraint and a target outage probability constraint. Assuming a finite number of rounds with temporal spacing between retransmissions of at least a channel's coherence time, the optimization problem is constructed as a constrained nonlinear programming problem for the cases of Type I, CC and IR HARQ schemes. The optical channel's statistics are required to obtain the optimal power allocation rather than the instantaneous channel gains. The solutions are derived numerically via iterative algorithms, namely IP and SQP, and validated through a brute-force search, i.e., a search of all points in the feasible region. Simulations are then executed to evaluate the proposed methodology and provide performance parameters of IP and SQP while also exhibiting the impact of SI, average path loss and target outage probability. The numerical results show that Type I HARQ yields the highest average total power, CC is moderate and IR yields the lowest average total power. The IP algorithm was found to be more accurate in finding the global solution because of its nearly zero first-order optimality and constraint violations, but SQP is faster due to the smaller number of iterations and function evaluations. Finally, real experimental data from optical LEO-to-ground can be employed to evaluate the feasibility of HARQ schemes.

Chapter References

[1] Chaudhry, A.U.; Yanikomeroglu, H. Free Space Optics for Next-Generation Satellite Networks. *IEEE Consum. Electron. Mag.* **2021**, *10*, 21–31.

[2] Uysal, M.; Capsoni, C.; Ghassemlooy, Z.; Boucouvalas, A.; Udvary, E. *Signals and Communication Technology Optical Wireless Communications-An Emerging Technology*; Springer International Publishing: Cham, Switzerland, 2016; pp. 1–639.

[3] Kaushal, H.; Kaddoum, G. Free Space Optical Communication: Challenges and Mitigation Techniques. *IEEE Commun. Surv. Tutor.* **2016**, *19*, 57–96.

[4] Hemmati, H. *Near-Earth Laser Communications Edited By*; CRC Press: Boca Raton, FL, USA, 2009.

[5] Dosti, E.; Shehab, M.; Alves, H.; Latva-Aho, M. Ultra Reliable Communication via Optimum Power Allocation for HARQ Retransmission Schemes. *IEEE Access* **2020**, *8*, 89768–89781.

[6] Hosseini, S.S.; Abouei, J.; Champagne, B.; Chang, X.W. A Novel Cooperative HARQ Protocol for Free-Space Optical Broadcasting Systems. *J. Lightwave Technol.* **2020**, *38*, 1789–1799.

[7] Pan, G.; Ye, J.; Tian, Y.; Alouini, M.S. On Harq Schemes in Satellite-Terrestrial Transmissions. *IEEE Trans. Wirel. Commun.* **2020**, *19*, 7998–8010.

[8] Kiasaleh, K. Hybrid ARQ for FSO Communications through Turbulent Atmosphere. *IEEE Commun. Lett.* **2010**, *14*, 866–868.

[9] Kolev, D.R.; Toyoshima, M. Satellite-to-Ground Optical Communications Using Small Optical Transponder (SOTA)—Received-Power Fluctuations. *Opt. Express* **2017**, *25*, 28319–28329.

[10] Tokovinin, A.; Kellerer, A.; du Foresto, V.C. FADE, an Instrument to Measure the Atmospheric Coherence Time. *Astron. Astrophys.* **2008**, *477*, 671–680.

[11] Zedini, E.; Chelli, A.; Alouini, M.S. Unified Performance Analysis of Hybrid-ARQ with Incremental Redundancy over Free-Space Optical Channels. In Proceedings of the IEEE 25th Annual International Symposium on Personal, Indoor, and Mobile Radio Communication (PIMRC), Washington, DC, USA, 1–2 September 2014; pp. 774–778.

[12] Zedini, E.; Chelli, A.; Alouini, M.S. On the Performance Analysis of Hybrid ARQ With Incremental Redundancy and With Code Combining Over Free-Space Optical Channels With Pointing Errors. *IEEE Photonics J.* **2014**, *6*, 1–18.

[13] Chaitanya, T.V.K.; Larsson, E.G. Outage-Optimal Power Allocation for Hybrid ARQ with Incremental Redundancy. *IEEE Trans. Wirel. Commun.* **2011**, *10*, 2069–2074.

[14] Su, W.; Lee, S.; Pados, D.A. The Optimal Transmission Power Per Round for Hybrid-ARQ Rayleigh Fading Links. In Proceedings of the IEEE International Conference on Communications, Cape Town, South Africa, 23–27 May 2010; pp. 1–5.

[15] Dosti, E.; Charalambous, T.; Wichman, R. Power Allocation for ARQ Two-Hop Cooperative Networks for Ultra-Reliable Communication. In Proceedings of the IEEE International Conference on Communications (ICC), Dublin, Ireland, 7–14 June 2020; pp. 1–7.

[16] Chen, Y.-A.; Zhang, Q.; Chen, T.-Y.; Cai, W.-Q.; Liao, S.-K.; Zhang, J.; Chen, K.; Yin, J.; Ren, J.-G.; Chen, Z.; et al. An integrated space-to-ground quantum communication network over 4600 kilometres. *Nat. Cell Biol*. **2021**, *589*, 214–219.

[17] Ntanos, A.; Lyras, N.K.; Zavitsanos, D.; Giannoulis, G.; Panagopoulos, A.D.; Avramopoulos, H. LEO Satellites Constellation-to-Ground QKD Links: Greek Quantum Communication Infrastructure Paradigm. *Photonics* **2021**, *8*, 544.

[18] Nocedal, J.; Wright, S.J. *Numerical Optimization Second Edition*; Springer Science & Business Media LLC, New York, USA, 2006.

[19] Boyd, S.P.; Vandenberghe, Lieven. In *Convex Optimization*; Cambridge University Press, 2004.
[20] Kolev, D.R.; Toyoshima, M. Received-Power Fluctuation Analysis for LEO Satellite-to-Ground Laser Links. *J. Lightwave Technol.* **2017**, *35*, 103–112.
[21] Kapsis, T.T.; Panagopoulos, A.D. Optimum Power Allocation Based on Channel Conditions in Optical Satellite Downlinks. *Wireless Pers. Commun.* **2021**, *116*, 2997–3013.

Chapter 6
Robust Power Allocation in Optical Satellite MIMO Links With Pointing Jitter[7]

In this Chapter, an optical satellite system is considered comprised of a geostationary satellite with multiple transmitters on-board and an optical ground station with multiple receiving telescopes. A robust power allocation strategy for the downlink is investigated incorporating the effects of the atmospheric impairments as well as the optical beam pointing jitter. Firstly, a theoretical analysis for the optical satellite system under pointing jitter is given and a maximin optimization problem is formulated maximizing the worst-case network capacity. The power allocation is carried out under peak and total power constraints using standard convex techniques. The lower bound of the ergodic network capacity for independent log-normal optical channels over variable jitter variance is derived. The proposed methodologies are evaluated via simulations using experimental channel measurements from the ARTEMIS-optical satellite campaign and their performances are compared to baseline power allocation strategies. The presented results show the effects of jitter on the network capacity and confirm the superiority of the proposed allocation scheme.

6.1 Introduction

The vision of the fifth-generation (5G) digital mobile networks is to bring revolutionary network capabilities and services that range from advanced cognitive radio to Internet of Things applications. Operation in challenging heterogeneous communication environments, high reliability and availability, global continuous coverage, and minimal latencies are some of the aspects of the 5G standard. The backhaul portion of the core network is expected to employ either wired means, i.e., optic fibres to interconnect the small cells but the installation cost and time are major limiting factors that hinder further deployment, or Free Space Optics

(FSO) solutions that bring unique transmission features capable to address the aforementioned challenges and alleviate the heavily congested backhaul sub-systems [1–2]. They offer quick installation and affordable cost, without the need for large or heavy equipment, incredible bandwidth potential reaching several THz, point-to-point communications improving the link's security from unwanted interferences [1–2]. The optical satellite technology especially is currently being developed and tested for feeder links while its feasibility has been proved in numerous experimental missions [2–3].

Albeit the optical satellite links perform exceptionally in good weather conditions, the received signal is greatly weakened or completely lost when the levels of atmospheric absorption and scattering are extreme, i.e., due to clouds and fog [1]. Still, atmospheric turbulence affects the beam propagation even in a cloud-free scenario and can cause beam broadening and more importantly the scintillation effects. The latter lead to received irradiance temporal disturbances because of the variations in the refractive index on the slant path. Another issue is the possible pointing error that induces uncertainty due to link misalignment and random vibrations or movements of the telescope platform also known as jitter [4–5]. These adverse effects are usually mitigated by enlarging the receiver's aperture diameter [6]. Nevertheless, for commercial, small and compact telescopes the pointing jitter is a loss factor that has to be taken into account even in downlinks. The small-sized optical telescopes and the directivity properties of the laser beams facilitate the employment of optical multiple-input multiple-output (MIMO) antenna systems to increase the network capacity and throughput by establishing uncorrelated parallel optical channels [7].

In this Chapter, the power allocation optimization problem is studied for an optical satellite-to-ground system consisting of a geostationary earth orbit (GEO) satellite and an optical ground station (OGS) communicating through optical MIMO channels under the effects of atmospheric attenuation, turbulence and pointing jitter. The knowledge of both optical channels' statistics and instantaneous gains, i.e., long-term and short-term Channel State Information at Transmitter (CSIT) respectively, is necessary to maximize the ergodic network capacity. However, the pointing jitter is a stochastic process that can't be accurately predicted in the short term hence a robust methodology is proposed to deal with the jitter uncertainty. Robust optimization problems for radio frequency (RF) systems have been investigated in [8–11]. Optical satellite networks were recently considered in [12–14] but the robust optimization problem for optical satellite links has not been studied yet. The following two cases of objective functions are analysed:

i. The worst-case capacity yielding a maximin optimization problem with peak and total power constraints. This metric is taken under the concept of confidence intervals since the exponential pointing error term is bounded in an interval [0,1] [8]. The worst capacity occurs when the jitter term reaches its lowest point.

ii. The lower bound of the ergodic capacity while the power constraints are the peak and average total power. The expected pointing jitter noise power is considered to obtain only a lower bound. The optimal performance requires accurate knowledge of the exact pointing error [9].

The main contributions are as follows:

i. A robust convex optimization problem is formulated and solved for parallel GEO-to ground optical links under the effects of atmospheric turbulence and pointing jitter.

ii. The robust optimization problem has never been studied for optical MIMO satellite links yet. The research on MIMO optical satellite links is also a contribution of this letter. The incorporation of atmospheric scintillation and the pointing jitter impairments in the whole analysis yields a considerably different problem than the RF one.

iii. The simulations are performed using real experimental channel data from the European Space Agency's ARTEMIS optical program [15].

iv. The proposed power allocation schemes can be easily employed because they converge to the optimal solution rapidly. To the authors' best knowledge this is the first time that this problem is investigated in optical satellite networks.

For the remainder of this Chapter, in Section 6.2 the system model, and the major assumptions are described. In Section 6.3, the optimization problem is formed and the solutions' methodologies are developed. In Section 6.4, the ARTEMIS experiment is briefly described and the simulation results are exhibited and commented, while in Section 6.5 the conclusions are reported.

6.2 System and Channel Model

In this Section, optical GEO-to-ground communication links are considered over turbulent atmospheric channels with a channel response matrix $\mathbf{H} \in \mathrm{R}^{R \times T}$ where R is the number of receiving apertures and T is the number of transmitting terminals. The Intensity Modulation/Direct Detection (IM/DD) scheme is employed, the optical channels are assumed uncorrelated (distances greater than Fried parameter [1]) and cloud-free (otherwise clouds

block the communication [1]) but suffer from path losses, scintillation, and pointing jitter. For a collimated Gaussian beam the received irradiance at distance L is [4,6]:

$$I_{gaus}(\boldsymbol{\rho}, L) = \frac{2P_t}{\pi w_L^2} \exp\left(-\frac{2\|\boldsymbol{\rho}\|^2}{w_L^2} \right), \tag{6.29}$$

where P_t is the transmitted power, $\boldsymbol{\rho}$ is the radial distance vector from the centre axis of the beam, and W_L is the radius at which the field amplitude falls to $1/e^2$ of its axial values (beam waist at distance L).

Incorporating the atmospheric transmittance losses η_{atm}, and the quantum efficiencies of transmitters and receivers η_t, η_r, the expression (6.1) becomes [4]:

$$I_{path}(\boldsymbol{\rho}, L) = \frac{2P_t}{\pi w_L^2} \eta_{atm} \eta_t \eta_r \exp\left(-\frac{2\|\boldsymbol{\rho}\|^2}{w_L^2} \right) \tag{6.30}$$

Finally, the stochastic effects of scintillation and jitter are included as follows [4,6]:

$$I_{rr}(\mathbf{r}, L) = \frac{2P_t}{\pi w_L^2} \eta_{atm} \eta_t \eta_r \exp\left(2X_s\right) A_0 \exp\left(-\frac{2\mathbf{r}^2}{w_{L,eq}^2} \right), \tag{6.31}$$

where X_s is a stochastic process defined as the log-amplitude of field fluctuations due to scintillation, $\mathbf{r}$ is the pointing deviation from the centre of the aperture, A_0 is the fraction of the collected power at $\mathbf{r} = 0$, $W_{L,eq}$ is the equivalent beamwidth. The (6.3) shall be written now as:

$$I_{rr}(\mathbf{r}, L) = P_t \, PL(L) \, h_s^2(X_s) \, h_j^2\left(\mathbf{r}\right), \tag{6.32}$$

where $PL(L)$ are the total path losses, $h_s^2\left(X_s\right)$ is the scintillation term, and $h_j^2\left(\mathbf{r}\right)$ is the jitter term. The strength of scintillation effects is estimated with the scintillation index (SI):

$$\sigma_I^2 = \left\langle I^2 \right\rangle \Big/ \left\langle I \right\rangle^2 - 1, \tag{6.33}$$

where $\langle I \rangle$ is the average received irradiance in W/m^2. In our analysis, we consider the specific case of weak scintillation conditions (SI < 1) for satellite links with elevation angle higher than 20° (something that is usual for feeder links). In this case, an analytical formula for SI is provided by Rytov [1]:

$$\sigma_R^2 = 2.25 k^{7/6} \sec^{11/6}(\zeta) \int_{H_{OGS}}^{H_{GEO}} C_n^2(h) \left(h - H_{OGS}\right)^{5/6} dh, \tag{6.34}$$

where $k = 2\pi/\lambda$ (*rad/m*) is the wavenumber, sec( ) is the secant function, ζ (*rad*) is the zenith angle, $C_n^2(h)$ is the refractive index structure parameter, h(*m*) is the vertical height, and H_{GEO},

H_{OGS} are the altitudes of GEO and OGS. The $C_n^2(h)$ is a function of the ground weather conditions and is given by the Hufnagel-Valley model in [1]. Moreover, the received irradiance follows the Lognormal distribution with the following Probability Density Function (PDF) [1,5]:

$$f_{h_s^2}(I) = \frac{1}{I\sqrt{2\pi}\sigma_I} \exp\left\{ -\frac{\left[\ln\left(I/\langle I\rangle\right) + 0.5\sigma_I^2\right]^2}{2\sigma_I^2} \right\} \tag{6.35}$$

Regarding the pointing jitter, **r** is a Rayleigh distributed variable and therefore the irradiance follows a special case of beta distribution (PDF) [1,4] with mean value $E\left[h_j^2\right] = A_0 \frac{w_{L,eq}^2}{4\sigma_r^2 + w_{L,eq}^2} = A_0 \frac{\beta}{\beta+1} = \tau$ whereas $\beta = w_{L,eq}^2 / 4\sigma_r^2$ and σ_r is the jitter's standard deviation [5,6]. The normalized variance of h_j^2 in the presence of pointing jitter is [5,6]: $\sigma_j^2 = \frac{E\left[h_j^4\right]}{\left(E\left[h_j^2\right]\right)^2} - 1 = \frac{1}{\beta(\beta+2)}$. Thus, in perfect link alignment and pointing conditions, it is easy to see that $\tau = A_0$, $\mathbf{r} = \sigma_r = 0$.

The employed optical channel models are supported by related work where the Log-normal distribution is considered for the modeling of weak turbulence and the Rayleigh distribution for the radial displacement [16–19]. Moreover, it is reported that it's safe to presume that the jitter variance is the same both horizontally and vertically [16–19]. Finally, GEO-to ground parallel optical links are considered so the transmitters are on-board the same vibrating platform implying approximately independent and identically distributed (i.i.d.) jitter variables. The proposed methodology still applies to a non-i.i.d. jitter assumption.

6.3 The Optimization Problem

Considering the impact of pointing jitter, the optical satellite system is expressed [20]:

$$\mathbf{y} = \mathbf{JHx} + \mathbf{n}, \tag{6.36}$$

where $\mathbf{y} \in \mathbb{R}^{R\times 1}$ is the received signal vector, $\mathbf{J} \in \mathbb{R}^{R\times R}$ is the pointing jitter matrix with elements h_j^2, $\mathbf{H} \in \mathbb{R}^{R\times T}$ is the optical channel response matrix representing the path loss and scintillation with elements h_s^2, $\mathbf{x} \in \mathbb{R}^{T\times 1}$ is the transmitted signal vector, and $\mathbf{n} \in \mathbb{R}^{R\times 1}$ is the optical noise with variance σ_n^2 and represents the ambient optical interference.

It includes the background radiation from the various celestial bodies, the Amplified Spontaneous Emission (ASE) from the optical preamplifier and the electronic detection noise [1]. The constant bias with respect to the background sky radiance can be mitigated by using narrow bandpass optical filters and a small field-of-view of the received telescopes [21,22]. The ASE can also be removed via bandpass filtering with a bandwidth of multiple times the data rate [1]. Ultimately, the dominant thermal or shot noises can be modelled as independent and zero-mean Additive White Gaussian Noise for IM/DD systems [19,21,22]. The satellite communication designers of an optical space-to-ground link are taking into account all these possible environmental noise sources, by incorporating interference margins to mitigate them so they cannot affect the proposed power allocation methodology.

Because the receiver expects an average jitter loss of τ [1], any deviation from this expected value induces an additive noise component as follows [20]:

$$\begin{aligned}\mathbf{y}=\mathbf{JHx}+\mathbf{n}&=\left(\mathbf{J}+\tau\mathbf{I}-\tau\mathbf{I}\right)\mathbf{Hx}+\mathbf{n}=\left(\tau\mathbf{I}\right)\mathbf{Hx}\\&+\left(\mathbf{J}-\tau\mathbf{I}\right)\mathbf{Hx}+\mathbf{n}=\left(\tau\mathbf{I}\right)\mathbf{Hx}+\tilde{\mathbf{n}}\ ,\end{aligned}\tag{6.37}$$

Where $\tilde{\mathbf{n}}=\left(\mathbf{J}-\tau\mathbf{I}\right)\mathbf{Hx}+\mathbf{n}$ is the new total noise with mean value $\mathrm{E}\left[\tilde{\mathbf{n}}\right]=\mathrm{E}\left[\left(\mathbf{J}-\tau\mathbf{I}\right)\mathbf{Hx}+\mathbf{n}\right]=0$ and covariance matrix $\mathbf{\Sigma}=\mathrm{E}\left[\tilde{\mathbf{n}}\tilde{\mathbf{n}}^{H}\right]$. Considering uncorrelated, parallel downlinks with *R=T=N,* the network's capacity in (bps/Hz) is given by:

$$C_{sys}=\sum_{i=1}^{N}\log_2\left(1+\frac{\tau^2 PL\,h_{s,i}^2P_i}{\sigma_n^2+PL\left(h_{j,i}^2-\tau\right)^2h_{s,i}^2P_i}\right)\tag{6.38}$$

The worst-capacity scenario occurs when the deviation Ω from the mean jitter losses is maximum i.e., $\Omega=\left(h_{j,i}^2-\tau\right)^2=\max$. From (6.3) the $h_j^2\left(\mathbf{r}\right)$ has a confidence interval $\left[\varepsilon_1,\varepsilon_2\right]\subseteq\left[0,1\right]$. In this circumstance, the Robust Maximin Power Allocation problem is formulated as follows [8]:

$$\max_{P_i}\min C_{sys}=\sum_{i=1}^{N}\log_2\left(1+\frac{\tau^2 PL\,h_{s,i}^2P_i}{\sigma_n^2+PL\,\Omega\,h_{s,i}^2P_i}\right)\tag{6.39}$$

$$\text{s.t. }\ 0\le P_i\le\overline{P},\ 0\le\sum_{i=1}^{N}P_i\le P_{tot}\ ,\tag{6.40}$$

where $\overline{P}$ is the peak optical power and P_{tot} is the total transmit power. The problem is convex with respect to P_i and by applying the Karush-Kuhn-Tucker (KKT) conditions, the solution in closed-form is [23–24]:

$$P_i = \frac{-\sigma_n^2\left(2\Omega+\tau^2\right)+\sigma_n\sqrt{\tau^4\sigma_n^2+\dfrac{4PL\,\Omega\,h_{s,i}^2\,\tau^2\left(\Omega+\tau^2\right)}{v}}}{2PL\,h_{s,i}^2\,\Omega\left(\Omega+\tau^2\right)} \tag{6.41}$$

The optimal power allocation is:

$$P_i^* = \min\left\{\overline{P}, \max\left(P_i, 0\right)\right\} \tag{6.42}$$

The value of v is evaluated iteratively as follows [23]:

$$\sum_{i=1}^{N} P_i^* = P_{tot} \tag{6.43}$$

Here it is assumed that the GEO transmitters have only long-term CSIT so a lower bound of average capacity is attainable. The Ergodic Capacity Power Allocation problem is formulated as follows [9]:

$$\max_{P_i} \mathrm{E}\left[C_{sys}\right] = \mathrm{E}\left[\sum_{i=1}^{N}\log_2\left(1+\frac{\tau^2 PL\,h_{s,i}^2 P_i}{\sigma_n^2+PL\,\sigma_j^2 P_i}\right)\right] \tag{6.44}$$

$$\text{s.t. } 0 \le P_i \le \overline{P},\ 0 \le \mathrm{E}\left[\sum_{i=1}^{N} P_i\right] \le P_{tot} \tag{6.45}$$

The average noise power is given:

$$E\left[\tilde{\mathbf{n}}\tilde{\mathbf{n}}^H\right] = \sigma_n^2\mathbf{I} + E\left[\left(\left(\mathbf{J}-\tau\mathbf{I}\right)\mathbf{H}\mathbf{x}\right)\left(\left(\mathbf{J}-\tau\mathbf{I}\right)\mathbf{H}\mathbf{x}\right)^H\right] = \sigma_n^2\mathbf{I} + PL\,\sigma_j^2 P_i\,\mathbf{I} \tag{6.46}$$

For lognormal channels is $\mathrm{E}\left[h_s h_s^H\right] = \mathrm{E}\left[\exp\left(2X_s\right)\right] = \exp\left(2\mu_{X_s} + 4\sigma_{X_s}^2/2\right) = \exp\left(-2\sigma_{X_s}^2 + 2\sigma_{X_s}^2\right) = 1$ since $\mathrm{E}\left[X_s\right] = -\sigma_{X_s}^2$ where $\sigma_{X_s}^2 = \sigma_I^2/4$ [5].

The problem is convex with respect to P_i and by applying the well-known KKT conditions, the solution in closed-form is found [23–24]:

$$P_i = \frac{-\sigma_n^2\left(2\sigma_j^2+\tau^2 h_{s,i}^2\right)+\sqrt{\tau^4\sigma_n^4\,h_{s,i}^4+\dfrac{4\tau^2\sigma_n^2 PL\,\sigma_j^2\,h_{s,i}^2\left(\tau^2 h_{s,i}^2+\sigma_j^2\right)}{v}}}{2PL\,\sigma_j^2\left(\sigma_j^2+\tau^2 h_{s,i}^2\right)} \tag{6.47}$$

The optimal power allocation is:

$$P_i^* = \min\left\{\overline{P}, \max\left(P_i, 0\right)\right\} \tag{6.48}$$

The value of v is evaluated iteratively as follows [23]:

$$\sum_{i=1}^{N} \mathrm{E}\left[P_i^*\right] = P_{tot} \tag{6.49}$$

The (6.13) and (6.18) are actually the positive solutions of the quadratic equations that are obtained from the KKT stationarity conditions. Since there are no guaranteed bit error rate

constraints, the optimum methodology allocates more power to the stronger optical channels with the best conditions. However, (6.13) and (6.18) are certainly more complex than the water-filling algorithm and are more sensitive to variations of jitter parameters Ω, σ_j than channel gains.

6.4 Numerical Results and Discussion

In 2003, the rollout of the ARTEMIS optical satellite mission took place which was organized by the European Space Agency (ESA) to test the feasibility of optical data-relaying between the ARTEMIS GEO satellite and the high-altitude (2400 m) observatory in Tenerife, Spain. More details for the experiment can be found in [15]. The experimental channel measurements derived from the ESA ARTEMIS optical satellite mission are used to execute simulations to evaluate the performance of the proposed methodologies.

The impact of pointing jitter is the primary parameter that requires sheer investigation. Firstly, the worst–capacity is optimized for various Ω values and our methodology is compared to the Best – Case capacity algorithm that can be obtained from (6.11) by substituting $\Omega = 0$ and then solving i.e., when there is no deviation from expected jitter losses τ. Secondly, the ergodic capacity is optimized for various jitter variances σ_j^2 and our proposed scheme is compared to the Best–Case capacity algorithm that can be obtained from (6.16) for $\sigma_j^2 \simeq 0$ and then solving the optimization problem.

The simulation input parameters are listed in the following Table 6-1. Experimental data are denoted as "Exp" whereas numerical data as "Num".

Table 6-1: Input Parameters

Data	Parameter	Value
Exp	Number of channels	$N = 3$
Exp	$[PL_1\ PL_2\ PL_3]$	$[-67.8 -70.3 -72.5]$ dB
Exp	$[\sigma_{l,1}^2\ \sigma_{l,2}^2\ \sigma_{l,3}^2]$	$[0.0101\ 0.0142\ 0.0274]$
Num	σ_n^2, τ^2	1W/Hz, 0.8
Num	Ω , σ_j^2	0.0 – 1.0
Num	$\overline{P}$, P_{tot}	1 W, 1–3 W

In the first simulation scenario, the worst capacity is computed for various values of Ω, the deviation from the mean jitter losses. A 3x3 optical satellite-to-ground MIMO system is considered under weak turbulence and path losses using the ARTEMIS experimental data for the channel samples. In Figure 6-1 we observe that pointing jitter induces noteworthy losses

that can't be ignored even in downlinks as Ω rises. Specifically, the increased deviation from expected jitter losses causes network capacity to drop almost to half at 3 W.

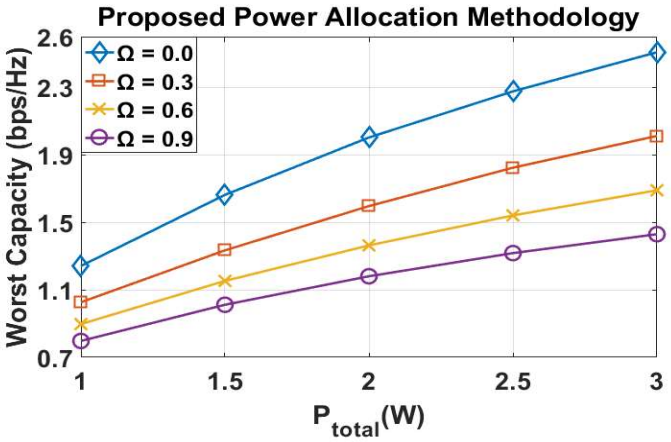

Figure 6-1: Worst capacity versus the total transmitting power. The higher the deviation from the mean jitter losses, the lower the spectral efficiency.

In the second simulation scenario, the proposed methodology is compared to the Best-Case allocation algorithm for the system under investigation. In Figure 6-2 we observe that the larger jitter deviations Ω decrease the sum-rate as anticipated but the difference gets significant at higher Ω where the proposed scheme outperforms Best-Case until the 3 W at which both perform evenly $\left(\overline{P} = 1\,\mathrm{W}\right)$.

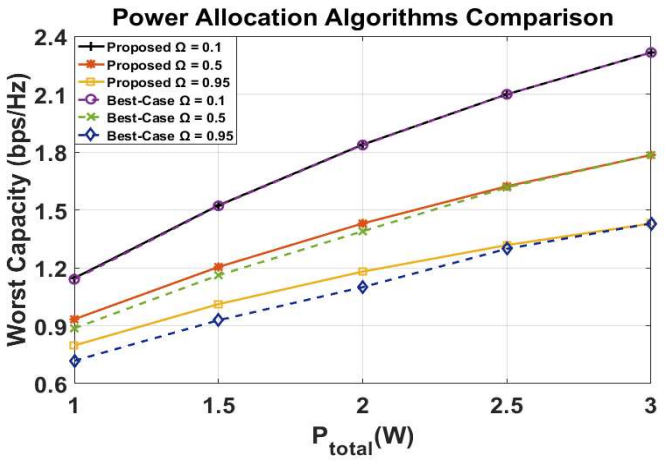

Figure 6-2: Worst capacity versus the total transmitting power. For small Ω the data rate difference is marginal but it gets larger when the Ω increases.

In the last simulation scenarios, new experimental sessions from ARTEMIS have been used with different SIs = {0.111, 0.124, 0.177}. The lower bound of ergodic capacity is

computed for various values of σ_j^2, the jitter variance. From Figure 6-3 we observe that pointing jitter induces average losses similar to the ones for worst capacity. Again, the higher the σ_j^2 the lesser the ergodic capacity falling off several bps/Hz at 3 W as it is easily observed.

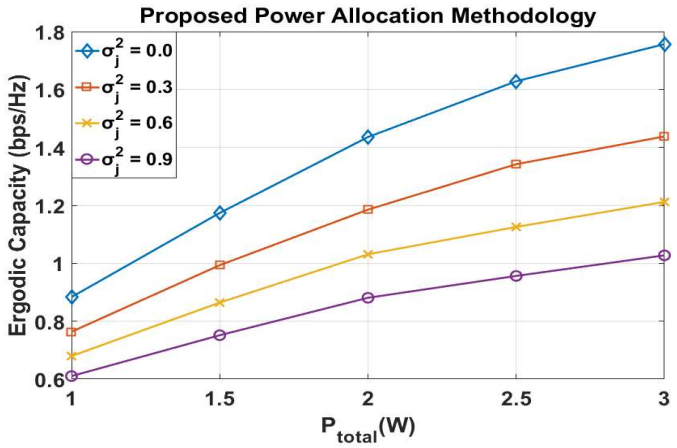

Figure 6-3: Lower bound of ergodic capacity versus the total expected power. The higher the σ_j^2 the lower the network's spectral efficiency.

In the final simulation scenario, the comparison with the Best-Case allocation algorithm is depicted in Figure 6-4. We observe that the jitter variance imposes considerable losses on the sum-rate and the proposed scheme outperforms Best-Case, mainly at higher σ_j^2 values. At 3 W both perform evenly $\left(\overline{P} = 1\,\text{W}\right)$.

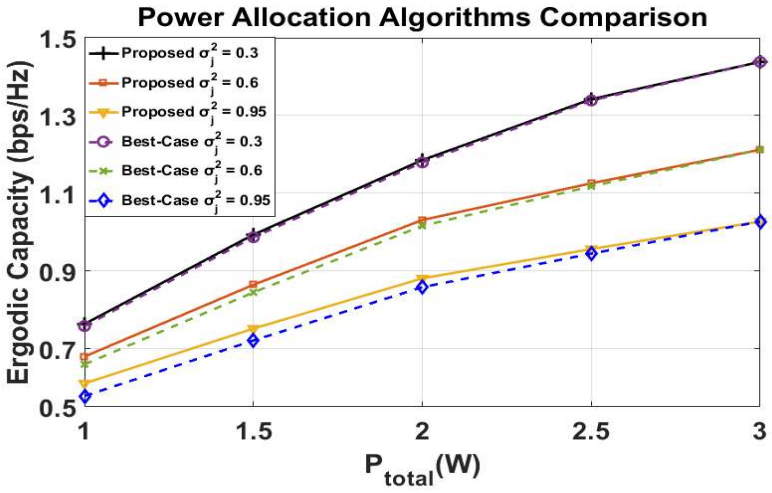

Figure 6-4: Lower bound of ergodic capacity versus the total transmitting. For small σ_j^2 the difference in data rate is marginal but it gets larger when the σ_j^2 increases.

6.5 Conclusions

In this Chapter, a robust power allocation strategy for the optical GEO-to-ground link is proposed that takes into account the atmospheric impairments of the slant path and the link pointing jitter. Specifically, the impact of jitter is examined on the worst-capacity yielding a maximin optimization problem and on the ergodic capacity by incorporating the average pointing jitter noise power obtaining an optimum lower bound. The power allocation is performed under peak and total power constraints employing convex techniques. The proposed methodologies are evaluated via simulations with experimental channel measurements from the ESA ARTEMIS optical satellite campaign and their performance is compared to other power allocation strategies. The network's capacity is severely degraded when the jitter exceeds its expected value, and the outcomes confirm the spectral efficiency superiority of the proposed schemes compared to the Best-Case power allocation algorithm.

Chapter References

[1] H. Hemmati, "Near-Earth Laser Communications," Boca Raton: CRC Press, 2009.

[2] H. Kaushal, G. Kaddoum, “Optical Communication in Space: Challenges and Mitigation Techniques,” in IEEE Comm. Surv. Tutor., 19, 57–96, 2016.

[3] C. -X. Wang, et al "6G Wireless Channel Measurements and Models: Trends and Challenges," in IEEE Vehicular Technology Magazine, vol. 15, no. 4, pp. 22-32, Dec. 2020.

[4] M. Toyoshima, et al. “Optimum divergence angle of a Gaussian beam wave in the presence of random jitter in free-space laser communication systems,” in JOSA A, 19(3), 567-571, 2002.

[5] F. Yang, et alJ. Cheng, T. A. Tsiftsis, “Free-space optical communication with nonzero boresight pointing errors”, IEEE Transactions on Communications, 62(2), 713-725, 2014.

[6] A. A. Farid, S. Hranilovic. “Outage capacity optimization for free-space optical links with pointing errors”, Journal of Lightwave technology, 25(7), 1702-1710 .2007.

[7] T.T. Kapsis, A. D. Panagopoulos, “Optimized Power Allocation Scheme in Optical Satellite Communication Downlinks”, 12th CSNDSP, pp. 1-6, 2020.

[8] A. Rao, A., M. D. Nisar, M. S. Alouini, “Robust power allocation for multicarrier amplify-and-forward relaying systems”, IEEE Transactions on Vehicular Technology, 62 (7), 3475-3481, 2013.

[9] T. Yoo, A. Goldsmith, “Capacity of fading MIMO channels with channel estimation error”, IEEE ICC Vol. 2, pp. 808-813, 2004.

[10] Z. Lin, et al. "Supporting IoT with Rate-Splitting Multiple Access in Satellite and Aerial-Integrated Networks," in IEEE Internet of Things Journal, vol. 8, no. 14, pp. 11123-11134, 15 July15, 2021.

[11] Z. Lin, et al. "Secure and Energy Efficient Transmission for RSMA-Based Cognitive Satellite-Terrestrial Networks," in IEEE Wireless Communications Letters, vol. 10, no. 2, pp. 251-255, Feb. 2021.

[12] Q. Huang, M. Lin, W. -P. Zhu, J. Cheng and M. -S. Alouini, "Uplink Transmission in Mixed RF/FSO Satellite-aerial-Terrestrial Networks," GLOBECOM 2020 - 2020 IEEE Global Communications Conference, pp. 1-6, Dec. 2020.

[13] S. Gong et al., "Network Availability Maximization for Free-Space Optical Satellite Communications," in IEEE Wireless Communications Letters, vol. 9, no. 3, pp. 411-415, March 2020.

[14] T. Lin et al., "Photonic Pre-Coding for MIMO System in Satellite-Terrestrial Communication," in IEEE Access, vol. 8, pp. 40378-40388, 2020.

[15] A. Alonso, et al. “Performance of satellite-to-ground communications link between ARTEMIS and the optical ground station,” Proc. SPIE Vo. 5572, 2004.

[16] M. T. Dabiri,, M. J, Saber, S. M. S. Sadough, “On the performance of multiplexing FSO MIMO links in log-normal fading with pointing errors,” in IEEE/OSA Journal of Optical Communications and Networking 9(11), 974-983, 2017.

[17] H. D. Trung, B. T. Vu, A. T. Pham, “Performance of free-space optical MIMO systems using SC-QAM over atmospheric turbulence channels,” in IEEE International Conference on Communications (ICC), pp. 3846-3850, 2013.

[18] M. T. Dabiri, S.M.S Sadough, M. J. Saber, “Ergodic capacity of MIMO-FSO communications over atmospheric turbulence channels,” in IEEE Iranian Conference on Electrical Engineering (ICEE) pp. 1830-1834, 2017.

[19] H. Safi, A. Dargahi, A., J. Cheng, “Performance Analysis of FSO MIMO Multiplexing Links with Beam Wander and Nonzero Boresight Pointing Errors,” in 16th IEEE Canadian Workshop on Information Theory, pp. 1-6, 2019.

[20] L. Yang, K. Panta, J. Armstrong, “Channel Capacity of OFDM Systems with Timing Jitter,” in IEEE GLOBECOM 2010 pp. 1-5, Dec 2010.
[21] M. Uysal, C. Capsoni, Z. Ghassemlooy, A. Boucouvalas, and E. Udvary “Optical Wireless Communications: An Emerging Technology,” Switzerland, Springer, ISBN: 978-3-319-80748-5, 2016.
[22] M. Rahaim, and T. D. Little, “Interference in IM/DD optical wireless communication networks,” in Journal of Optical Communications and Networking, 9(9), 51-63, 2017.
[23] S. Boyd, L. Vandenberghe, “Convex Optimization,” Univ. Press: Cambridge, U.K., 2004.
[24] D. P. Bertsekas, “Constrained Optimization and Lagrange Multiplier Methods,” New York: Academic Press, 1982.

Chapter 7
Optimal Power Allocations in Optical GEO Satellite Downlinks using Model-Free Deep Learning Algorithms[8]

Geostationary (GEO) satellites are employed in optical frequencies for a variety of satellite services providing wide coverage and connectivity. Multi-beam GEO high-throughput satellites offer Gbps broadband rates and, jointly with low-Earth-orbit mega-constellations, are anticipated to enable a large-scale free-space optical (FSO) network. In this Chapter, a power allocation methodology based on deep reinforcement learning (DRL) is proposed for optical satellite systems disregarding any channel statistics knowledge requirements. An all-FSO, multi-aperture GEO-to-ground system is considered and an ergodic capacity optimization problem for the downlink is formulated with transmitted power constraints. A power allocation algorithm was developed, aided by a deep neural network (DNN) which is fed channel state information (CSI) observations and trained in a parameterized on-policy manner through a stochastic policy gradient approach. The proposed method does not require the channels' transition models or fading distributions. To validate and test the proposed allocation scheme, experimental measurements from the European Space Agency's ARTEMIS optical satellite campaign were utilized. It is demonstrated that the predicted average capacity greatly exceeds other baseline heuristic algorithms while strongly converging to the supervised, unparameterized approach. The predicted average channel powers differ only by 0.1 W from the reference ones, while the baselines differ significantly more, about 0.1–0.5 W.

7.1 Introduction

The progressively demanding criteria of fifth-generation (5G) mobile communications sparked the deployment of high throughput short-range links and mesh topologies to cater to the increased user capacity and to reduce energy consumption [1–2]. The sub-10 GHz radio frequency (RF) band is almost exhausted and strictly regulated. Consequently, scientific research is moving towards the incorporation of millimeter and nanometer wavelengths [1–2]. Optical wireless communications (OWC) operate similarly to fiber optics by modulating a coherent laser beam that propagates point to point and by line of sight [2–6]. Free-space optical (FSO) technology has excellent backhauling capabilities of ultra-fast transfer of traffic between antenna towers and small cells [2–6]. FSO also mitigates the last mile problem, i.e., congestion in the component linking the user to the Cloud/Internet [2–6].

Satellite communications (SatComs) cover a large portion of the Earth, including remote locations, and enable a vast variety of forecasting and broadcasting applications [6–7]. Yet, the cost of designing and manufacturing them is substantial, satellite debris causes "space pollution", and a satellite constellation requires numerous satellites in addition to very quick handovers to guarantee visibility and continuity [6–7]. Especially for high-speed SatComs, FSO systems have exhibited great potential due to their easy installment (<30 min), their operation with low initial expense and maintenance, no licensing requirements like RF systems, and their secure connections due to their large antenna gains, allowing several FSO links to be deployed in parallel and in proximity [2–6]. Nevertheless, they demand advanced pointing, acquisition, and tracking components. The process of creating a private encryption key between two parties is known as quantum key distribution (QKD) [7]. Fundamentally, QKD is an optical technology that can supply encryption keys for any two locations connected by an optical link [7]. The application of QKD over optical fiber, on the other hand, is restricted by exponential fiber losses. In this setting, QKD over satellites is becoming more popular. The capacity to put up robust optical links and guarantee a minimal quantum bit error rate (QBER) by overcoming numerous transmission obstructions is critical to the success of QKD over satellites [7].

However, the FSO beam is susceptible to various problematic atmospheric phenomena, i.e., absorption, scattering, cirrus clouds, and turbulence [2–6]. Physical obstructions, geometric losses, and the blockage of the link caused by cloud occurrence are some of the difficulties [8–9]. For mitigating the cloud occlusion, site diversity can be used [8]. Received irradiance scintillation is created from rapid changes in wind speed, pressure, and

temperature, which in turn induce changes in the refractive index [10–12]. The impact of scintillation depends primarily upon the time of day, the elevation angle of the link, and the altitude of the station [10–12]. In the daytime, at low elevation angles and low-altitude stations (denser atmosphere), turbulence is more extreme [10–12].

In [10–12], the power allocation (PA) problem is investigated for optical satellite downlinks under weak turbulence and solved using a Karush–Kuhn–Tucker (KKT), water-filling-inspired algorithm. However, the reported methodology depends on the knowledge of the system and channel model. In [13–14], a radio-on-FSO (RoFSO) wavelength multiplexing scenario is considered where the channel model is assumed unknown. The developed model-free primal–dual deep learning algorithm (PDDL) strongly converges to the precise solution derived from the model-based algorithm. In both studies, however, synthetic data were employed while the optical satellite-to-ground scenario was not explored. Likewise, in [15] a MIMO FSO system is studied and the PA problem is solved via reinforcement learning (RL) in a deep deterministic policy gradient (DDPG) approach. More power allocation problems regarding FSO, RF, and terrestrial and non-terrestrial networks exploiting ML and deep RL techniques can be found in [16–22].

In this Chapter, several channel-model-free methodologies and heuristics are explored for optimal PA, and then compared to the exact, model-based solution for an all-optical, multi-aperture satellite downlink between a geostationary (GEO) satellite and an optical ground station (OGS). Deep learning (DL) constitutes a powerful tool to handle data from complex and fading communication channels [23–25]. Therefore, the PA problem is formulated as a constrained learning optimization problem with peak and total expected power inequality constraints. Specifically, a deep reinforcement learning (DRL) module is proposed that assists the agents in producing actions via a stochastic policy gradient technique, given channel state information (CSI) observations from the environment. The policy is structured as a deep neural network (DNN) and trained according to the REINFORCE (REward Increment = Nonnegative Factor times Offset Reinforcement times Characteristic Eligibility) algorithm [26], but modified to include the power constraints, and the multi-agent optical environment where the agents act, independently accessing only their local observations but collaboratively trying to maximize the global reward. The proposed PA strategy is deemed appropriate for difficult optical conditions since it learns explicitly from observation. Whilst the optimization problem has been approached in the literature, it has never been presented in a MIMO optical satellite scenario along with available experimental data. Summarizing the main contributions of this Chapter:

i. We propose a DRL-aided algorithm to optimally allocate power in an optical GEO-to-ground multi-aperture system. The proposed method accurately adjusts the expected power for each optical channel, without any knowledge of path losses and scintillation conditions. Only CSI samples are utilized. The total expected power and peak power are constrained. Although in an LEO/MEO scenario deep learning would be even more beneficial, the GEO optical CSI is still unstable due to variations in the refractive index structure parameter along the slant path, thin clouds that may attenuate or block the laser beam, and pointing and tracking errors. Thus, it is challenging to have a more accurate system model and fading distribution knowledge in the short and long term.

ii. Instead of simulated data, experimental irradiance time series from the European Space Agency's (ESA's) ARTEMIS optical satellite sessions were employed to evaluate the performance of the proposed methodology [27–28].

iii. The achieved ergodic system capacity from the application of the proposed algorithm greatly exceeds the performance of the model-free Equal Power, Random Power, and Deep Q-Learning Network (DQN) schemes [20–22] and approaches the model-based, unparameterized solution with very good agreement.

iv. An investigation of the impact of the number of hidden layers and neurons, policy distribution, and hyperparameter selection and overfitting effects was carried out.

v. The proposed solution differs from other standard learning formulas because it applies to a multi-agent optical satellite PA problem based on the parameter sharing approach, allowing centralized learning under a single policy for faster convergence. The learning model is scalable as it has been tested in scenarios with a large number of optical satellite downlinks and a great amount of data and retained its performance. It is especially more scalable than the DQN algorithm because the Q-table is not scalable when there are large, high-dimensional, and continuous state–action pairs [20–22].

In Section 7.2, the optical carrier is described, the system model is presented, and the PA problem is formalized as a learning program. In Section 7.3, the proposed DRL-aided methodology is reported along with other heuristic, model-free strategies. In Section 7.4, the ARTEMIS mission is briefly discussed, and experimental measurements are employed to evaluate and compare the considered PA methodologies. Performance results are drawn and commented on. Section 7.5 concludes this Chapter.

7.2 Channel Model and Power Allocation Problem

The turbulent cells of the atmosphere, known as eddies, work as a prism that will enhance or degrade a propagating optical signal [3]. If an eddy's diameter is almost the size of an incoming beam, it will result in received irradiance I_r fluctuations called scintillation, which is the primary factor of deterioration in the FSO downlink [3]. The scintillation index (SI) σ_I^2 constitutes the normalized ratio of the standard deviation of received irradiance fluctuations to the mean received irradiance [3,29]:

$$\sigma_I^2 = \frac{\left\langle I_r^{\,2} \right\rangle - \left\langle I_r \right\rangle^2}{\left\langle I_r \right\rangle^2} \tag{7.50}$$

where $\left\langle I_r \right\rangle$ represents the mean received optical irradiance in $\mathrm{W/m^2}$. In satellite downlinks with $\sigma_I^2 < 1$, and elevation angle > 20°, the atmospheric turbulence is considered weak [10–12]. In weak turbulence conditions, the optical channel follows the Lognormal$\left(\mu, \sigma_I^2\right)$ with Probability Density Function (PDF) [5]:

$$f_{I_r}(I_r) = \frac{1}{I_r \sqrt{2\pi}\sigma_I} \exp\left\{ -\frac{\left[\ln\left(I_r / \left\langle I_r \right\rangle\right) + 0.5\sigma_I^2\right]^2}{2\sigma_I^2} \right\} \tag{7.51}$$

where $\mu = -0.5\sigma_I^2$.

The optical satellite downlink system under investigation is represented by the real-valued channel matrix $\mathbf{H} \in \mathbb{R}^{N \times M}$ where N is the number of ground receivers (Rx), and M is the number of on-board transmitters (Tx). It is assumed that the covariance matrix $\mathbf{\Sigma} = \mathrm{E}\left[(\mathbf{H} - \mathrm{E}[\mathbf{H}])(\mathbf{H} - \mathrm{E}[\mathbf{H}])^{\mathrm{T}}\right]$ has zero non-diagonal elements, i.e., linearly uncorrelated channels. In practice, this is achieved by having a distance between the Rx elements larger than Fried's parameter [1,29]. The CSI of the channels is denoted as $\left(h_{ij}\right)_{1 \le i \le N,\, 1 \le j \le M}$ and the allocated power as $P_{ij}\left(h_{ij}\right) \mathrm{P_{ij}}\left(\mathrm{h_{ij}}\right)$. The channel capacity is $C_{ij}\left(P_{ij}\left(h_{ij}\right), h_{ij}\right)$ $\mathrm{C_{ij}}\left(\mathrm{P_{ij}}\left(\mathrm{h_{ij}}\right), \mathrm{h_{ij}}\right)$. The average (ergodic) channel capacity is $\mathrm{E}\left[C_{ij}\left(P_{ij}\left(h_{ij}\right), h_{ij}\right)\right]$.

For independent channels, and a proportionate number of Rx and Tx: $N=M=L$ and $i=j=l$, the total average capacity maximization problem is mathematically formalized as follows:

$$(\mathbf{OP}) \max_{\{P_l(h_l):\forall l\}} \sum_{l=1}^{L} \mathrm{E}\left[C_l\left(P_l\left(h_l\right), h_l\right)\right] \tag{7.52}$$

$$\text{s.t.} \quad 0 \le P_l(h_l) \le P_s, \quad \forall l$$
$$\sum_{i=1}^{L} \mathrm{E}\left[P_l(h_l)\right] \le P_{av} \tag{7.53}$$

where P_s is the maximum safety power allocated to a single channel, and P_{av} is the total available power constraint.

7.3 Proposed Methodology

The Lagrangian function to maximize is [30]:

$$L(P_l(h_l), \upsilon) = \sum_{l=1}^{L} \mathrm{E}\left[C_l\left(P_l(h_l), h_l\right)\right] - \upsilon\left(\sum_{l=1}^{L} \mathrm{E}\left[P_l(h_l)\right] - P_{av}\right) \tag{7.54}$$
$$0 \le P_l \le P_s$$

where υ is the dual variable.

If the statistical models $\mathrm{f}_{\mathrm{h_l}}(\mathrm{h_l})$ are available, the average channel capacity is then [11–12]:

$$\mathrm{E}\left[C_l\left(P_l(h_l), h_l\right)\right] = \int_0^{\infty} \log_2\left(1 + \frac{P_l(h_l)|h_l|^2}{N_0}\right) \mathrm{f}_{h_l}(h_l)\,\mathrm{d}h_l \tag{7.55}$$

and the average transmitted power is then [11–12]:

$$\mathrm{E}\left[P_l(h_l)\right] = \int_0^{\infty} P_l(h_l)\,\mathrm{f}_{h_l}(h_l)\,\mathrm{d}h_l \tag{7.56}$$

The PA problem (7.3) and (7.4) is then convex [30]. The instantaneous optimal PA for the i^{th} channel is given in [11–12]:

$$P_l^*(h_l) = \min\left\{P_s, \max\left(\frac{1}{\upsilon^*} - \frac{N_0}{h_l}, 0\right)\right\} \tag{7.57}$$

where υ^* is the optimal dual multiplier, and N_0 is the optical noise variance.

The υ^* is evaluated numerically from (7.4), (7.8) as follows:

$$\sum_{l=1}^{L} \int_0^{\infty} P_l^*(h_l)\,\mathrm{f}_{h_l}(h_l)\,\mathrm{d}h_l = P_{av} \tag{7.58}$$

or via an iterative algorithm, e.g., sub-gradient method with decreasing step size η as below [30]:

$$\upsilon^{k+1} = \left[\upsilon^k - \eta^k\left(P_{av} - \mathrm{E}\left[\sum_{l=1}^{L} P_l(h_l)\right]\right)\right]_+$$
$$\eta^{k+1} = \eta^k / (k+1) \tag{7.59}$$

Note that the analytical expression (7.8) is valid as long as the N_0 $\mathrm{N_0}$is constant and not a function of $\mathrm{P_l(h_l)}$. Also, (7.8) requires precise h_l, and (7.9) demands precise channels' PDFs knowledge to calculate υ^*. In practice, it's very hard to assume accurate model information, CSI values, and constant optical noise.

Supervised learning is a process of providing labeled input datasets to the learning model to make predictions (regression) or decisions (classification) based on the labeled samples. In a regression problem, the output node is continuous ranging theoretically from negative infinity to positive infinity. The mean square error (MSE) is the most common loss function to employ. From (7.8) and (7.10) the exact solution is provided (no need for brute-force or exhaustive search) which can be utilized as ground truth to train a DNN to predict the optimal power allocation. Non-linear regression fitting or a multi-layer perceptron model may be implemented. However, this supervised approach is model-based.

DNNs consist of several layers of interconnected neurons and enable the learning of complex non-linear functions. RL teaches an agent how to execute actions upon entering a new state to maximize the cumulative future returns [23–25]. A DRL methodology refines its policy by directly calculating the policy gradient to maximize the cumulative rewards. The referred policy is a DNN that uses a continuous state as input and produces a probability distribution as output. A continuous action is then sampled. The core idea is to parameterize the policy using a DNN's weights parameter $\boldsymbol{\theta} \in \mathbb{R}^w$ where $w = \sum_{i=1}^{Q} w_i w_{i+1}$ assuming a DNN with Q layers, and each with a corresponding dimension w_i [23–25].

Then, we denote the parameterized policy as the probability distribution of selecting power $P_{t,l}$ for the l^{th} channel in time-step t, and from the state $\left(h_{t,l}, \theta\right)$ [13–14]:

$$\pi\left(\mathbf{h}, \boldsymbol{\theta}\right) = \Pr\left[P_{t,l} \mid h_{t,l}, \theta\right] \tag{7.60}$$

where $h_{t,l}$ $\mathrm{h_{t,l}}$ represents recorded CSI data of l^{th} channel, and $P_{t,l} \in \left[0, P_s\right]$ is the allocated power as derived from $\pi(\mathrm{h}, \theta)$.

The agent's reward-return r_{t+1} at next time-step $t+1$ is the following expression [13–14]:

$$r_{t+1} \quad = L(\theta, \upsilon) \underset{0 \le \pi\left(h_{t,l}, \theta\right) \le P_s}{} = \sum_{l=1}^{L} C_{t,l}\left(\pi\left(h_{t,l}, \theta\right), h_{t,l}\right) - \upsilon\left(\sum_{l=1}^{L} \pi\left(h_{t,l}, \theta\right) - P_{av}\right) \tag{7.61}$$

Then, the discounted cumulative returns G_t are defined as:

$$G_t = r_{t+1} + \gamma r_{t+2} + \gamma^2 r_{t+3} + ... = \sum_{t'=t+1}^{T} \gamma^{t'-t-1} r_{t'} \tag{7.62}$$

where T is the duration of an episode, $t = 0 \ldots T\text{-}1$, and $\gamma \in [0,1)$ is the discount factor [20–22]. The objective function is the long-term discounted rewards [13–14]:

$$J(\theta) = \mathrm{E}\left[G_t \mid \pi(h_t, \theta) \right] \tag{7.63}$$

In general, the gradient for a whole episode with duration T is:

$$\nabla_\theta J(\theta) = \int_T \nabla_\theta \pi_\theta(T) G(T) dT \tag{7.64}$$

If we apply the log-derivative trick $\nabla_\theta \pi_\theta = \pi_\theta \nabla_\theta \log \pi_\theta$ [13–14] then:

$$\nabla_\theta J(\theta) = \mathrm{E}\left[\nabla_\theta \log \pi_\theta(T) G(T) \right] \tag{7.65}$$

Then we obtain a Monte-Carlo approximation of $\mathrm{E}[.]$ in (10.16) for all the $t = 0, 1, \ldots, T\text{-}1$ time-steps, and $l = 0, 1, .., L\text{-}1$ channels [31]:

$$\nabla_\theta J(\theta) = \frac{1}{T} \sum_{t=0}^{T-1} \sum_{l=0}^{L-1} \left[\nabla_\theta \log \pi(h_{t,l}, \theta) G_t \right] \tag{7.66}$$

To summarize, the proposed model-free, DRL methodology requires only h_l samples that can be observed, C_l values that can be experimentally measured, and a differentiable policy to be optimized. The proposed methodology is summarized in Algorithm 1.

Algorithm 1 DRL-aided Proposed Power Allocation Methodology

Initialize number of channels L, number of episodes Ep, episodes duration T, learning rate a, discount factor γ, and weights θ of the policy network;
for $i \leftarrow 0$ **to** Ep-1 **do**
  Set $\nabla_\theta J(\theta) = 0$;
  for $t \leftarrow 0$ **to** T-1 **do**
    for $l \leftarrow 0$ **to** L-1 **do**
      Fetch recorded CSI data $\{h_{t,l}\}$ for each t^{th} time-step and l^{th} optical channel;
      Sample the allocated power $\{\pi(h_{t,l}, \theta)\}$ using the current policy distribution;
      Calculate the returns $\{r_{t+1,l}\}$ from (7.12);
      Calculate $G_{t,l} = \sum_{t'=t+1}^{T} \gamma^{t'-t-1} r_{t',l}$ from (7.13);
      $\nabla_\theta J(\theta) \leftarrow \nabla_\theta J(\theta) + \nabla_\theta \log \pi(h_{t,l}, \theta) G_{t,l}$ from (7.17);
    end
  end
  $\theta \leftarrow \theta + \alpha \nabla_\theta J(\theta) / T$ gradient ascent the policy parameter (DNN's weights);
  $\upsilon \leftarrow \left[\upsilon - \alpha \sum_{t=0}^{T-1} \left\{ \sum_{l=0}^{L-1} \pi(h_{t,l}, \theta) - P_{av} \right\} / T \right]_+$ update dual variable (total power constraint);
end

7.4 Simulations Results

In this Section, the DRL-aided proposed PA methodology is applied to the experimental ARTEMIS time-series data along with other heuristic, model-free strategies, i.e., DQN, Equal Power, Random Power algorithms, and the model-based Supervised method.

The ESA's data relay satellite mission ARTEMIS (Advanced Relay and Technology Mission Satellite) took place in 2003 when the spacecraft attained GEO orbit, and involved a variety of optical communication telescopes for satellite-to-ground and intersatellite bi-directional links [27–28]. The experimental data to be utilized are recorded time series from the downlink transactions from the laser terminal (OPALE) onboard ARTEMIS to the reflector telescope (LUCE) installed on the Teide Observatory in Tenerife, 2400 m above sea level [27–28]. The spacecraft's location and communication features as well as LUCE's and OGS's essential characteristics are given in Table 7-1.

Table 7-1: ARTEMIS, OPALE, LUCE, and OGS Characteristics.

Name	Characteristic	Value
ARTEMIS	Longitude	21.5° East
	Latitude	0.0° ± 2.81° North
	Altitude	35,787 km
	Elevation Angle	37°
	Coverage	Europe, Africa, and the Middle East
OPALE	Wavelength	819 nm
	Beam Diameter ($1/e^2$)	125 mm
	Transmitted Power	10 mW
	Modulation Scheme	Intensity Modulation - Direct Detection
	Data Rate	2 Mbps (downlink), 50 Mbps (uplink)
LUCE	Aperture Diameter	26 cm
OGS	Altitude	2.4 km

In Figure 7-1, the normalized PDFs of five experimental time series are illustrated vs. the normalized PDFs of synthesized data that are lognormally distributed [27–28]. It is obvious that the PDFs derived from the retrieved ARTEMIS data accurately fit the lognormal PDFs implying weak turbulence conditions, and that the channel model in (7.2) can be applied to find the exact solution which will be used as labeled data for the Supervised approach, elaborated in Section 7.3.

The channel samples are then employed to form a 5 x 5 diagonal Multi-Input Multi-Output (MIMO) optical satellite-to-ground system. In general, the channels are assumed cloud-free but suffer from propagation losses and turbulence-induced scintillation.

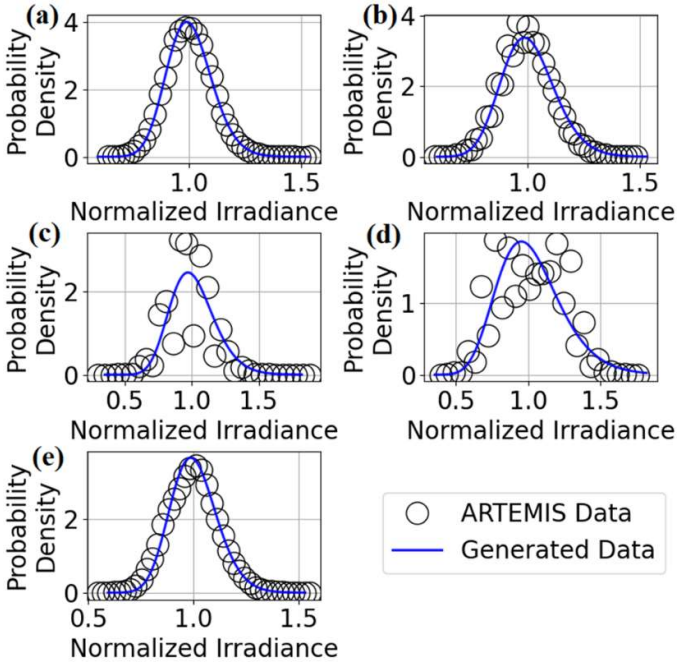

Figure 7-1: Normalized PDFs of experimental and synthesized data. (a) 10/09/2003 20:10-20:30. (b) 10/09/2003 00:30-00:50. (c) 12/09/2003 00:30-00:50. (d) 13/09/2003 23:30-23:50. (e) 16/09/2003 20:10-20:30.

In Table 7-2, the experimental optical channels' mean powers and SIs are included. The lower the $\langle P_r \rangle$ and the higher the SI, the worse the slant path conditions. The channels' correlation is negligible hence they are safely considered independent, and will be denoted as ch.0, ch.1, ch.2, ch.3, and ch.4.

Table 7-2: Optical Channels' Parameters.

Channel	Experiment	Parameters	Values
0	10/09/2003 20:10	$\langle P_r \rangle, \sigma_I^2$	-13.34 dBm, 0.0101
1	10/09/2003 00:30	$\langle P_r \rangle, \sigma_I^2$	-15.79 dBm, 0.0142
2	12/09/2003 00:30	$\langle P_r \rangle, \sigma_I^2$	-19.78 dBm, 0.0274
3	13/09/2003 23:30	$\langle P_r \rangle, \sigma_I^2$	-20.94 dBm, 0.0485
4	16/09/2003 20:10	$\langle P_r \rangle, \sigma_I^2$	-13.85 dBm, 0.0121

To develop the proposed DRL-aided power allocation algorithm, the policy's DNN had to be accurately specified. In particular, the neural network's layers, nodes, and probability distribution must be chosen in a way to avoid overfitting, overhead, and high inference time. In Figure 7-2, the results of an investigation of the optimal number of hidden layers and neurons are shown. From Figure 7-2(a) it is seen that one or two hidden layers are sufficient

as they achieve the maximum average capacity and loss function. From Figure 7-2(b) it is concluded that 256 neurons yield the best performance too.

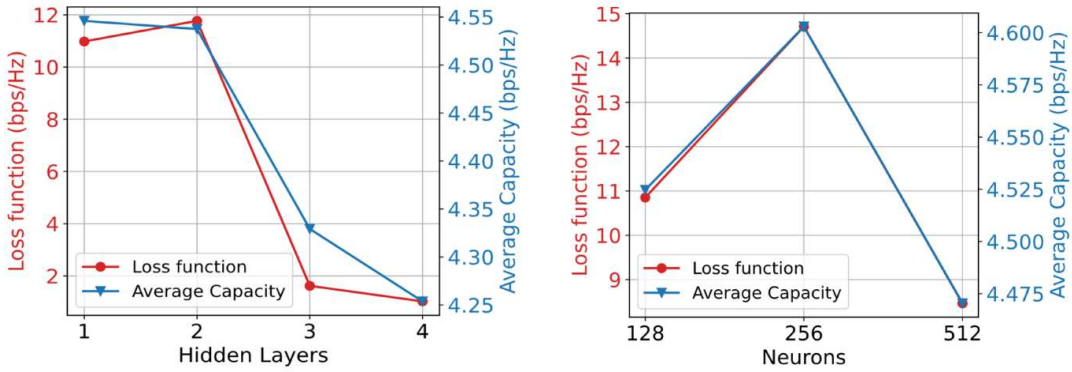

Figure 7-2: The loss function and predicted average capacity in terms of the (a) number of hidden layers (200 nodes/layer) and (b) number of neurons (2 hidden layers). P_s = 1 W, P_{av} = 3 W.

Finally, the stochastic policy that will determine the agents' actions was investigated. In Figure 7-3, three different probability distributions, i.e., truncated Normal $(\mu, \sigma, 0, P_s)$, truncated Weibull $(k, \lambda, 0, P_s)$, and truncated Exponential $(\lambda, 0, P_s)$ were tested and evaluated. Normal and Weibull are two-parameter distributions while Exponential is one-parameter. It is observed that the two-parameter distributions are the best choice and that truncated Normal performs slightly better.

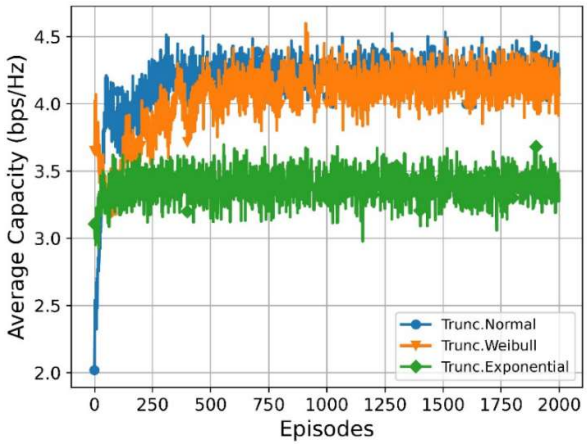

Figure 7-3: Performance results for five optical satellite downlinks using three different policy distributions: truncated Normal (μ,σ,0,Ps), truncated Weibull (k,λ,0,Ps), and truncated Exponential (λ,0,Ps). P_s = 1 W, P_{av} = 2.5 W.

The finalized policy structure consists of a four-layer DNN, as reported in Table 7-3. In addition, the truncated Normal (TN) distribution is selected as a stochastic power policy for the five optical channels.

Table 7-3: Policy DNN Architecture.

Channel	# Nodes	Activation
Input	5	Linear
Hidden #1	200	ReLu
Hidden #2	100	ReLu
Output	10	Softplus

The output nodes are used as parameters of the five TN distributions—means and standard deviations. The optimization algorithm involved in the training is RMSProp with step learning rate scheduling. Specifically, 5000 episodes with a duration of T = 100 time-steps are considered to have frequent weight updates. The initial learning rate is set to 0.001 and the discount factor to 0.5 because fading negatively affects the impact of an agent's actions on his future expected returns [20]. Also, given the total power constraint, the agents' behaviors affect others' rewards due to the unpredictability of their neighbors' actions. Higher γ is also undesirable because it decelerates the response to channel fluctuations [20]. The proposed algorithm was implemented in PyTorch.

In Figure 7.4, the predicted average capacity (a) and the constraint function (b) $\sum_{l=0}^{L-1} \mathrm{E}[P_l(h_l)] - P_{av}$ are depicted for P_{av} = 2.0 W. In Figure 7.5, the average channel powers are illustrated for the proposed, the supervised, the DQN, the Equal Power, and the Random Power algorithms for P_{av} = 2.0 W. Likewise, in Figure 7.6, the predicted average capacity (a) and the constraint function (b) are depicted for P_{av} = 3.0 W, and in Figure 7.7, the average channel powers are illustrated for P_{av} = 3.0 W. Finally, in Figure 7.8, the predicted average capacity (a) and the constraint function (b) are depicted for P_{av} = 4.0 W, and in Figure 7.9, the average channel powers are illustrated for P_{av} = 4.0 W. The DQN is a model-free, off-policy method that tries to predict the Q-values (expected future rewards) for every state–action pair using the ϵ-greedy policy that alternates between exploration and exploitation [20–22]. DQN employs discretized actions: $\left\{0, \overline{P}/A\text{–}1, 2\overline{P}/A\text{–}1, \ldots, \overline{P}\right\}$ where A is the number of actions [20,21,22]. Here, A = 21 was chosen.

The supervised algorithm was trained using the exact solution taken from the water-filling algorithm as if the channel statistics had been known to the transmitter. That scenario is expressed in Section 7.3 and incorporates (7.2), (7.8), and (7.10).

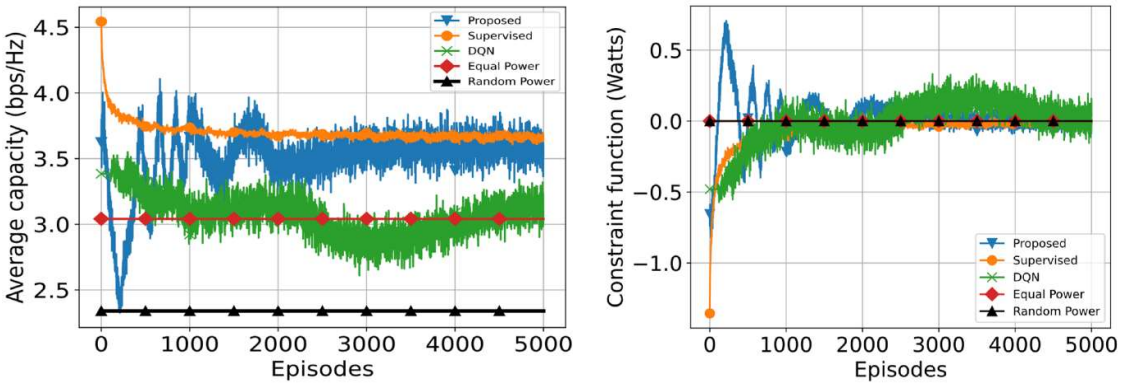

(a) (b)

Figure 7-4: Learning episodes of five different PA algorithms for five optical channels: (a) the average system capacity and (b) the constraint function. $\boldsymbol{P_s = 1\ W, P_{av} = 2\ W}$.

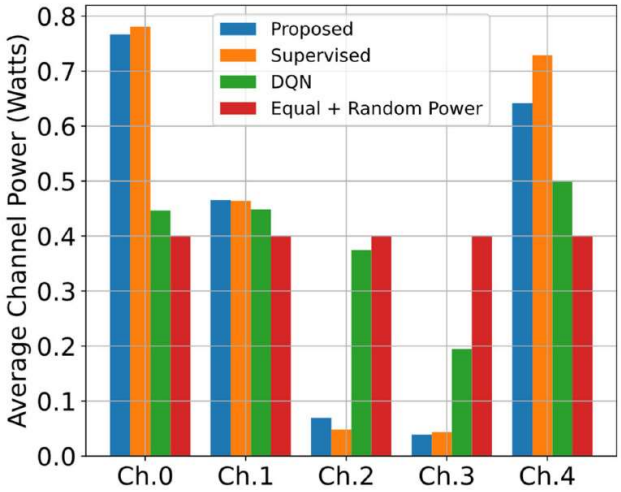

Figure 7-5: The average channel powers of five different PA algorithms for five optical channels during 5000 episodes. $\boldsymbol{P_s = 1\ W, P_{av} = 2\ W}$.

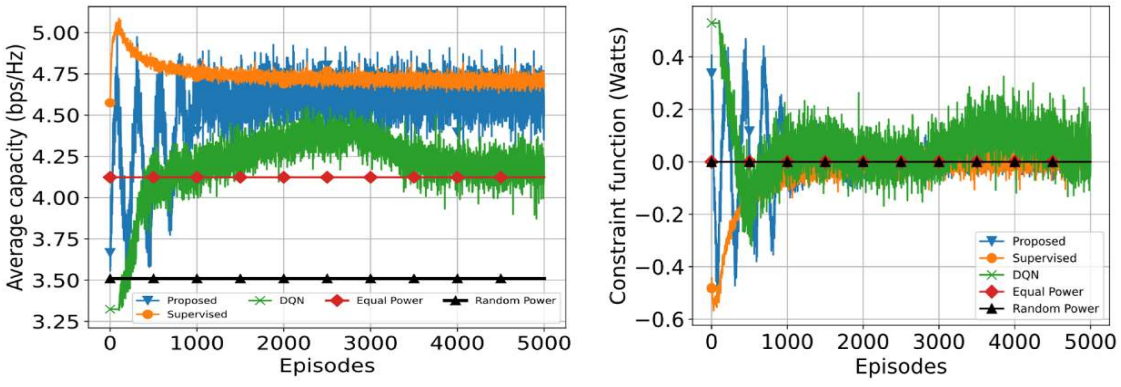

(a) (b)

Figure 7-6: Learning episodes of five different PA algorithms for five optical channels: (a) the average system capacity and (b) the constraint function. $\boldsymbol{P_s = 1\ W, P_{av} = 3\ W}$.

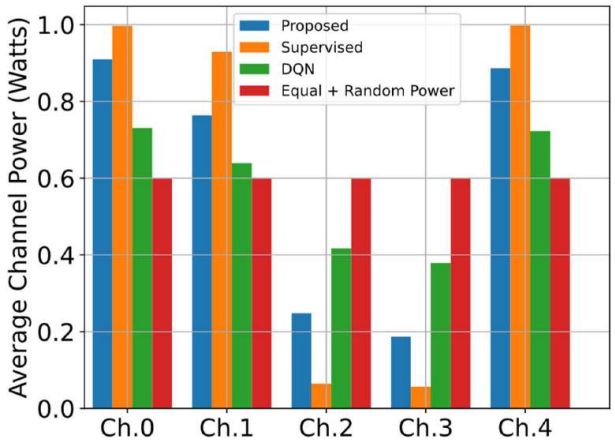

Figure 7-7: The average channel powers of five different PA algorithms for five optical channels during 5000 episodes. $\boldsymbol{P_s = 1\ W, P_{av} = 3\ W}$.

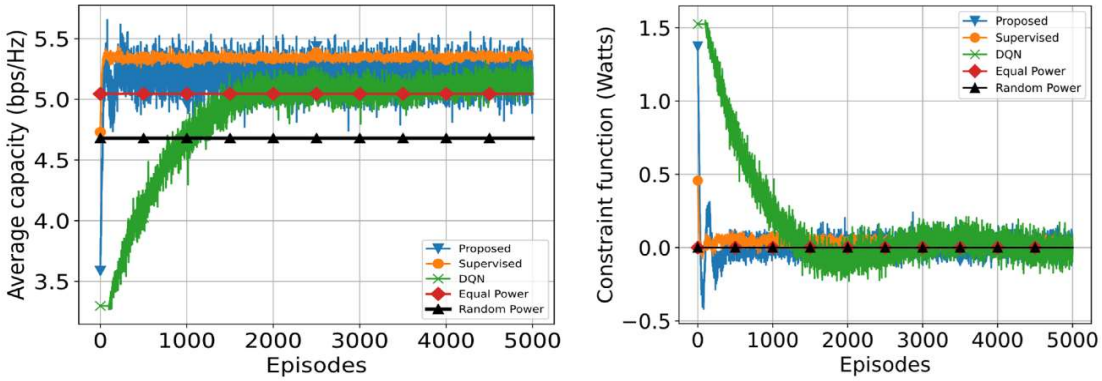

(a) (b)

Figure 7-8: Learning episodes of five different PA algorithms for five optical channels: (a) the average system capacity and (b) the constraint function. $\boldsymbol{P_s = 1\ W, P_{av} = 4\ W}$.

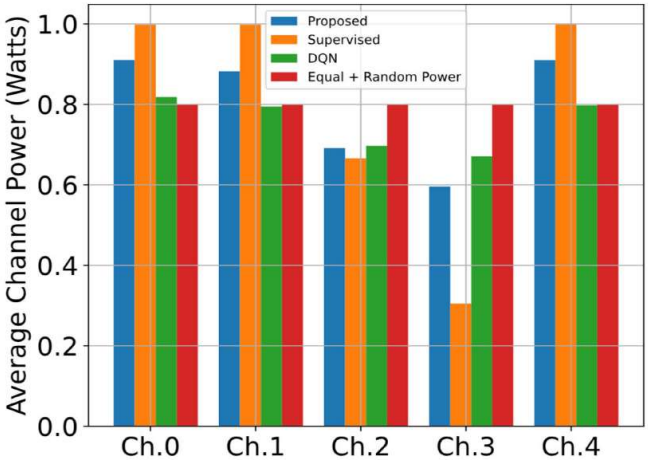

Figure 7-9: The average channel powers of five different PA algorithms for five optical channels during 5000 episodes. $\boldsymbol{P_s = 1\ W, P_{av} = 4\ W}$.

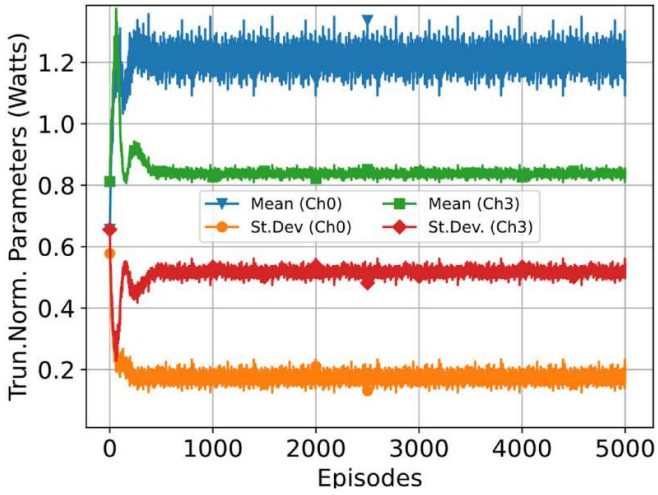

Figure 7-10: The mean and standard deviation of the TN distributions for two allocated channel powers corresponding to ch.0 and ch.3.

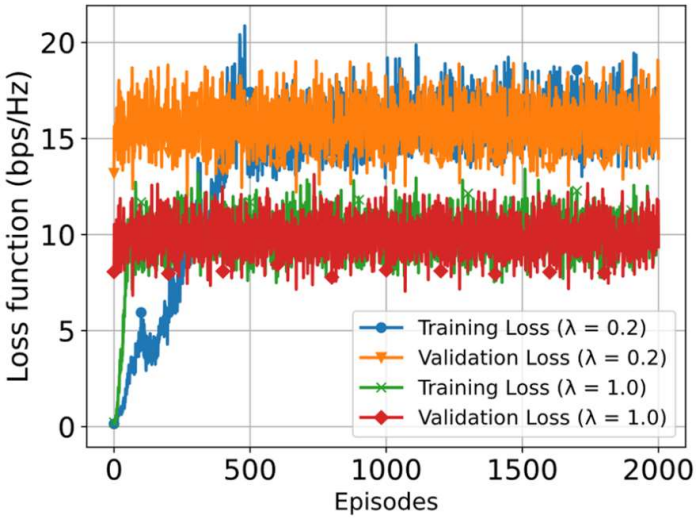

Figure 7-11: Loss function across the training and validation sets for two hyperparameter λ values related to the total power constraint function. $\boldsymbol{P_s = 1W, P_{av} = 3\ W}$. The relaxed $\lambda = 0.2$ allows the power constraint to be violated, resulting in higher loss values, while the stricter $\lambda = 1.0$ yields lower loss values. No overfitting is observed.

In Figure 7.4, Figure 7.6 and Figure 7.8, we observe that the proposed model-free DRL-aided solution outperforms the three baseline algorithms, showing a predicted average capacity advantage (18% better than Equal Power, 16% better than DQN, and 53% better than Random Power for $P_{av} = 2.0$ W). Additionally, it approximates the supervised method with excellent accuracy (2% worse performance for $P_{av} = 2.0$ W). The episode duration of $T = 100$ steps causes some waveform fluctuation, which can be resolved by using more time-steps at the cost of inference time. In Figure 7.5, Figure 7.7 and Figure 7.9, the average channel powers of the proposed algorithm match very well with the supervised ones, i.e., more power

is assigned to the channels with better conditions, only differing by 0.1–0.2 W. The allocated channel powers of the other schemes differ significantly more, about 0.1–0.5 W. The inference time of an episode is 0.7–0.8 s including recorded data sampling, cumulative reward calculation, gradient computation, and back-propagation.

In Figure 7.10, the means and standard deviations of the TN distributions for ch.0 and ch.3 are depicted. Gradually, the values are stabilized according to their conditions in Table 7-2. The mean value of ch.0 (~1.2) is greater than that of ch.3 (~0.85), and the standard deviation of ch.0 (~0.2) is smaller than that of ch.3 (~0.5). Thus, ch.0 has a much higher probability of being allocated with P_s = 1.0 W than the weaker ch.3.

Finally, in Figure 7.11 the loss function is plotted for a training (two-thirds of original dataset) and a validation set (one-third of original dataset), and for two fixed hyperparameter λ values. The λ can be selected to adjust the trade-off between the power constraint violation and the loss function. The training loss is on the same level as the validation loss; therefore, no overfitting is observed.

7.5 Conclusions

In this Chapter, several channel-model-free methodologies and heuristics are explored for optimal PA and then compared to the unparameterized solution for an all-FSO, multi-aperture satellite downlink between a GEO satellite and an OGS. A DRL-aided power allocation methodology is proposed for optical satellite systems disregarding any channel statistics knowledge requirements. Therefore, the PA problem is formulated as a constrained learning optimization problem with peak and total expected power inequality constraints. A power allocation algorithm was developed, aided by a DNN which is fed CSI observations and trained in a parameterized on-policy manner through a stochastic policy gradient approach. The proposed method does not require the channels' transition models or fading distributions. To validate and test the proposed allocation scheme, experimental measurements from the ARTEMIS optical satellite campaign were utilized. The proposed scheme performs 18% better than Equal Power, 16% better than DQN, and 53% better than Random Power, and it approximates the supervised method, with only 2% less accuracy, for P_{av} = 2.0 W. The predicted average channel powers match very well with the supervised ones, only differing by 0.1–0.2 W, while the allocated channel powers of the other schemes differ significantly more, about 0.1–0.5 W. Two hidden layers, 256 neurons, and two-parameter distributions are the optimal choices for the policy DNN.

Chapter References

[1] Sharma, S.K.; Chatzinotas, S.; Arapoglou, P.D. Satellite Communications in the 5G Era; Institution of Engineering and Technology: London, UK, 2018; pp. 1-500.

[2] Jahid, A.; Alsharif, M.H.; Hall, T. J. A contemporary survey on Free Space Optical Communication: Potentials, technical challenges, recent advances and research direction. Journal of Net. and Comput. Applic. 2022, 200, 103311.

[3] Kaushal, H.; Kaddoum, G. Optical Communication in Space: Challenges and Mitigation Techniques. IEEE Commun. Surv. Tutor. 2016, 19, 57–96.

[4] Hemmati, H. Near-Earth Laser Communications; CRC Press: Boca Raton, FL, USA, 2009; pp. 1-418.

[5] Andrews, L.C.; Phillips, R.L. Laser Beam Propagation through Random Media; SPIE Optical Engineering Press: Bellingham, WA, USA, 2005; pp. 1–820.

[6] Majumdar, A.K. Laser Communication with Constellation Satellites, UAVs, HAPs and Balloons: Fundamentals and Systems Analysis for Global Connectivity; Springer International Publishing: Cham, Switzerland, 2022; pp. 1-270.

[7] Kodheli, O.; Lagunas, E.; Maturo, N.; Sharma, S.K.; Shankar, B.; Montoya, J.F.M.; Duncan, J.C.M.; Spano, D.; Chatzinotas, S.; Kisseleff, S.; et al. Satellite Communications in the New Space Era: A Survey and Future Challenges. IEEE Commun. Surv. Tutor. 2021, 23, 70–109.

[8] Lyras, N.K.; Kourogiorgas, C.I.; Kapsis, T.T.; Panagopoulos, A.D. On Optical Satellite Communication Systems Design: CFLOS Calculation and OGS Selection. In Proceedings of the 13th European Conference on Antennas and Propagation (EuCAP), Krakow, Poland, 2019; pp. 1-5.

[9] Lyras, N.K.; Kourogiorgas, C.I.; Panagopoulos, A.D. Cloud free line of sight prediction modeling for optical satellite communication networks. IEEE Commun. Lett. 2017, 21, 1537-1540.

[10] Kapsis, T.T.; Lyras, N.K.; Kourogiorgas, C.I.; Panagopoulos, A.D. Time Series Irradiance Synthesizer for Optical GEO Satellite Downlinks in 5G Networks. Future Internet 2019, 11, 131.

[11] Kapsis, T.T.; Panagopoulos, A.D. Optimum power allocation based on channel conditions in optical satellite downlinks. Wirel. Pers. Commun. 2021, 116, 2997–3013.

[12] Kapsis, T.T.; Panagopoulos, A.D. Robust power allocation in optical satellite MIMO links with pointing jitter. IEEE Wirel. Commun. Lett. 2022, 11, 957–961.

[13] Gao, Z.; Eisen, M.; Ribeiro, A. Resource Allocation via Model-Free Deep Learning in Free Space Optical Communications. IEEE Trans. on Commun. 2022, 70, 920-934.

[14] Eisen, M.; Zhang, C.; Chamon, L.F.; Lee, D.D.; Ribeiro, A. Learning optimal resource allocations in wireless systems. IEEE Trans. Signal Process. 2019, 67, 2775–2790.

[15] Li, Y.; Geng, T.; Tian, R.; Gao, S. Power allocation in a spatial multiplexing free-space optical system with reinforcement learning. Optics Commun. 2021, 488, 126856.

[16] Lionis, A.; Peppas, K.; Nistazakis, H.E.; Tsigopoulos, A.D.; Cohn, K. Experimental Performance Analysis of an Optical Communication Channel over Maritime Environment. Electronics 2020, 9, 1109.

[17] Lionis, A.; Sklavounos, A.; Stassinakis, A.; Cohn, K.; Tsigopoulos, A.; Peppas, K.; Aidinis, K.; Nistazakis, H. Experimental Machine Learning Approach for Optical Turbulence and FSO Outage Performance Modeling. Electronics 2023, 12, 506.

[18] Sharma, S.; Yoon, W. Energy Efficient Power Allocation in Massive MIMO Based on Parameterized Deep DQN. Electronics 2023, 12, 4517.

[19] Ortiz-Gomez, F.G.; Lei, L.; Lagunas, E.; Martinez, R.; Tarchi, D.; Querol, J.; Salas-Natera, M.A.; Chatzinotas, S. Machine Learning for Radio Resource Management in Multibeam GEO Satellite Systems. Electronics 2022, 11, 992.
[20] Nasir, Y.S.; Guo, D. Multi-agent deep reinforcement learning for dynamic power allocation in wireless networks. IEEE J. Sel. Areas Commun. 2019, 37, 2239–2250.
[21] Cho, Y.; Yang, W.; Oh, D.; Jo, H.S. Multi-Agent Deep Reinforcement Learning for Interference-Aware Channel Allocation in Non-Terrestrial Networks. IEEE Commun. Lett. 2023, 27, 936-940.
[22] Hu, X.; Liu, S.; Chen, R.; Wang, W.; Wang, C. A deep reinforcement learning-based framework for dynamic resource allocation in multibeam satellite systems. IEEE Commun. Lett. 2018, 22, 1612–1615.
[23] O'Shea, T.; Hoydis, J. An introduction to deep learning for the physical layer. IEEE Trans. Cogn. Commun. Netw. 2017, 3, 563–575.
[24] Arulkumaran, K.; Deisenroth, M.P.; Brundage, M.; Bharath, A.A. Deep reinforcement learning: A brief survey. IEEE Signal Process. Mag. 2017, 34, 26–38.
[25] Alom, M.Z.; Taha, T.M.; Yakopcic, C.; Westberg, S.; Sidike, P.; Nasrin, M.S.; Hasan, M.; Van Essen, B.C.; Awwal, A.A.S.; Asari, V.K. A State-of-the-Art Survey on Deep Learning Theory and Architectures. Electronics 2019, 8, 292.
[26] Williams, R.J. Simple statistical gradient-following algorithms for connectionist reinforcement learning. Mach. Learn. 1992, 8, 229-256.
[27] Reyes, M.; Comeron, A.; Alonso, A.; Rodriguez, A.; Rubio, J.A.; Dios, V.F.; Chueca, S.; Sodnik, Z. Ground-to-satellite bidirec-tional laser links for validation of atmospheric turbulence model. Proc. SPIE Free Space Laser Commun. Act. Laser Illum. III 2003, 5160, 44–55.
[28] Alonso, A.; Reyes, M.; Sodnik, Z. Performance of satellite-to-ground communications link between ARTEMIS and the optical ground station. Proc. SPIE Optics in Atmos. Propag. and Adap. Sys. VII 2004, 5572, 372-383.
[29] Kolev, D.R.; Toyoshima, M. Satellite-to-ground optical communications using small optical transponder (SO-TA)—received-power fluctuations. Opt. Express 2017, 25, 28319–28329.
[30] Bertsekas, D.P. Convex Optimization Theory; Athena Scientific Belmont: Belmont, MA, USA, 2009.
[31] Hastings, W.K.; Mardia, K.V. Monte Carlo Sampling Methods Using Markov Chains and Their Applications. Biometrika 1970, 57, 97–109.

Chapter 8
Thesis Summary and Future Work

In this Chapter the major contributions of this Doctoral Thesis are listed along with some suggestions for further research. It is important to remember that while the mathematical ideas described here can be used in other wireless networks, this research only represents a small portion of the larger scientific picture of optimal power allocation in optical satellite networks.

8.1 General Conclusions

Chapter 3 is focused on the modelling of received long-term irradiance time series for an optical GEO downlink and extended validation in terms of first order statistics (Probability Density Function (PDF), Cumulative Distribution Function (CDF)) and second order statistics (Power Spectral Density (PSD)). The major contributions are summarized as follows:

- A synthesizer for the generation of received irradiance time series taking into account the weak turbulence effects for an optical GEO downlink is proposed.
- The time series generator benefits from stochastic differential equations for modelling the temporal behaviour of the scintillation effects.
- The synthesizer is validated in terms of first and second order statistics (PDF, CDF, PSD) with actual experimental data from the ARTEMIS campaign with very good agreement.
- System-level simulation numerical results for various weather conditions are presented.
- Rytov theory, Kolmogorov spectrum of refractive index, links with elevation angle greater than 20°, perfect link pointing conditions, and one collimated Gaussian beam are assumed.

Chapter 4 is devoted to the optimum power allocation scheme based on channel conditions in optical GEO satellite downlinks and the optimized power allocation strategies in hybrid optical satellite networks. The major contributions are listed as follows:

- A waterfilling-based power allocation methodology and an iterative allocation algorithm are presented for an optical satellite downlink with multiple independent transmitters and receivers.
- The satellite downlink's ergodic capacity under the total expected power constraint and the peak transmitting power limitation is optimized using convex optimization techniques.
- Experimental downlink data are employed to apply the proposed allocation strategies.

- The algorithm is presented under both weak and strong turbulence conditions therefore the extreme cases of clear air turbulence.
- Network simulations with numerical data investigating the sensitivity of the algorithm to scintillation and to atmospheric attenuation are presented. The proposed methodology is compared to two other algorithms achieving much higher data rates. It may also be applied to various statistical contributions simulating different channel conditions.
- The proposed algorithm is very flexible, converges rapidly and scales well.
- Hybrid optical satellite links are investigated in a multi-input multi-output, decode-and-forward dual hop network.
- A power allocation methodology is proposed for the optimization of the system's capacity under peak and total available power constraints. The convex optimization problem is solved via the convexity theory and singular value decomposition method by considering the spatial channel correlation, the atmospheric attenuation and the turbulence strength.
- Numerical simulations are executed to examine the impact of correlation, to evaluate the proposed algorithm's performance and to investigate the case of poor source-relay conditions regarding the system's power efficiency.
- Numerical results and remarks are presented validating the proposed methodology in various network topologies and settings.

Chapter 5 is concentrated on the power allocation for reliable and energy-efficient optical LEO-to-Ground downlinks with hybrid automatic repeat request (HARQ). The major contributions are listed as follows:

- Three power allocation methodologies based on the Type I, chase combining and incremental redundancy HARQ schemes are proposed. Their performances are compared and ranked in terms of the average power consumption.
- The energy efficiency and reliability of the optical links are optimized by formulating the constrained nonlinear programming problem with the average power usage as objective function, and the maximum transmitted power, target outage probability as constraints.
- Only the channel statistics (long-term) are required to obtain the optimal power allocation strategy and not the instantaneous channel states.
- The proposed solutions are derived numerically via the interior point and sequential quadratic programming algorithm, and validated through a brute force search.

- Simulations are executed for various channel conditions and system settings by simulating a LEO passing over various turbulence intensities and ground weather conditions. Novel numerical results are reported and commented on.

Chapter 6 is focused on the robust power allocation in optical satellite MIMO links with pointing jitter. The major contributions are listed as follows:

- A robust convex optimization problem is formulated and solved for parallel GEO-to ground optical links under the effects of atmospheric turbulence and pointing jitter.
- The impact of jitter is examined on the worst-capacity yielding a maximin optimization problem and on the ergodic capacity obtaining an optimum lower bound.
- The robust optimization problem has never been studied for optical MIMO satellite links. The incorporation of atmospheric scintillation and pointing jitter impairments yields a considerably different problem than the RF one.
- The simulations use real experimental channel data from the ARTEMIS optical program.
- The proposed power allocation schemes converge to the optimal solution rapidly. To the authors' best knowledge this is the first time that this problem is investigated.

Chapter 7 is devoted on the optimal power allocation in optical GEO satellite downlinks using model-free deep learning algorithms. The major contributions are listed as follows:

- We propose a deep reinforcement learning (DRL) algorithm to optimally allocate power in an optical GEO-to-ground multi-aperture system. The proposed method accurately adjusts the expected power for each optical channel, without any knowledge of path losses and scintillation conditions. Only CSI samples are utilized.
- Experimental irradiance time series from the ARTEMIS optical satellite sessions are employed.
- The achieved ergodic system capacity from the application of the proposed algorithm greatly exceeds the performance of various model-free schemes, and approaches the model-based solution with very good agreement.
- An investigation of the impact of the number of hidden layers and neurons, policy distribution, and overfitting effects is carried out.
- The proposed solution applies to a multi-agent optical satellite environment based on the parameter sharing approach allowing centralized learning under a single policy for faster convergence.

8.2 Future Work

Several directions for future research can be suggested based on the considered assumptions and simplifications during the development of the mathematical models, the modelling and optimization algorithms during this Dissertation. These directions are listed below:

8.2.1 Moderate/strong scintillation modelling in non-geostationary orbit satellites

For the synthesis of time series modelling the effects of weak atmospheric turbulence on the downlink, a corresponding generating methodology based on stochastic differential equations could be developed for moderate and strong scintillation conditions. Similarly, non-geostationary satellites (low and medium Earth orbit satellites) are of great interest, but so are the cases of drone-to-ground, UAV-to-ground, and CubeSat-to-ground links. The primary challenges are the shorter rotation period and line-of-sight time (< 24 h), the frequent day-night cycle (in darkness > 2% of time), the rapidly varying elevation angle, the need for better optical pointing and tracking, the high travelling speed (> 10,000 mph), and the worse beam wander and aperture averaging effects. Simulated or even real-world optical satellite data can be employed.

8.2.2 Non-convex and NP-hard power allocation problems

Finding heuristics and meta-heuristics for non-convex and NP-hard optimization problems, as well as the study of optimal power allocation in optical satellite systems of massive MIMO, Non-Orthogonal Multiple Access (NOMA), constellation of satellites, etc.., are other possible applications of this research. For example, maximizing energy efficiency is a critical issue in NOMA systems and is formulated as an NP-hard optimization problem under maximum transmission power, minimum user data rate requirement, and sequential interference cancellation (SIC) requirement. Also, the non-convex power allocation problem in integrated 6G satellite-terrestrial (integrated 6G satellite-terrestrial) due to the inherent non-convexity of the objective function. The solution must demonstrate high scalability and efficiency and low complexity. The formulation of the power allocation problem itself and the proposed techniques to solve it will be the main focus of future work. The terminology used in this PhD thesis is broad and assumes that past actions or situations do not predict future situations. However, there are interesting circumstances in which this is not the case, e.g., an optical channel model that incorporates a Markov model where the channel state at one instant depends on previous instants. Similarly, proportional fairness problems take into

account an additional condition related to the previously allocated powers of terminal emitters.

8.2.3 Performance analysis of other optical uplink propagation issues with small satellites or unmanned aerial vehicles.

Beam wander is a major challenge in uplink, as it results in beam displacement of several hundreds of meters. During beam spreading the incoming beam will be diffracted and scattered independently, leading to distortion of the received wavefront. For the uplink, beam dispersion, beam wandering and variations in the angle of arrival are the main factors contributing to signal degradation and thus create a more complex power assignment optimization problem. Also, LEO nanosatellites with tiny ~9 cm telescopes can orbit the Earth quickly in about 90 minutes while CubeSat platforms have lifetimes from a few weeks to 1-2 years. Drones suffer from platform vibrations due to the drone's rotor blades and from randomly hovering due to local wind gusts and GNSS accuracy. It is therefore necessary to study optimal or robust power distribution schemes and to perform a performance analysis of these systems with simulated or experimental data. Finally, adaptive optics (AO), which are used to mitigate the effect of atmospheric turbulence and provide an undistorted beam, are of particular interest. Likewise, in the context of future research is the performance analysis of AOs in various turbulence conditions with experimental measurements if possible.

8.2.4 Machine learning and neural networks

Conventional and classic optimization methods still demonstrate advantages in the power allocation optimization of wireless network types. Nevertheless, they demand complex and intensive iterations and might be sub-optimal. On the other hand, machine learning (ML) has a lot of promise for solving difficult-to-model issues and transferring laborious and computationally expensive optimization processes to offline training. For this reason, and with the exponential increase in the number of available datasets, ML has become a fundamental technology in various areas of wireless communications, and optimal power allocations specifically. In addition to deep neural networks (DNNs), solutions with architectures of recurrent neural networks (RNNs), graph neural networks (GNNs), convolutional neural networks (CNNs) and deep reinforcement learning (DRL) techniques could be explored in distributed multi-agent environments.

8.2.5 Obtaining training data and real-system employment

Since machine learning techniques require the collection of copious amounts of high-quality data in addition to network profiles, they encounter many obstacles throughout the training phase. For example, well-characterized data is required for supervised learning systems, but this can be difficult to achieve in a rapidly changing environment. Some methods are based on simulated datasets generated using a particular kind of network. As a result, there could be a discrepancy between the optimal approach that works in a real system and the established method. The need and cost of optical satellite and terrestrial measurements will become increasingly difficult as wireless optical networks become denser and more demanding in the future.

8.2.6 Broader power allocation applications

One of the main uses for 6G has been identified as Virtual Reality (VR) and Augmented Reality (AR). Applications for VR/AR span from remote control and tactile internet to social interactions, personal entertainment, and streaming videos in cars. Requiring a latency of less than 20 ms and requiring 350 Mbits/s of bandwidth means that optimizing communication, processing, and storage resources is difficult. Besides the optical satellite networks, the algorithms presented in this Dissertation can be extended to transportation networks, vehicle-to-vehicle (V2V) communications, smart grids, and developing smart city environments. These are just a few examples of the settings where power allocation optimization and data interchange are achieved by measuring customer satisfaction. Energy-efficient and customer-oriented solutions are hence prioritized for future work. Moreover, safe reinforcement learning in wireless industrial systems and the previously discussed low-latency wireless control systems are two specific issues of relevance for Industry 4.0.

8.2.7 Secure communications

Devices are networked for real-time sensing and interaction in the Internet of Things era. Access to private data, including bank account information and health care records, should be prevented from network security risks such as eavesdropping and interception. Next-generation wireless networks will have to deal with issues such as cyberwarfare, cloud data theft, and phishing, which will have a significant impact on how data exchange is protected in a way that preserves both privacy and fairness. The free-space optical link has inherent security features and can support quantum cryptography when fiber optic infrastructure is not available. Quantum Key Distribution (QKD) is a promising technology that achieves unconditional security, which is essential for a wide range of sensitive applications. Unlike

optical fiber, FSO communication is effectively used as a quantum channel without affecting the polarization of the transmitted photons. Unfortunately, all traditional key distribution approaches are inherently unpredictable, relying entirely on computational mechanisms that are vulnerable to future developments in computer hardware and algorithms. With the exponential growth of quantum computers, it is expected that the existing public key infrastructure will become more vulnerable within a few years due to the availability of large-scale quantum computers. A GEO quantum satellite can provide a slow but continuous rate of secret key generation due to its fixed position in the sky at a very high altitude. In contrast, LEO quantum satellites are much closer to the Earth's surface and, because of this, can provide a faster but intermittent secret key generation service. In the case of a quantum satellite, the resource allocation problem thus boils down to optimizing the objective function, such as maximizing key flows and minimizing secret key consumption.

List of Publications

International Peer-Reviewed Journals

1. **T. T. Kapsis** and A. D. Panagopoulos, "Robust Power Allocation in Optical Satellite MIMO Links With Pointing Jitter," *IEEE Wireless Communications Letters*, vol. 11, no. 5, pp. 957-961, May 2022. https://doi.org/10.1109/LWC.2022.3151730.
2. **T. T. Kapsis** and A. D. Panagopoulos, "Power Allocation for Reliable and Energy-Efficient Optical LEO-to-Ground Downlinks with Hybrid ARQ Schemes," *Photonics*, vol. 9, no. 2, p. 92, Feb. 2022. https://doi.org/10.3390/photonics902009.
3. **T. T. Kapsis**, N. K. Lyras and A. D. Panagopoulos, "Long Term Irradiance Statistics for Optical GEO Downlinks: Validation with ARTEMIS Experimental Measurements," *Progress In Electromagnetics Research Letters*, vol. 82, pp. 89-94, Mar. 2019. https://doi.org/10.2528/PIERL18122105.
4. **T. T. Kapsis** and A. D. Panagopoulos, "Optimum Power Allocation Based on Channel Conditions in Optical Satellite Downlinks," *Wireless Pers. Commun.*, vol. 116, pp. 2997–3013, 2021. https://doi.org/10.1007/s11277-020-07831-z.
5. **T. T. Kapsis**, N. K. Lyras, C. I. Kourogiorgas and A. D. Panagopoulos, "Time Series Irradiance Synthesizer for Optical GEO Satellite Downlinks in 5G Networks," *Future Internet*, vol. 11, no. 6, p. 131, June 2019. https://doi.org/10.3390/fi11060131.
6. N. K. Lyras, **T. T. Kapsis**, and A. D. Panagopoulos, "Monthly Cloud Free LOS Time Series Generator for Optical Satellite Links," *Progress In Electromagnetics Research Letters*, vol. 85, pp. 25-30, 2019. https://doi.org/10.2528/PIERL18122103.
7. T. Mpimis, **T. T. Kapsis**, A. D. Panagopoulos and V. Gikas, "Cooperative D-GNSS aided with multi attribute decision making module: a rigorous comparative analysis," *Future Internet*, vol. 14, no. 7, p. 195, June 2022. https://doi.org/10.3390/fi14070195.
8. T. Mpimis, **T. T. Kapsis**, V. Gikas and A. D. Panagopoulos, "Dynamic Optimal Vehicle Selection for Cooperative Positioning Using Low-Cost GNSS Receivers," *IEEE Access*, vol. 11, pp. 134146-134154, Nov. 2023. https://doi.org/10.1109/ACCESS.2023.3337037
9. **T. T. Kapsis**, N. K. Lyras and A. D. Panagopoulos, "Optimal Power Allocations in Optical GEO Satellite Downlinks using Model-Free Deep Learning Algorithms," *Electronics*, vol. 13, no. 3, p. 647, 2024. https://doi.org/10.3390/electronics13030647.

International Peer-Reviewed Conferences

1. **T. T. Kapsis** and A. D. Panagopoulos, "Optimized power allocation strategies in hybrid optical satellite networks," *International Conference on Space Optics (ICSO) 2020*, vol. 11852, pp. 2353-2362, June 2021. https://doi.org/10.1117/12.2600009.
2. **T. T. Kapsis** and A. D. Panagopoulos, "Optimized Power Allocation Scheme in Optical Satellite Communication Downlinks," *12th International Symposium on Communication Systems, Networks and Digital Signal Processing (CSNDSP) 2020*, Porto, Portugal, pp. 1-6, July 2020. https://doi.org/10.1109/CSNDSP49049.2020.9249541.
3. N. K. Lyras, C. I. Kourogiorgas, **T. T. Kapsis** and A. D. Panagopoulos, "Ground-to-Satellite Optical Link Turbulence Effects: Propagation Modelling & Transmit Diversity Performance," *13th European Conference on Antennas and Propagation (EuCAP) 2019*, Krakow, Poland, pp. 1-5, Apr. 2019.
4. N. K. Lyras, C. I. Kourogiorgas, **T. T. Kapsis** and A. D. Panagopoulos, "On Optical Satellite Communication Systems Design: CFLOS Calculation and OGS Selection," *13th European Conference on Antennas and Propagation (EuCAP) 2019*, Krakow, Poland, pp. 1-5, Apr. 2019.
5. **T. T. Kapsis**, T. Mpimis, A. D. Panagopoulos, and V. Gikas, "Positioning Enhancement using Low Cost GNSS Receivers Data Exchange in Critical Intelligent Transport Systems," *Panhellenic Conference on Electronics & Telecommunications (PACET) 2022*, Tripolis, Greece, pp. 1-4, Dec. 2022.
6. **T. T. Kapsis**, N. K. Lyras and A. D. Panagopoulos, "Deep Reinforcement Learning Module for Power Allocation in Optical Satellite Networks," *Panhellenic Conference on Electronics & Telecommunications (PACET) 2024*, Thessaloniki, Greece, pp. 1-4, Mar. 2024.